Quantum Control of Nuclear Spins Coupled to Nitrogen-Vacancy Centers in Diamond

Sorawis Sangtawesin

A Dissertation
Presented to the Faculty
of Princeton University
in Candidacy for the Degree
of Doctor of Philosophy

Recommended for Acceptance
by the Department of
Physics
Adviser: Jason R. Petta

May 2016

Abstract

This dissertation presents experiments on nitrogen-vacancy (NV) defect centers in diamond. The NV center is an optically active color center formed by one substitutional nitrogen atom and an adjacent vacancy in the diamond lattice. Its ground state spin triplet transitions are accessible in the microwave regime and their corresponding excited state transitions exhibit spin-dependent fluorescence that allows for optical spin state readout. We present methods for the deterministic placement and the fine tuning of the NV center population in bulk diamond via ion implantation. We demonstrate quantum control of the nuclear spin in diamond through manipulation of the NV center electronic spin. By utilizing the hyperfine coupling between the electronic and nuclear spins, fast phase gates on the intrinsic nitrogen nuclear spin can be achieved within half a microsecond, a speed that far exceeds that of the gates performed with conventional nuclear magnetic resonance pulses. The hyperfine coupling also results in an enhancement of the effective nuclear gyromagnetic ratio. We demonstrate the tunability of this enhancement by changing the magnetic field. Finally, we discuss preliminary experiments aimed towards coupling a single NV center to higher nuclear spin systems.

Acknowledgements

I was originally accepted to the graduate program at Princeton University as a high-energy theoretical physicist. Upon the transition from college to graduate school, I considered changing my area of study into condensed matter experiments, where I get to do hands-on experimental physics. Thanks to Prof. Jason Petta for the opportunity to join his lab. I found myself, along with my advisor, working together on the first weekend, hammer-drilling holes into the wall of Jadwin Hall to set up a new lab space for my experiments.

Throughout my Ph.D. career, Jason has taught me to be independent as an experimentalist, and to pay attention to all the minute details of the experiments. I would not have reached this point without support from him. I would like to acknowledge Ted Brundage and Zach Atkins, two undergraduate students that I have had opportunities to work with, for their contributions to the development of the NV project that ultimately resulted in this dissertation. I acknowledge Bryan Myers, Claire McLellan, Prof. Ania Jayich, and Prof. David Awschalom for their help providing the isotopically purified diamond samples that a thesis chapter is based on. I also appreciated the fruitful discussions with Prof. Gurudev Dutt and Prof. Gregory Fuchs on the experimental techniques.

The beginning of my graduate school at Princeton has been very smooth thanks to the past Petta lab members. Mike Schroer, despite having minimal overlap with me, has provided the wonderful template used for this dissertation on the lab server. Yuliya Dovzhenko, Anasua Chatterjee and Christopher Quintana helped maintain the feelings of my college life during the transition. Karl Petersson and Loren Alegria have taught me experimental techniques that I have adapted to my experiments. Ke Wang has always brought laughter to the lab with his jokes, not all of which were sense-making. Without them, I would not be where I am today.

I also would like to thank all the current Petta lab members for their company throughout the more intense stage of my Ph.D. Yinyu Liu has always been the most productive example in the lab, publishing paper after paper. Dave Zajac and Tom Hazard have provided very useful advice to me in nanofabrication. Xiao Mi and Sonia Zhang have never ceased to be topics of entertainment in lab. Most importantly, I would like to thank my friend, colleague, and roommate George Stehlik for his tremendous knowledge and support throughout my Ph.D. And let us not forget Syntia, the loyal coffee machine that has served in Petta lab since 2011, providing our daily supply of caffeine.

Princeton University has also provided me with a strong set of personnel that help support my experiments. I would not have been able to efficiently obtain lab snacks from Thorlabs without the help from Catherine Brosowsky as a group secretary, Claude Champagne, Lauren Callahan and Barbara Grunwerg from the purchasing department and Darryl Johnson from the shipping department. Machined parts for my experiments were generally completed with ease thanks to the help from Bill Dix, Ted Lewis, and Steve Lowe. Fabrications in the cleanroom were successful with the help and advice from Yong Sun and Bert Harrop.

Lastly, life in graduate school can be difficult and I am fortunate to have good emotional support in my life. My family has always been a warm base to which I can always rely on for life advice. I am also grateful to have joined the Princeton Tango Club since the first year in graduate school, where I have also found an extended family that have been strong supporters in my life at Princeton as well. Without them, I would not be able to make it this far.

The research presented in this dissertation was supported by the Sloan and Packard Foundations, Army Research Office grant W911NF-08-1-0189 and the National Science Foundation through grants DMR-1409556 and DMR-1420541.

To my family and friends.

The work described in this dissertation has been published in the following articles and presented at the following conferences:

Appl. Phys. Lett. **105**, 063107 (2014).
Phys. Rev. Lett. **113**, 020506 (2014).

American Physical Society Meeting, March 2015, San Antonio, Texas.
American Physical Society Meeting, March 2013, Baltimore, Maryland.

Contents

List of Figures

Chapter 1

Introduction

1.1 Nitrogen-Vacancy Centers in Diamond

Diamond, a precious gemstone, possesses several desirable physical properties. Being a wide band gap material with a high Debye temperature, diamond is a perfect host for a large collection of color centers with excitation energies in the optical spectrum. The nitrogen-vacancy (NV) center is a defect in diamond formed by a single substitutional nitrogen atom and an adjacent vacancy in the diamond lattice [see Fig. 1.1]. In particular, its negatively-charged state NV^- contains a radiative transition in the visible spectrum that allows the defect to be detected via fluorescence microscopy. In this dissertation, we focus solely on the negatively-charged state NV^- and will generally refer to it as a NV.

NV centers, owing to their optical and spin properties, have been the focus of ongoing research on a wide variety of applications, such as bio-sensing, optomechanics, photonics, quantum information processing, and nanoscale magnetometry. In this dissertation, we will focus on two particular applications: (1) Using a NV center as a qubit for quantum information processing, and (2) Using a NV center as a sensitive nanoscale magnetometer.

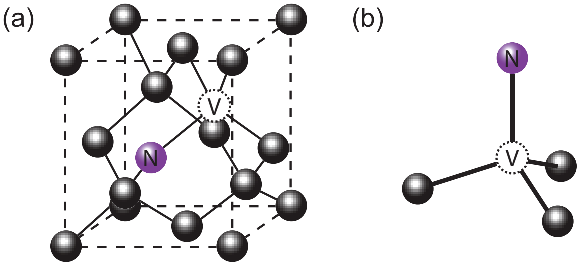

Figure 1.1: Structure of a NV center: (a) The diamond lattice consists of two interpenetrating face-centered cubic Bravais lattices. The lattice constant is 3.57 Å. A NV center is formed by replacing two adjacent carbon atoms in the diamond lattice with a nitrogen (N) and a vacancy (V). (b) The NV axis serves as a C_{3v} symmetry axis, where the structure is invariant under $2\pi/3$ rotations around the NV axis and under reflections through the planes formed by the NV axis and one of the three nearest neighbor carbon atoms.

1.2 The NV Center as a Qubit for Quantum Information Processing

The NV center has long been a good candidate for a qubit due to its optical addressability and spin-dependent fluorescence [1,2]. Its ground state spin has an electronic spin $S = 1$ spin triplet structure with a large zero-field splitting that allows for individual transitions to be isolated and addressed via ac magnetic field in the microwave regime. Millisecond long electronic spin coherence times have been observed, even at room temperature [3,4]. (Details of the electronic structure will be discussed in Section 2.1.)

The optical addressability of the NV center plays a significant role in terms of the scalability of the system. At cryogenic temperatures, the polarization of an emitted photon is dependent on the spin state of a NV center for one set of optical transitions at low strain [5]. This entanglement of the spin and photon allows for coupling of the distant NV center spins via photon entanglement [6]. The hallmark of this long range entanglement is the demonstration of a loophole-free Bell inequality violation using two NV centers physically separated over a kilometer and their photons entangled via fiber optics [7].

In addition to the cryogenic-temperature spin-photon entanglement, the NV center can also serve as a scalable quantum information processing (QIP) unit at room temperature. Its electronic spin is readily coupled to nearby nuclear spins via magnetic dipole-dipole coupling, including its intrinsic nitrogen nuclear spin. This dipole coupling also enables coupling between two NV centers at room temperature [8].

The long coherence time of nuclear spins, combined with the fast control of the NV electronic spin, results in a scalable architecture for controlling multiple nuclear spin qubits. With continuous improvements in optical detection, single shot readout of multiple nuclear spin qubits has been made possible [9, 10]. In addition, basic quantum error correction using three nuclear spin qubits has been demonstrated [11].

1.3 Extending the Coherence Time of a NV Center

One of the major requirements of a good qubit for quantum information processing is the ability to perform several computational steps on the qubit within the decoherence time. The performance in this metric can be improved by increasing the control speed and by improving the coherence time of the qubit. Demonstration of fast control pulses beyond the rotating wave approximation has been demonstrated on NV centers by engineering an impedance-matching coplanar waveguide for delivering high-power and high-fidelity control pulses to the NV center [12].

The coherence of NV centers, despite being relatively long at room temperature, still suffers deterioration from the magnetic field and electric field noise in the environment, and the strain in the diamond lattice. In high-purity diamonds used in this dissertation, the dominant contribution to the decoherence is the magnetic field noise caused by fluctuations of the electronic and nuclear spin bath surrounding the defect center. To overcome this through a materials perspective, engineering of isotopically-enriched diamond has been demonstrated, allowing a one millisecond coherence time of the NV electronic spin to be achieved at room temperature [4].

In addition to material engineering, active cancellation of the magnetic field noise can be achieved with quantum control. The simplest case of such a cancellation is the Hahn echo technique, where a refocusing π-pulse is used to reverse the state of the qubit, thereby effectively reversing the direction of the quasi-static magnetic field noise experienced by the qubit [13]. Extensions of this technique have been demonstrated using multiple refocusing pulses, aiming to decouple different types of noise fluctuations and to compensate for possible pulse errors [14, 15]. A common application is the Carr-Purcell-Meiboom-Gill (CPMG) type dynamical decoupling sequence, where the refocusing π-pulses are evenly spaced [16, 17]. Implementations of such pulse sequences have been shown to improve the coherence time of NV centers by over two orders of magnitude [18, 19]. These improvements are beneficial not only for quantum information processing, but also for the application of the NV center as a nanoscale magnetometer.

1.4 The NV Center as a Sensitive Magnetometer

Owing to the relatively large electron gyromagnetic ratio and the long coherence time of the electronic spin in NV centers, the system can be used as a sensitive magnetometer to probe the magnetic field environment surrounding the NV [20]. Since the NV center is an atomic-scale defect, it can be brought to within a few nanometers of the diamond surface, offering excellent spatial resolution. Moreover, diamond is a robust material such that it can be fabricated into nanoscale probes for scanning over a sample as well.

Magnetic field sensing using NV centers is typically based on Ramsey interference, where the spin precesses around the Bloch sphere with the rate determined by the local magnetic field [21]. Phase accumulation from such precession can then be converted to a measurable population via spin-dependent fluorescence. For ac magnetic field sensing, a Hahn-echo type pulse sequence can be employed to cancel the quasi-static magnetic field fluctuations. This ac sensing scheme can be extended via dynamical decoupling to allow for longer coherence times and more efficient filtering of the magnetic field noise spectrum [22]. Significant progress has also been made to improve the quality of shallow NV sensors via surface treatment and high-temperature annealing [23, 24]. At the current state of the art, the sensitivity allows for the detection of single electronic spins on the surface of a diamond [25].

Chapter 2

Detection and Manipulation of Single NV Centers

2.1 Electronic Structure of the NV Center

In this dissertation, we focus on the negatively-charged state of the nitrogen-vacancy center, NV$^-$. This negatively-charged state consists of six electrons in total, three from each of the neighboring carbon atoms, two from the intrinsic nitrogen atom, and one from the environment. The configuration results in an electronic structure with six optical transitions, all of which are addressable at cryogenic temperature [26, 27]. However, at room temperature, the electronic structure can be simplified to spin-triplet ground states and excited states. This simplified room-temperature energy level structure is depicted in Fig. 2.1.

The ground state of interest for quantum control is the stable spin-triplet with a zero-field splitting of $D = 2.87$ GHz between the $m_S = \pm 1$ and $m_S = 0$ spin projections. Its excited state counterpart is also a spin-triplet with a zero field splitting of $E = 1.42$ GHz [26, 28, 29]. The excited state and ground state triplets are coupled via spin-conserving optical transitions with a zero-phonon line around 637 nm.

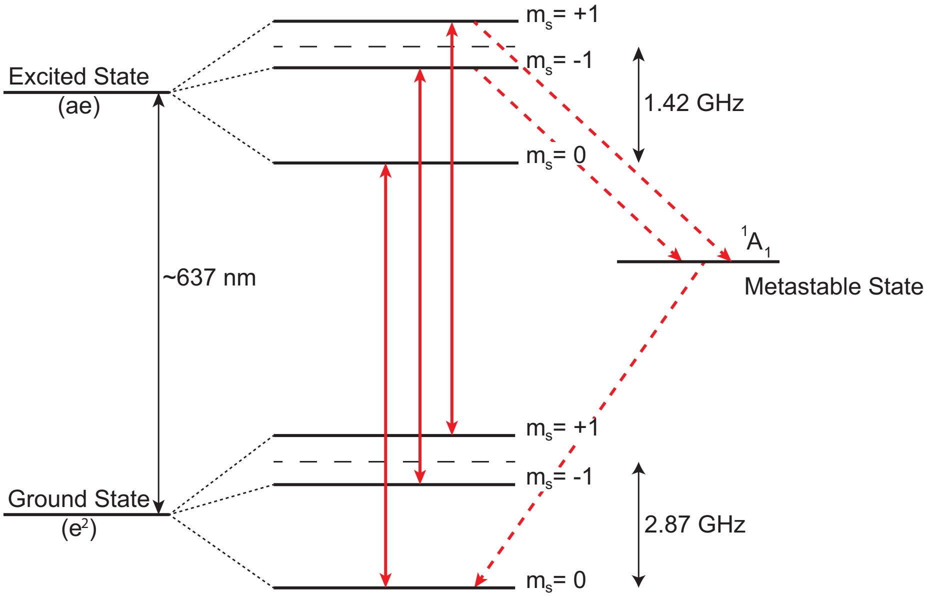

Figure 2.1: Electronic structure of a NV center at room temperature. The ground state manifold (e^2) and the excited state manifold (ae) are separated by $\Delta E \sim 1.95$ eV, corresponding to a zero-phonon line of ~ 637 nm. Each of the three electronic spin projections $m_S = -1, 0, +1$ in the ground state manifold are coupled to the same spin projections in the excited state manifold during optical excitation. However, spin-orbit interactions couple the $m_S = -1, +1$ excited states to the metastable singlet state $^1A_1$, which is then coupled to the $m_S = 0$ ground state via a non-radiative transition. We utilize the ground state spin triplets, whose Hamiltonian is given in Eq. 2.1, for quantum control.

In addition to the stable ground state and excited state spin triplets, there is also an additional metastable ground state spin singlet $^1A_1$, also commonly referred to as a shelving state, whose symmetry allows for transitions from the $m_S = \pm 1$ excited states to $m_S = 0$ ground state via this metastable state [see dashed lines in Fig. 2.1] [28]. As the metastable state has a long lifetime ~ 300 ns compared to that of the excited state ~ 12 ns and the decay from the metastable singlet state to the $m_S = 0$ ground state is non-radiative, the photoluminescence from $m_S = \pm 1$ states is suppressed. We utilize this mechanism to determine the spin state of a NV center under optical excitation. It is also precisely this transition that allows for the polarization of a NV center to its ground state $m_S = 0$ under continuous excitation with a 532-nm laser.

For the purpose of quantum information processing and magnetic field sensing, we will utilize the dynamics of the electron spin triplet ground state of the NV center, whose Hamiltonian is given by:

$$H/h = DS_z^2 + g_e\mu_B\vec{B}\cdot\vec{S} + \sum_k \left(\vec{S}\cdot A_k\cdot\vec{I}_k - g_k\mu_k\vec{B}\cdot\vec{I}_k\right). \tag{2.1}$$

Here D is the zero-field splitting, g_e is the electronic g-factor, μ_B is the Bohr magneton, $\vec{B}$ is the external magnetic field, and $\vec{S}$ ($\vec{I}$) are the electron (nuclear) spin operators. The index k sums over all nuclear spins that the NV center electronic spin interacts with via magnetic dipole-dipole coupling. The hyperfine tensor associated with each coupling is given by A_k and the gyromagnetic ratio of each nuclear spin is given by $g_k\mu_k$.

2.2 Hyperfine Coupling to the Intrinsic Nitrogen Nuclear Spin

From the general NV Hamiltonian given in Eq. 2.1, we can derive an explicit Hamiltonian to account for hyperfine coupling to the intrinsic nitrogen nuclear spin that is present in every NV center:

$$H/h = DS_z^2 + g_e\mu_B\vec{B}\cdot\vec{S} + A_\perp(S_xI_x + S_yI_y) + A_\parallel S_zI_z + QI_z^2 - g_N\mu_N\vec{B}\cdot\vec{I}. \tag{2.2}$$

The energy level diagram with the inclusion of the nitrogen nuclear spin is shown in Fig. 2.2 for both ^{14}N ($I = 1$) and ^{15}N ($I = 1/2$) nuclear spins. With an application of the external magnetic field B_z along the NV axis, the $m_S = -1$ and $m_S = +1$ energy level degeneracy is lifted by a Zeeman splitting $g_e\mu_BB_z$, where $g_e\mu_B = 2.802$ MHz/G. Hyperfine coupling to the nitrogen nuclear spin further splits each electronic state into sublevels corresponding to the different nuclear spin projections (three sublevels $m_I = -1, 0, +1$ for ^{14}N nuclear spin and two sublevels $m_I = -\frac{1}{2}, +\frac{1}{2}$ for ^{15}N nuclear spin). The $m_I = -1, +1$ states are split from the $m_I = 0$ state by an additional nuclear quadrupole coupling $Q = -4.962$ MHz in the case of ^{14}N nuclear spin ($Q = 0$ for ^{15}N nuclear spin). The degeneracy of the remaining states is lifted by nuclear Zeeman splitting, with $g_N\mu_N = 0.308$ kHz/G for ^{14}N and $g_N\mu_N = -0.432$ kHz/G for ^{15}N. Hyperfine coupling to the electronic spin, described by the hyperfine tensor A, further separates the nonzero nuclear spin states in the $m_S = \pm1$ manifold. For ^{14}N nuclear spin, the coupling strengths are given by $A_\perp = -2.70$ MHz and $A_\parallel = -2.16$ MHz. For ^{15}N nuclear spin, the coupling strengths are given by $A_\perp = 3.65$ MHz and $A_\parallel = 3.03$ MHz. Off-diagonal terms of the matrix A are zero due to the symmetry of the NV center [12, 30–32].

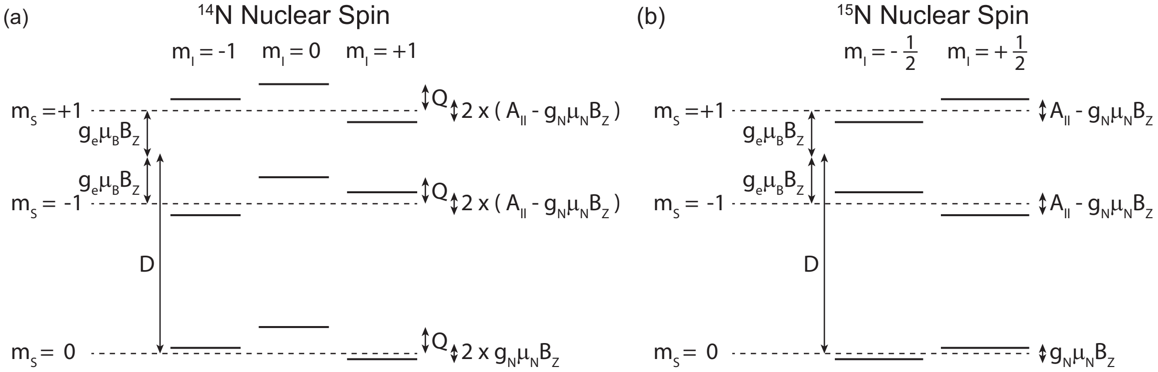

Figure 2.2: Electronic and nuclear spin level structure of a NV center in the presence of hyperfine coupling to the intrinsic (a) ^{14}N nuclear spin $I = 1$ and (b) ^{15}N nuclear spin $I = 1/2$. The $m_S = \pm1$ electronic spin states are separated from the $m_S = 0$ state by a zero-field splitting D and their degeneracy is lifted via the Zeeman energy $g_e\mu_B B_z$. Hyperfine coupling $A_\parallel$ and the nuclear Zeeman energy $g_N\mu_N B_z$ further split each electronic spin state into sublevels associated with the different nuclear spin projections m_I.

2.3 Isolating a Single NV Center

By performing scanning confocal microscopy with the setup described in Appendix A, we can obtain a fluorescence image of the sample. We then identify and characterize several samples of both type Ib and type IIa diamonds (Element Six), locating single fluorescence spots that would arise from NV centers. Type Ib diamonds typically contain up to 500 ppm of nitrogen impurities, which are dispersed throughout the crystal. These impurities can form isolated NV centers, but the majority of them remain optically inactive. However, these optically-inactive nitrogen impurities (P1 centers) contain electronic spins that contribute to the decoherence of NV centers [18]. In contrast, type IIa diamonds (referred to as high-purity diamonds) typically contain less than 5 ppb of nitrogen impurities. Therefore, NV centers formed in these type IIa diamonds exhibit longer coherence times and are more suitable for quantum control. We find that the NV density varies from sample to sample and not all the samples have a NV density low enough to allow single NV centers to be resolved using our confocal microscope.

Once a NV center is located, we verify that we indeed have a single photon emitter by adding a fiber beamsplitter and a second detector in a Hanbury Brown and Twiss setup [see Fig. 2.3(a)] and measuring the correlation function $g^{(2)}(\tau)$, defined by:

$$g^{(2)}(\tau) = \frac{\langle I(t)I(t+\tau)\rangle}{\langle I(t)\rangle^2}, \tag{2.3}$$

where $I(t)$ is the number of photons arriving at the detectors at time t and τ is the delay time between the two channels.

For a random, uncorrelated photon source, we expect $g^{(2)}(\tau) = 1$ from the normalization. In the case of an ideal single-photon source, only one detector can produce a signal at a given time and therefore $g^{(2)}(\tau)$ should vanish as $\tau \to 0$. For a n-photon source in the absence of any background, the probability that at least one photon reaches the second detector at the same time is $1 - \frac{1}{n}$. This probability represents the value of $g^{(2)}(0)$. Hence, we can write down thresholds for an n-photon source in presence of background photons that can contribute to accidental counts at $\tau = 0$, as:

$$1 - \frac{1}{n} < g^{(2)}(0) < 1 - \frac{1}{n+1}, \tag{2.4}$$

where the upper bound is given by the value of $g^{(2)}(0)$ for a $(n+1)$-photon source. Figure 2.3(b) shows an example of the antibunching effect at $\tau \approx 0$, where $g^{(2)}(\tau)$ dips to $g^{(2)}(0) \approx 0.2$, lower than the threshold for a two-photon emitter $g^{(2)}(0) = 0.5$, indicating that we have a single-photon emitter [1, 33]. The nonzero $g^{(2)}(0) \approx 0.2$ is attributed to spurious background fluorescence from the sample and the dark counts from the avalanche photodiodes themselves (100 counts/s, ∼1% of the signal). In addition to the antibunching effect, we also observe bunching effects at an intermediate τ, where $g^{(2)}(\tau) > 1$. The bunching effect is attributed to the high power of the laser excitation, where the NV center is more likely to be excited immediately after its previous photon emission [33].

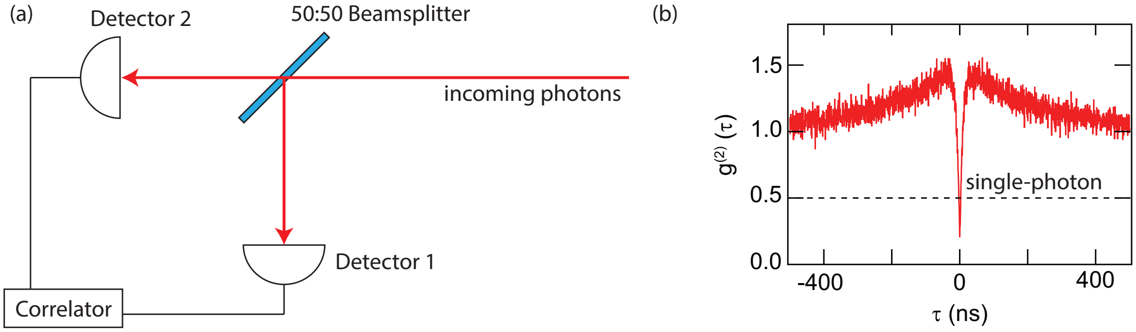

Figure 2.3: Correlation measurements: (a) Hanbury Brown and Twiss measurements: The collection fiber is split into two detectors and their signals are routed through a time-tagging photon correlator. (b) Correlation function $g^{(2)}(\tau)$ showing the normalized coincidence rate as a function of the delay time τ between two detectors. The antibunching dip $g^{(2)}(0) \approx 0.2$ indicates a single photon source, as two photons cannot reach the detectors at the same time. Bunching effects, where $g^{(2)}(\tau) > 1$, can be observed at an intermediate τ due to the high laser excitation power.

2.4 Ground State Spectroscopy

Focusing on a single NV center, we perform ground state spectroscopy via optically-detected magnetic resonance (ODMR). ODMR is performed by driving a microwave (MW) field at the sample under continuous laser excitation, varying the MW frequency ν_{MW} and subsequently monitoring the photoluminescence (PL) of the NV. When ν_{MW} is far detuned from any spin transitions, the NV center is polarized by a 532-nm excitation laser to the $m_S = 0$ state and its PL is at maximum. Near the electronic spin resonance (ESR) transition frequencies, the MW field induces the transitions between the $m_S = 0$ and $m_S = \pm 1$ states, repopulating the spin configuration of the NV. Since the $m_S = \pm 1$ spin states can decay non-radiatively into the shelving state as described in Section 2.1, the PL will decrease as the frequency approaches resonance. Zeeman splitting of the $m_S = \pm 1$ states can be induced by applying an external magnetic field B_z at the sample. Experimentally, this is achieved by placing a permanent magnet near the sample, adjusting its position to tune the magnetic field strength and orientation. Figure 2.4 shows typical ODMR spectra obtained at zero-field and with an external magnetic field applied. The separation between the two transition frequencies in Fig. 2.4(b) corresponds to the Zeeman splitting between the $m_S = -1$ and $m_S = +1$ states.

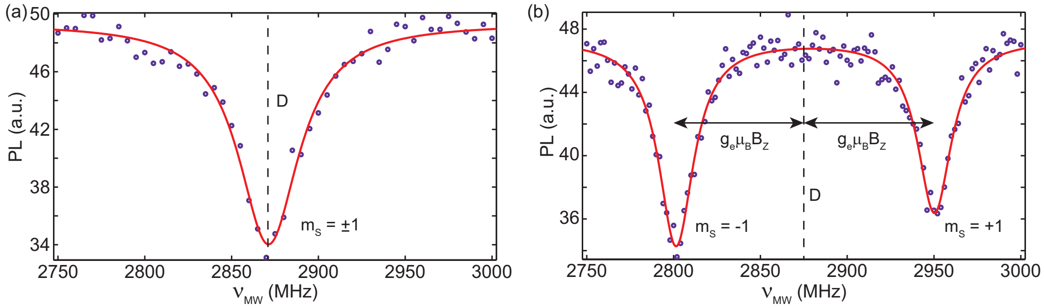

Figure 2.4: ODMR data: PL is plotted as a function of MW frequency ν_{MW}. (a) At $B_z = 0$, we observe a single dip in PL corresponding to ν_{MW} being on resonance with the $D = 2.87$ GHz zero-field splitting. (b) At $B_z = 53$ G, we observe two dips in PL corresponding to ν_{MW} being on resonance with the transitions from the $m_S = 0$ to $m_S = -1$ and $m_S = +1$ ground states. The transitions are separated by the Zeeman energy $2g_e\mu_B B_z$.

2.5 Rabi Oscillations

Rabi oscillations [34, 35] can be realized by splitting the $m_S = \pm 1$ states with an external magnetic field and choosing to address one of the ESR transitions, creating an effective two-level system as our qubit. We typically choose the $m_S = 0$ to $m_S = -1$ transition whose frequency is below 3 GHz for this purpose.

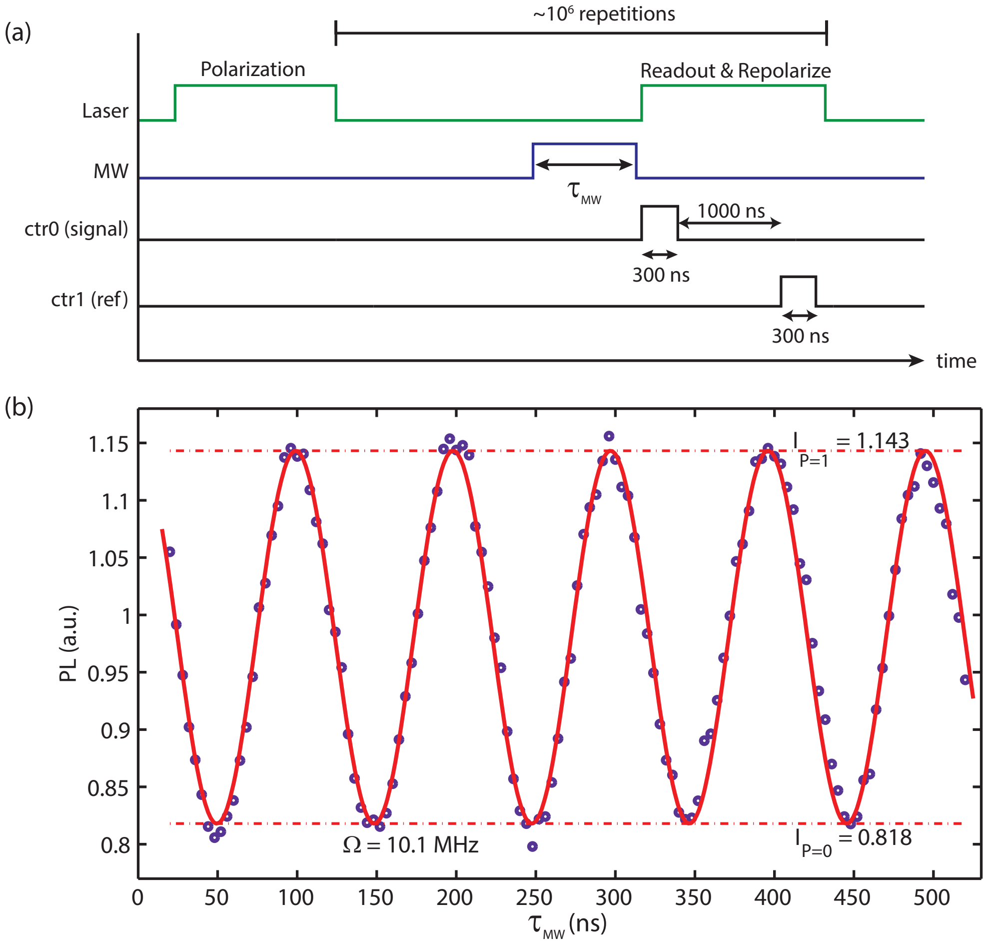

Figure 2.5: (a) Experimental pulse sequence for Rabi oscillations. The NV center is polarized to the $m_S = 0$ state with a 532-nm laser pulse. A MW pulse is then applied for a duration τ_{MW} to drive a coherent spin state rotation. Optical readout is performed by applying another laser pulse and counting the emitted signal photons. After the NV center is repolarized by the readout pulse, reference PL is recorded to account for any possible drift in the background PL. (b) PL as a function of MW pulse duration τ_{MW}. MW frequency $\nu_{\mathrm{MW}} = 2802$ MHz is tuned to resonance with the $m_S = 0$ to $m_S = -1$ transition. The data show electron Rabi oscillations with a Rabi frequency $\Omega = 10.1$ MHz.

The experimental sequence then proceeds as follows. We first initialize the NV center with a strong 532-nm laser pulse (~ 2 mW at objective), switch off the laser, apply a MW pulse with varying pulse duration τ_{MW} to drive a coherent spin state rotation, then switch on the laser and immediately count the photons from the state after the MW manipulation, integrating for 300 ns. The readout laser is left on for another 1 μs to repolarize the spin back to the $m_S = 0$ state and the photon counter is turned on for another 300 ns to measure the reference PL in order to compensate for any potential drift in the PL background signal. The process is then repeated $\sim 10^6$ times to suppress the Poisson noise to around 1% and thus improve the measurement fidelity. A typical pulse sequence is shown in Fig. 2.5(a). The data [Fig. 2.5(b)] show a sinusoidal modulation of the PL associated with the electronic spin Rabi oscillations [2,36]. We then fit the data to a cosine function and define the minimum and maximum PL as the thresholds for the $m_S = 0$ state population $P(m_S = 0) = 0$ and $P(m_S = 0) = 1$, respectively.

To validate the PL results, Rabi oscillations were performed with varying MW power P_{MW} and MW frequency ν_{MW} [see Fig. 2.6]. At low drive powers, even on resonance, there are modulations to the Rabi oscillation caused by the hyperfine coupling to the intrinsic ^{14}N nuclear spin $I = 1$. The hyperfine coupling results in three Rabi frequencies corresponding to each of the nuclear spin state projections $m_I = -1, 0, +1$. This multi-frequency modulation is also well-captured with our simulations [see Section 4.7].

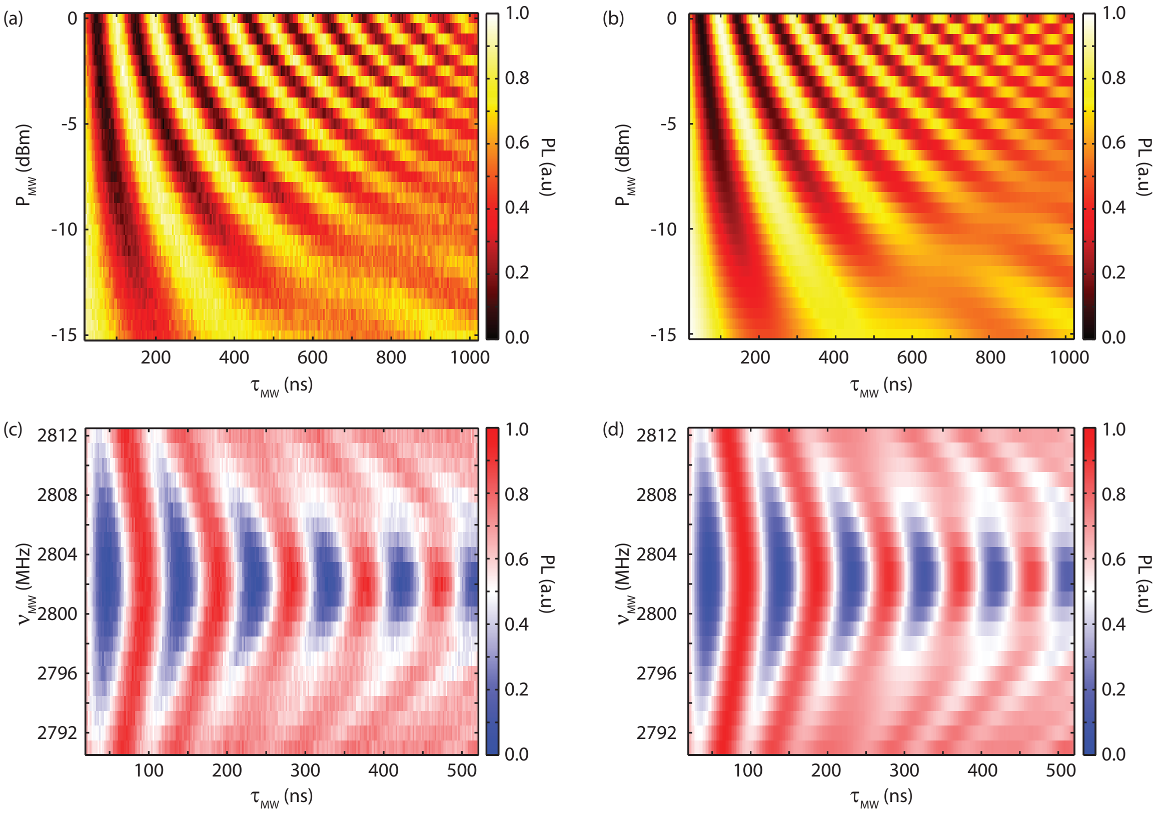

Figure 2.6: Rabi oscillations: (a) PL plotted as a function of τ_{MW} and P_{MW}, showing modulations to the amplitude at low P_{MW}. (b) Simulation of the data in (a). (c) PL plotted as a function of τ_{MW} and ν_{MW}. (d) Simulation of the data in (c).

2.6 Ramsey Experiments

To probe the coherence of the electronic spin of a NV center, we first begin with Ramsey experiments, where we prepare the spin in a superposition state and allow it to freely evolve for varying amount of time before measuring the coherence of the spin [36,37]. Experimentally, this is realized by first initializing the spin to the $m_S = 0$ ground state via optical pumping and turning off the laser excitation. We then apply a MW $\pi/2$-pulse on the $m_S = 0$ to $m_S = -1$ electronic spin transition in order to prepare a superposition state. We allow for the system to freely evolve for a duration τ and finally apply a second MW $\pi/2$-pulse to rotate the spin back to the measurement axis, converting coherence into population. The MW frequency ν_{MW} is set to be detuned from the actual electronic spin transition frequency in order to observe constructive and destructive interference patterns, i.e. Ramsey fringes. Figure 2.7 shows an example of Ramsey fringes that are modulated with three different frequencies, centered around the ~ 10 MHz detuning from the transition. These frequencies indicate different rates of state precession governed by the hyperfine interaction with the intrinsic ^{14}N nuclear spin $I = 1$. We fit the data using three superimposed cosines with a Gaussian decay envelope. The function can be written explicitly as

$$\mathrm{PL}(\tau) \propto e^{-(\tau/T_2^*)^2}\Big[\cos(2\pi\nu_1\tau+\phi_1)+\cos(2\pi\nu_2\tau+\phi_2)+\cos(2\pi\nu_3\tau+\phi_3)\Big], \quad (2.5)$$

where ν_1, ν_2, ν_3 are the precession frequencies of the three spin states and ϕ_1, ϕ_2, ϕ_3 are their corresponding phases. From the fit to the data, we extract the electron spin dephasing time $T_2^* = 2.7 \pm 0.4$ μs, a typical dephasing time for a NV in high-purity type IIa diamond with natural abundance of ^{13}C [36].

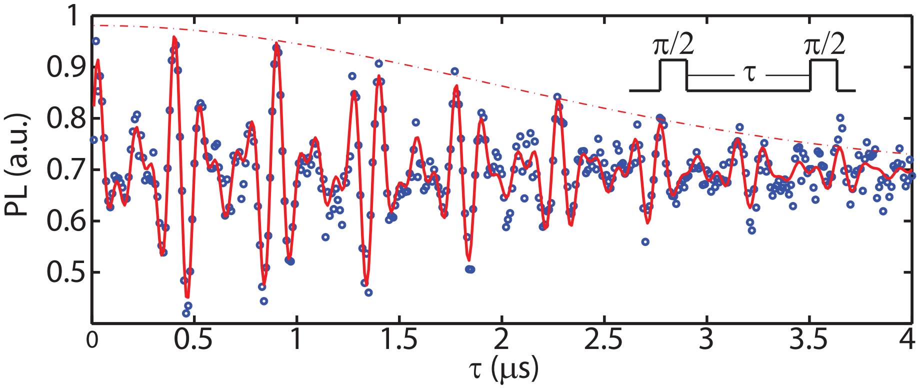

Figure 2.7: PL plotted as a function of the free precession time τ showing Ramsey fringes. The data are fitted with three superimposed cosines and a Gaussian decay envelope given by Eq. 2.5 (red). From the data, we extract the dephasing time $T_2^* = 2.7 \pm 0.4$ μs (dashed red line).

2.7 Spin Echo Experiments

The electron spin coherence of a NV center is affected by several factors, such as proximal electronic and nuclear spins, fluctuations in the external magnetic field, and fluctuations in temperature. Some of these effects, whose time scale is relatively long compared to the experimental pulse sequence, can be considered quasi-static sources of decoherence. We proceed onto mitigating these effects via spin echo techniques, where an additional π-pulse is applied in the middle of the free precession duration [13, 36]. This π-pulse effectively reverses the decoherence effect from the sources with long correlation time relative to free precession time τ, such as nuclear spins and dc magnetic field fluctuations, allowing the coherence to be preserved for a longer time.

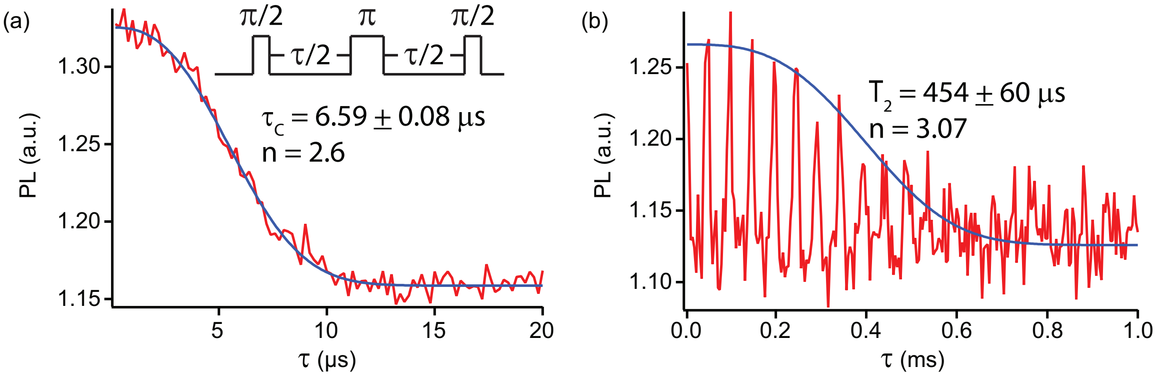

Figure 2.8: PL plotted as a function of the free precession time τ showing (a) Spin echo signal at $B_z = 37.5$ G (red) and fit to the data (blue) using a power law decay of the form $\mathrm{PL}(\tau) \propto \exp(-(\tau/\tau_c)^n)$. Best fit parameters are $\tau_c = 6.59 \pm 0.08$ μs and $n = 2.6$. (b) Spin echo signal taken under the same conditions as in (a), extended to longer times (red) and the fit to the envelope (blue) using a power law decay of the form $\mathrm{PL}(\tau) \propto \exp(-(\tau/T_2)^n)$. Best fit parameters are $T_2 = 454 \pm 60$ μs and $n = 3.07$.

Figure 2.8(a) shows the spin echo signal collapsing at a later time compared to the dephasing time obtained from Ramsey experiments. The characteristic decay envelope of this spin echo signal is an indicator of the nature of the decoherence sources. For a non-interacting spin bath, the spin echo will exhibit a Gaussian decay, whereas for a strongly-interacting spin bath, the PL signal is expected to decay as $\mathrm{PL}(\tau) \propto \exp(-(\tau/\tau_C)^4)$ [38]. In this experiment we fit the data to a power law decay envelope $\mathrm{PL}(\tau) \propto \exp(-(\tau/\tau_C)^n)$, which yields a collapse time $\tau_c = 6.59 \pm 0.08$ μs and a decay exponent $n = 2.6$. This collapse is accompanied by periodic revivals at the later times [see Fig. 2.8(b)]. These revivals occur under the conditions where $\tau/2$ is an integer multiple of the Larmor precession period of ^{13}C (25 μs at $B = 37.5$ G), synchronizing the noise from ^{13}C with the spin echo sequence. This implies that ^{13}C nuclear spins are the main decoherence source in this high-purity type IIa diamond. Fitting the revival peaks to a power law decay $\mathrm{PL}(\tau) \propto \exp(-(\tau/T_2)^n)$ yields an electron spin coherence time $T_2 = 454 \pm 60$ μs and $n = 3.07$, values that are consistent with with other literatures [36, 39].

Chapter 3

Highly Tunable Formation of NV Centers via Ion Implantation

3.1 Introduction

Advances in QIP require the use of multiple qubits that are stable and easily addressable. The NV center in diamond stands out as a candidate for this application due to its spin-dependent fluorescence and long coherence time at room temperature [4, 8, 11, 40]. However, the feasibility of integrating naturally occurring NV centers into a large-scale QIP architecture is limited by their random locations in the diamond lattice. The technique of nitrogen ion implantation can overcome this obstacle by offering precise control of NV center locations, while maintaining the quality of the NV centers created [8, 23, 41–46].

In order to achieve high accuracy placement of NV centers, techniques such as implantation through a scanning force microscope tip, focused-ion beam, and apertures in implantation masks have been developed [45–47]. In terms of ease of fabrication and scalability, one of the most versatile methods is implantation through lithographically defined apertures [42, 48].

In this chapter, we study the efficacy of this method by demonstrating highly-controllable NV implantations with different ion fluences across a wide range of aperture diameters. Within each ion fluence, aperture diameters vary from 80 to 240 nm. We characterize the implanted NV centers using PL data and autocorrelation measurements $g^{(2)}(\tau)$ [33]. Together, these data allow us to determine the statistics of NV center formation. We observe a linear relationship between the mean number of NV centers per aperture and the aperture area, from which we extract implantation yields of $6-7\%$. These yields are consistent across all ion fluences and with previously reported values [42, 48, 49]. Finally, we measure spin dephasing times $T_2^* \sim 3$ μs, a value comparable to that of naturally occurring NV centers, thus demonstrating the capability to maintain high quality NV centers and fine-tune the NV population distribution at well-defined locations [36, 50].

3.2 Implantation Process with Aperture Masks

We begin by selecting an electronic grade diamond (N $<$ 5 ppb, natural abundance ^{13}C, Element Six) with (100) orientation and low background PL. Typically, no NV centers are observable within our confocal microscope's 60×60 μm^2 field of view before implantation. As illustrated in Fig. 3.1(a), we create an implantation mask on the diamond surface by spin coating the diamond with a $t = 230$ nm thick layer of PMMA electron beam resist. Arrays of apertures are patterned on this PMMA mask in 100×100 μm^2 grids with 2 μm pitch using 125 kV electron beam lithography. Following the lithography, we implant the sample with 20 keV ^{15}N$^+$ ions at a 7° tilt to prevent ion channeling [42, 51].

We simulate the implantation process using Stopping and Range of Ions in Matter (SRIM) [48, 52]. We use a diamond substrate density of 3.52 g/cm^3 and a displacement energy of 37.5 eV [48]. Figure 3.1(b) shows the trajectories resulting from the

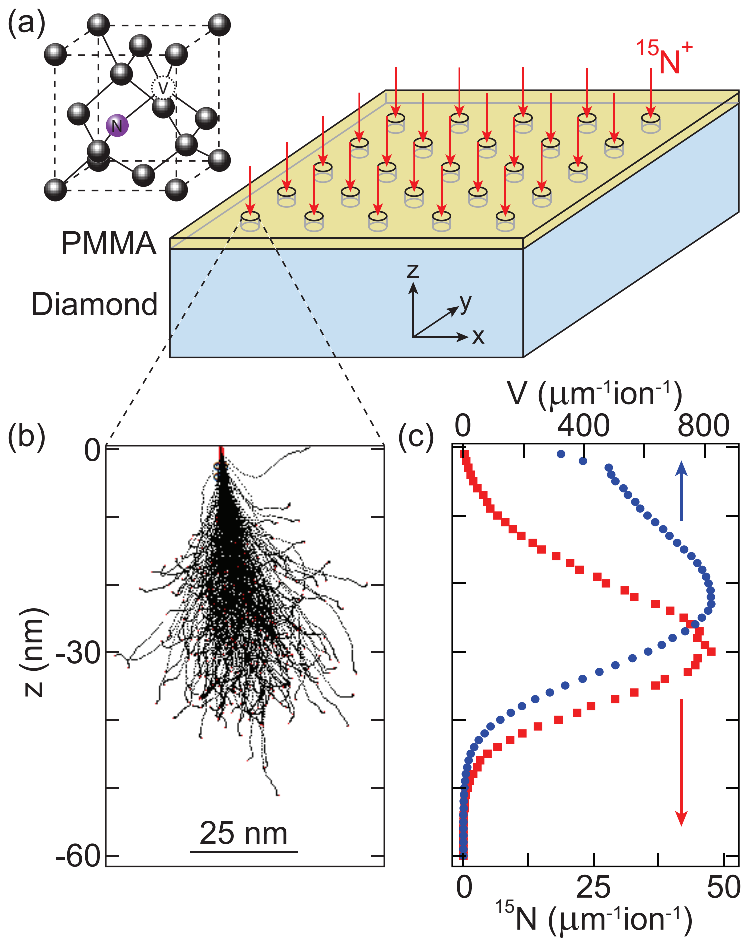

Figure 3.1: (a) Implantation method: A 230 nm thick layer of PMMA serves as an implantation mask. Arrays of apertures are patterned using electron beam lithography. (b) SRIM simulation of $^{15}N^+$ ion implantation with 20 keV energy. (c) Distribution of ^{15}N atoms and vacancies, V, per micron of depth as a function of implantation depth, z, integrated over the xy–plane.

implantation of 1,000 ions, while Fig. 3.1(c) provides the statistical distributions of the implanted ^{15}N and the vacancies that are created due to implantation. The average depth of implanted ^{15}N is $\sim$ 30 nm for our implantation energy of 20 keV. A simulation performed with a PMMA target shows that the ions are stopped with $>$ 99.99% probability within the PMMA layer.

In order to obtain reliable results, the same diamond sample is used for all implantations. Three separate implantations are performed by exposing the masked substrate to a $^{15}N^+$ ion beam with average fluences of 2×10^{11}, 1×10^{11}, and

5×10^{10} ions/cm^2 in each exposure, respectively. The average fluence in each exposure is controlled by the beam current and the exposure time. After the last implantation, the sample is cleaned in a boiling mixture of 1:1:1 nitric, perchloric, and sulfuric acid for 30 minutes. The sample is then annealed at 850 °C in vacuum for 2 hours to mobilize the vacancies, repair lattice damage, and allow the vacancies to be captured by the substitutional nitrogen atoms, forming NV centers [53–55]. A second acid cleaning step is performed for 4 hours after annealing to remove graphitic carbon and to oxygen terminate the surface [23, 51, 56].

3.3 Fine-Tuning of NV Center Populations

To control the number of ions implanted through different apertures during one ion exposure, we vary the aperture diameter by shifting the sample out of the focal plane of the electron beam during the lithography process. With the sub-micron positioning accuracy and the large depth of focus ($\sim 10\ \mu$m) of the electron beam, this technique results in reproducible and highly-tunable aperture diameters. Figure 3.2(a) shows an optical dark field image of the PMMA implantation mask with ~ 200 nm diameter apertures separated by 2 μm. We image a sample subset of apertures using a scanning electron microscope (SEM) to determine the aperture diameter, d, as shown in Fig. 3.2(b). Figure 3.2(c) shows d measured as a function of the electron beam focus offset, δz, demonstrating the ability to tune the aperture diameters from 80 to 240 nm.

The implanted sample is characterized using a scanning confocal microscope [57]. A 532 nm excitation laser is focused onto a diffraction-limited spot on the sample with a high numerical aperture objective lens and the resulting PL is measured with an avalanche photodiode operating in the single-photon counting regime. The PL of the NV centers, represented by the photon count rate, is dependent on the polarization

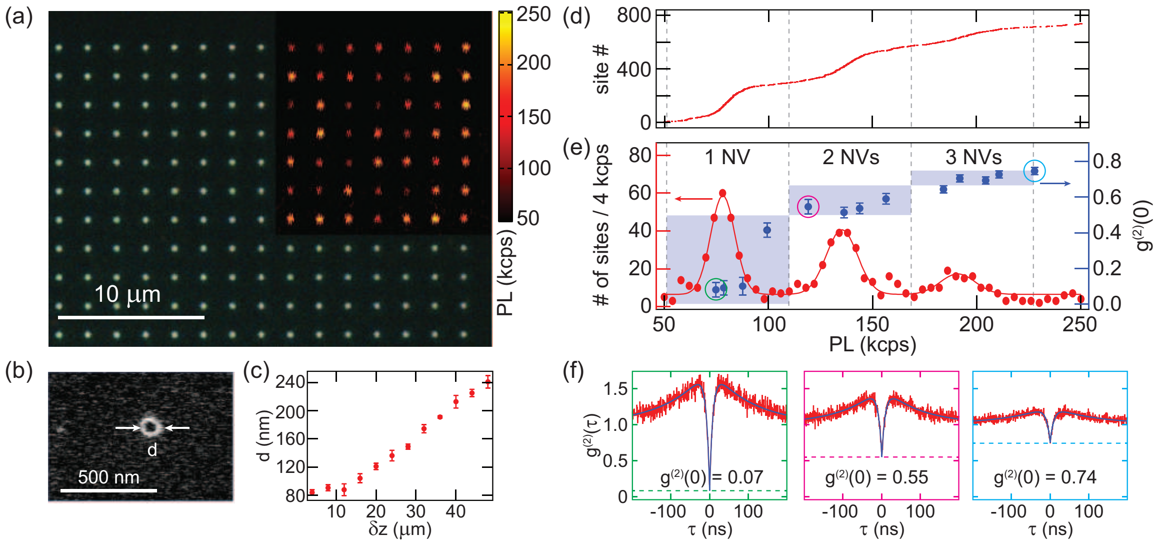

Figure 3.2: (a) Optical dark field image of the PMMA implantation mask. Overlay: A confocal microscope image shows PL from implanted NV centers (with the photon count rate in units of kilocounts per second, kcps). (b) Scanning electron micrograph of an aperture with diameter $d = 82$ nm. (c) Aperture diameter d as a function of the electron beam focus offset δz. (d) PL data from 750 implantation sites showing distinct count rates associated with different numbers of NVs. (e) Red data points and curves show histograms of PL from (d) and Gaussian fits to the data, respectively. Expected ranges of the autocorrelation minima $g^{(2)}(0)$ for one, two, and three single-photon emitters are defined by the blue shaded regions. Blue data points correspond to measured values of $g^{(2)}(0)$, indicating that we have one, two, and three NVs in those sites. (f) Autocorrelation function $g^{(2)}(\tau)$ from the one-, two-, and three-NV sites indicated by the circles in (e).

of the excitation photons. For a (100)-oriented diamond surface, there is a two-fold degeneracy of the four NV axes when projected onto the (100) face [58]. To produce consistent PL levels across all sites regardless of NV center orientation, we use a circularly polarized 532 nm laser excitation, along with a laser power high enough to saturate the cycling transitions for multiple NVs (~ 2 mW at the objective). As shown in Fig. 3.2(a), measurements of the PL show emission from the implanted array of NV centers. The PL data from several implantation sites are carefully analyzed for each ion exposure and aperture diameter to determine the implantation efficiency.

3.4 Characterization of the Implantation Sites

Figure 3.2(d) shows raw PL data from a sample of 750 sites implanted with average ion fluences of 2×10^{11} and 1×10^{10} ions/cm^2. We estimate the average background PL level to be $20 - 30$ kcps. Since NV centers are single-photon emitters, we expect the photon emission rate from each site to be proportional to the number of NVs within that site. The dense population around 80, 135, and 190 kcps, as indicated by the histogram in Fig. 3.2(e), is suggestive of distinct PL levels for one, two, and three NV centers, respectively.

To confirm that the PL levels from the histogram do indeed correspond to discrete numbers of NV centers, the photon autocorrelation function $g^{(2)}(\tau)$ is measured on a subset of implantation sites. Blue data points in Fig. 3.2(e) show that the autocorrelation minima $g^{(2)}(0)$ are in excellent agreement with their expected values, which are indicated by the shaded blue regions. The expected value of $g^{(2)}(0)$ for an n-photon source is given by Eq. 2.4. Photon bunching effects from the high excitation power are also observed for larger delay times τ, as shown in Fig. 3.2(f), where $g^{(2)}(\tau) > 1$ [see Section 2.3].

Using the now established scaling of the PL to the number of NV centers, we obtain an average number of NV centers per site, $\bar{n}_{\mathrm{NV}}$, by analyzing PL data from $100 - 400$ implantation sites for each implantation parameter (ion exposure and focus offset). Figure 3.3(a) shows the resulting $\bar{n}_{\mathrm{NV}}$, obtained from the three ion exposures, as a function of the effective aperture area, A, given by

$$A = \frac{d^2}{2}\left(\cos^{-1}(\beta \tan\theta) - \beta \tan\theta \sqrt{1 - \beta^2 \tan^2\theta}\right). \tag{3.1}$$

This takes into account shadowing from the PMMA mask due to the $\theta = 7°$ implantation angle and the aspect ratio of the aperture $\beta = t/d$. The effective aperture area is $\sim 15 - 50\%$ smaller than the physical area of the aperture for our range of aperture diameters.

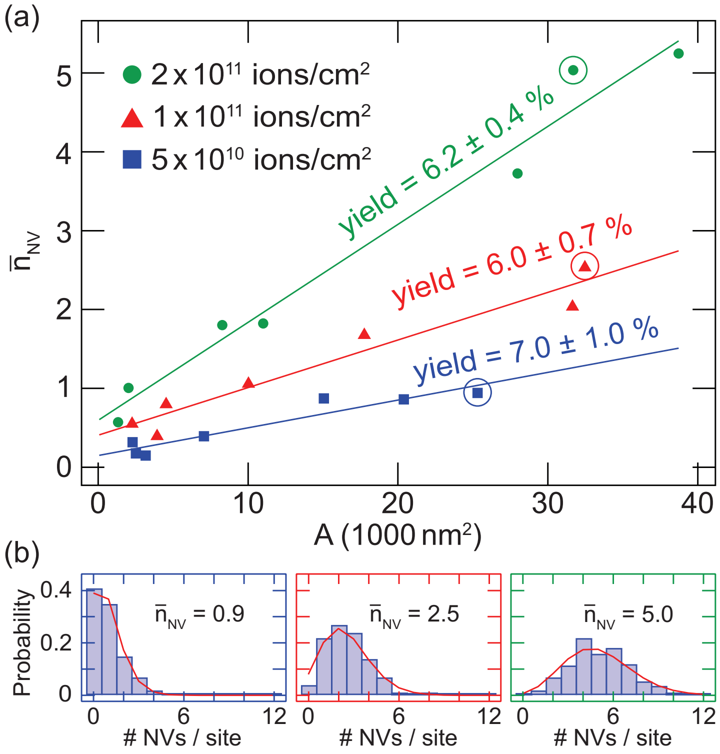

Figure 3.3: (a) Average number of NV centers, $\bar{n}_{\mathrm{NV}}$, as a function of effective implantation aperture area, A, for three exposures of $^{15}\mathrm{N}^+$, each with a different ion fluence. All three exposures result in a yield of $6 - 7\%$. (b) Population distributions of NV centers obtained from the three different ion fluences and aperture diameters that are indicated by the circles in (a). Solid lines are Poisson distributions for a given $\bar{n}_{\mathrm{NV}}$.

From linear fits to the results, we obtain ion-to-NV conversion yields of $6.2 \pm 0.4\%$, $6.0 \pm 0.7\%$ and $7.0 \pm 1.0\%$ for average ion fluences of 2×10^{11}, 1×10^{11}, and 5×10^{10} ions/cm^2, respectively. We also found similar yields on a second sample that was implanted with an average ion fluence of 2×10^{11} ions/cm^2 (data not shown). Within each array of the same ion exposure and aperture diameter, the NV population distribution follows Poisson statistics, as shown in Fig. 3.3(b). These results demonstrate that we can reliably tune the average number of NV centers in each aperture.

3.5 Coherence of the Implanted NV Centers

To probe the coherence of the implanted NV centers, we focus on implantation sites containing single centers and perform ODMR spectroscopy by driving MW signals through a 25 μm wire placed across the diamond surface. Working at a moderate magnetic field of $B_z \sim 50$ G aligned along the [111] direction, we can distinguish the NV centers with [111] orientation from those with other orientations using continuous wave ODMR. We then evaluate the quality of these NV centers by measuring the dephasing time, T_2^*, using a Ramsey experiment [36].

The Ramsey experiment is performed by first defining a two-level system using the $m_s = 0$ and $m_s = -1$ states. After preparation of the electronic spin in $m_s = 0$ by optical pumping, we apply a $\pi/2$-pulse to prepare a superposition state and then allow the state to evolve freely for a time interval τ_{free}. We then apply a second $\pi/2$-pulse to convert the coherence into population, followed by optical readout. Figure 3.4(a) shows the measured PL as a function of τ_{free}. The data display fast oscillations that decay with a characteristic timescale $T_2^* = 3.39 \pm 0.02$ μs, a value that is comparable to naturally occurring NV centers in high quality, non-isotopically purified diamond [36, 50].

The fast oscillations in Fig. 3.4(a) are the result of the MW pulse being detuned by ~ 5.5 MHz from the $m_s = 0$ and $m_s = -1$ transition. In our case, there are two hyperfine transitions associated with the $I = \frac{1}{2}$, ^{15}N nuclear spin, leading to two different detunings and hence the beating of the signal in Fig. 3.4(a). By applying a Fourier transformation to the Ramsey data, we can extract the frequency of the two transitions relative to the MW drive. Figure 3.4(b) shows that the two hyperfine transitions are separated by a splitting of $A_{\parallel} = 3.042 \pm 0.004$ MHz, consistent with previously reported values [29, 31]. We also performed pulsed ODMR measurements by optically pumping the electronic spin to $m_s = 0$ and applying a MW π-pulse with varying frequency, ν_{MW}, before optical readout [59]. When ν_{MW} is on resonance with

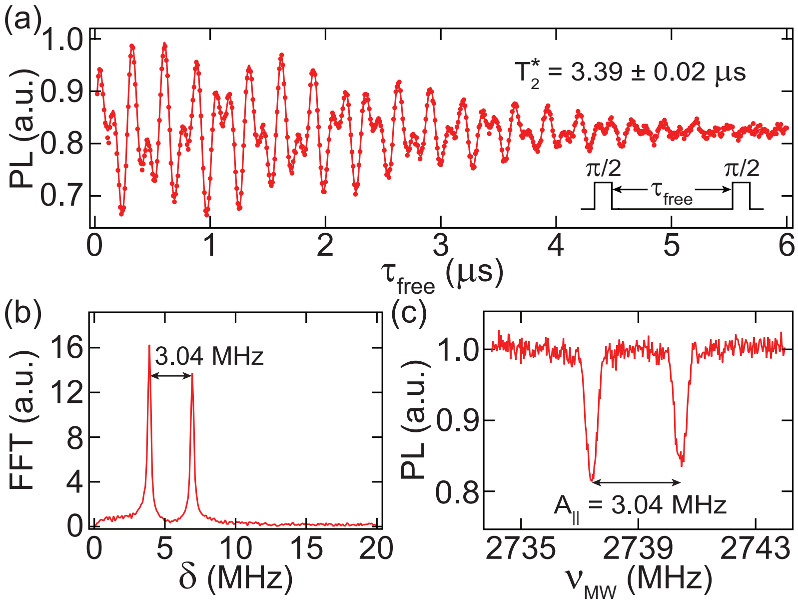

Figure 3.4: (a) Ramsey fringes: PL plotted as a function of free precession time τ_{free}. A fit to the data (solid line) yields a dephasing time $T_2^* = 3.39 \pm 0.02$ μs. (b) Fourier transform of the Ramsey data indicating two modulation frequencies separated by the hyperfine splitting $A_{\|} = 3.042 \pm 0.004$ MHz. (c) Pulsed ODMR: PL plotted as a function of MW frequency ν_{MW}, showing $A_{\|} = 3.04 \pm 0.01$ MHz.

the transition from $m_s = 0$ to $m_s = -1$, we see a reduction in PL from the NV center. With low MW powers (such that the transitions are minimally power broadened) we observe two hyperfine transitions yielding the same $A_{\|} = 3.04 \pm 0.01$ MHz.

3.6 Summary

In conclusion, we have demonstrated a simple and reproducible way of forming NV centers via ion implantation. This work has critical applications for creating coupled NV systems and integrating them into larger scale QIP architectures. Recent studies of quantum gate operations involving multiple nuclear spins coupled to a NV center required the analysis of $\sim 3,300$ randomly-distributed NV centers to find the desired spin environment [11]. The controlled formation of NV centers at well-defined locations demonstrated here will allow for the efficient automation of such a characterization, while providing a desirable distribution of NV populations. In addition, since our positioning accuracy is limited only by electron beam lithography, our process allows for the placement of NV centers in nanopillars and on-chip optical resonators [60, 61]. This work advances the field toward realizing the full potential of the NV center for scalable QIP applications.

Chapter 4

Fast Room-Temperature Phase Gate on a Single Nuclear Spin in Diamond

4.1 Introduction

The NV center in diamond is one of the most promising systems for quantum computation due to its convenient optical spin initialization and readout schemes, which can be performed at room temperature [3, 4, 62]. In addition to effective manipulation of the electronic spin, hyperfine coupling provides a means to detect and control proximal nuclear spins, enabling multiple qubit operations [10, 12, 36, 39, 63–65]. Recent experiments have demonstrated high-fidelity initialization and readout of nuclear spins in diamond using a NV center as an auxiliary qubit [9, 10]. Robust control of nuclear spins can also be achieved at room temperature with coherence times over one second [30, 50, 66].

As qubits, nuclear spins are known for their long coherence times and isolation from the external environment [67]. NV centers serve as a perfect gateway for accessing nuclear spins in diamond. However, the magnetic moment of a nuclear spin is roughly 1000 times smaller than that of the electron spin, which imposes a fundamental limit on the relevant interaction time with direct ac magnetic fields. Typically, nuclear spin rotations require at least several microseconds to complete [30, 39].

In this chapter, we demonstrate fast phase gate operations on a single $I = 1$ ^{14}N nuclear spin intrinsic to a NV center by utilizing off-resonant Rabi oscillations of the electronic spin, as previously demonstrated on N@C$_{60}$ fullerene ensembles by Morton *et al.* [68,69]. By simultaneously driving electronic transitions associated with the two spin projections of the nuclear qubit, phase accumulation between the nuclear spin states can be generated on the timescale of the electron Rabi oscillations. Through this quantum control approach, we can achieve a π-phase gate in less than 500 ns, a speed far exceeding that of the nuclear Rabi oscillations $\tau_n \sim 40$ μs. The pulses can be applied repeatedly, providing rapid phase shifts to bang-bang decouple the qubit from the environment and preserve the qubit state for as long as ~ 140 μs [68–70].

4.2 Methods

Our sample is a high purity type IIa diamond (Element Six) with naturally occurring NV centers. We determine the locations of single NV centers relative to pre-patterned alignment marks using fluorescence confocal microscopy, as shown in Fig. 4.1(a). We verify single photon emission from a single NV center by measuring the photon correlation function $g^2(\tau)$ [33]. After a single NV has been identified, we fabricate on-chip coplanar striplines and dc electrodes near the NV center. The NV used in this experiment has $g^2(0) < 0.5$ [see inset of Fig. 4.1(a)]. MW and radio frequency (RF) pulses are applied to the stripline to drive electron spin and nuclear spin transitions, respectively [see Fig. 4.1(b–c)]. The dc electrodes allow Stark shifting of the NV center energy levels [71, 72], but are not used in this experiment.

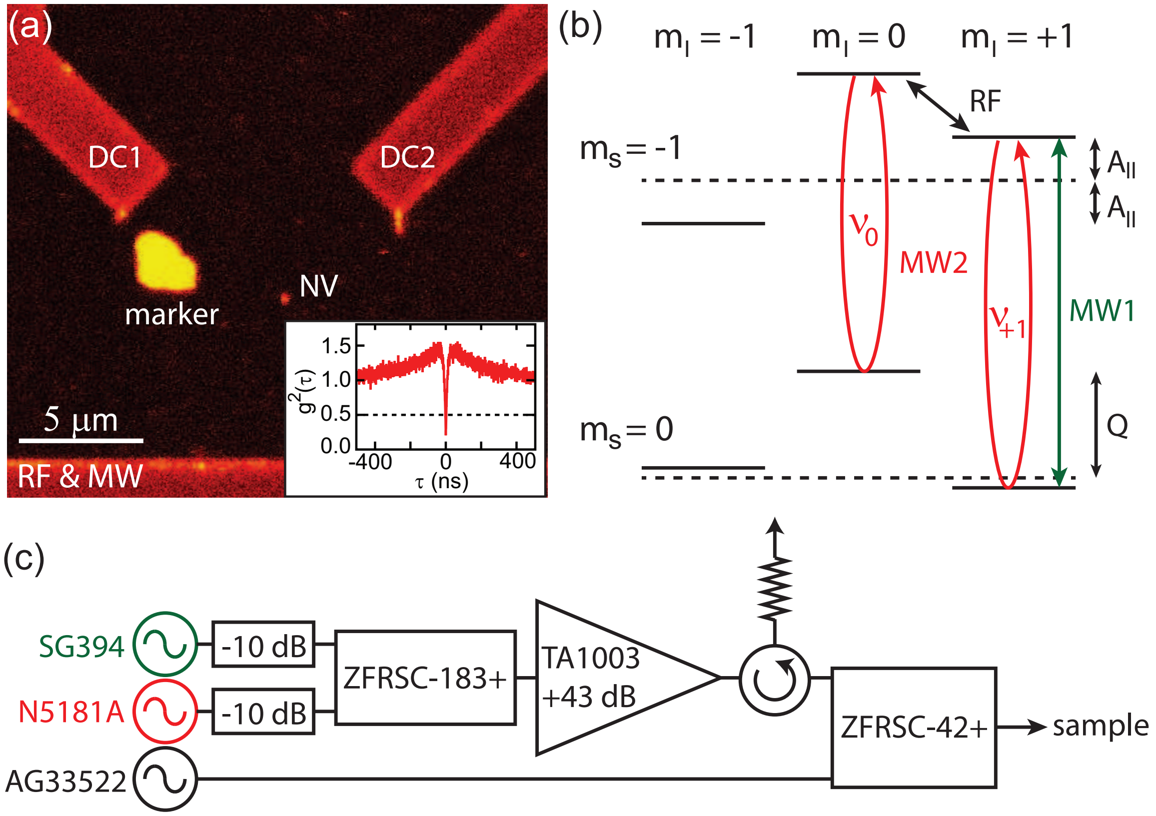

Figure 4.1: (a) Confocal image of the NV center used in the experiment. Two dc electrodes (not used) and a RF & MW stripline are fabricated near the NV center. Inset: Measurements of the second order correlation function $g^2(\tau)$, with $g^2(0) < 0.5$ indicating emission from a single NV center. (b) Energy level diagram, with energy levels indexed by the electron spin quantum number m_I and nuclear spin quantum number m_S. The $m_\mathrm{S} = +1$ level is not shown in the level diagram due to the relatively large electron Zeeman energy. Microwave excitations (MW1 and MW2) drive electronic transitions, while RF excitation is used to drive nuclear spin transitions. (c) Citcuit diagram: Two MW signal generators (SG394 and N5181A) are used to generate MW1 and MW2 pulses. The MW signals are combined via a resistive combiner and amplified to achieve strong ac magnetic fields at the sample. A circulator is placed at the output of the amplifier to prevent high-power reflections. Finally, the amplified MW signals are combined with the RF signal from AG33522 via another resistive combiner and the output is delivered to the sample.

Electron spin rotations are driven using MW signals generated from two sources (SRS SG394, Agilent N5181A), which are combined and then amplified using a +43 dB amplifier (Triad TA1003). For nuclear spin control, an additional function generator (Agilent 33522A) is used to generate a RF signal. All signals are combined and then delivered to the sample via an on-chip coplanar stripline fabricated on the diamond surface close to the NV [see Fig. 4.1(c) for the circuit diagram]. The experimental control sequence is generated using a high-speed digital delay generator (PulseBlasterESR-PRO500) with 2 ns time resolution.

The ground state manifold of the NV center is described by the Hamiltonian given in Eq. 2.2. The relevant energy level diagram is shown in Fig. 4.1(b). The $m_S = +1$ state is far detuned and therefore not shown in the diagram. We use the $m_S = 0$ and $m_S = -1$ levels to encode the electron spin qubit, allowing optical initialization and readout of the NV center electron spin state [1, 28]. We select the two sublevels $|m_S, m_I\rangle = |-1, +1\rangle$, $|-1, 0\rangle$ for our nuclear qubit as the transition is well isolated from the others, allowing selective excitation using the RF field. Moreover, it allows us to perform readout of the nuclear spin state using a microwave π-pulse (MW1, frequency ν_{MW1}), tuned to resonance with $m_I = +1$ transition ν_{+1}, mapping the nuclear spin state to the electronic spin state. The electron spin state is subsequently measured using optical readout [30, 39]. To create well-defined nuclear spin dynamics as a reference, we use RF pulses on resonance with the ^{14}N transition to induce nuclear Rabi oscillations with Rabi frequency Ω_n. We note that this is necessary as natural Larmor precession of the ^{14}N nuclear spin is prohibited due to its large quadrupole coupling [36].

In detail, when the system is in an arbitrary state $|\psi\rangle = \alpha|-1,0\rangle + \beta|-1,+1\rangle$, with $|\alpha|^2 + |\beta|^2 = 1$, we apply a MW pulse (MW2) with frequency ν_{MW2} for a short duration t, driving the electronic transitions $|-1,0\rangle \leftrightarrow |0,0\rangle$ and $|-1,+1\rangle \leftrightarrow |0,+1\rangle$ (with transition frequencies ν_0 and ν_{+1}, respectively). In the strong driving limit, where the electron Rabi frequency greatly exceeds the detunings $\Omega_e \gg \delta_{m_I} \equiv \nu_{\mathrm{MW2}} - \nu_{m_I}$, electrons undergo fast Rabi oscillations between $m_S = 0$ and $m_S = -1$ regardless of the nuclear spin state. We ensure that the electron Rabi frequency is the same on both transitions by setting ν_{MW2} midway between ν_0 and ν_{+1}. If t is chosen such that $\Omega_e t = 2n\pi$, the electron spin state will return to the original $m_S = -1$ subspace, with phase accumulation generated by the off-resonant electron spin Rabi oscillations:

$$U(t)|\psi\rangle = e^{in\pi}\left(\alpha e^{i\delta_0 t/2}|-1,0\rangle + \beta e^{i\delta_{+1}t/2}|-1,+1\rangle\right). \tag{4.1}$$

This process implements a phase gate on the nuclear spin, with the relative phase difference $\Delta\phi = (\delta_{+1} - \delta_0)t/2 = (\nu_0 - \nu_{+1})t/2 = A_{||}t/2$ between the two states set by the hyperfine coupling $A_{||}$ and the tunable duration of the MW2 pulse t). We note that this process also generates a global phase of $e^{in\pi}$ on all the states that are being driven by MW2, which can be used as a robust π-phase gate on the nuclear spins [11, 73].

The full experimental sequence, including optical initialization and readout, is illustrated in Fig. 4.2. A dc magnetic field $B_z \sim 500$ G is applied along the NV-axis, bringing the system close to the excited state level anti-crossing (ESLAC) [29]. At the ESLAC, the NV center electronic spin is first polarized to $m_S = 0$ via optical pumping with a 532 nm laser. During this process, the ^{14}N nuclear spin is dynamically polarized to $m_I = +1$ [74]. Details of the nuclear spin polarization process are described in Appendix B. The choice of working at the ESLAC provides high fidelity initialization and readout of the nuclear spin without requiring a Ramsey-type pulse sequence, where the fidelity is limited by a weak selective MW pulse and electron dephasing during the Larmor precession period in the initialization protocol [39]. After the system is polarized optically, a selective π-pulse (MW1) is applied to transfer the

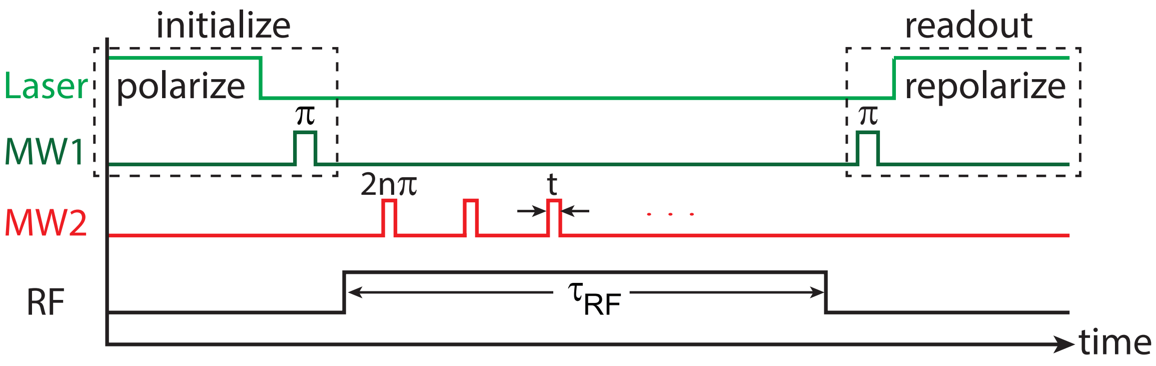

Figure 4.2: Pulse sequence used to implement the nuclear spin phase gate during nuclear Rabi oscillations. We initialize the nuclear spin qubit with the application of a laser pulse, followed by a selective MW1 π-pulse. We drive nuclear spin Rabi oscillations with a subsequent RF pulse. Phase gates are performed by driving $2n\pi$ rotations of the electronic spin with MW2 pulses. Finally, we apply a selective MW1 π-pulse to map the nuclear spin state to the electronic spin state before an optical readout.

population to $|-1,+1\rangle$, completing the initialization process. Spin manipulation is performed by applying a RF pulse with duration τ_{RF}, while phase gate "kicks" from MW2 are simultaneously applied. Finally, optical readout is performed after applying another selective MW1 π-pulse that converts the population from $|-1,+1\rangle$ to the bright state $|0,+1\rangle$. This yields a PL output that is proportional to the $|-1,+1\rangle$ population at the end of the pulse sequence.

4.3 ^{14}N Nuclear Spin Dynamics

We probe the $|-1,+1\rangle \leftrightarrow |-1,0\rangle$ nuclear spin transition by sweeping the RF frequency ν_{RF} for a fixed τ_{RF} that is set to achieve a π-pulse when on resonance. When ν_{RF} is on resonance with the nuclear spin transition, population will be transferred from $|-1,+1\rangle$ to $|-1,0\rangle$. Since $|-1,0\rangle$ is off resonance with MW1, the population transfer leads to a "dark" readout and reduces the PL intensity [see Fig. 4.3(a)]. ν_{RF} is then tuned to resonance with this transition. By varying τ_{RF}, nuclear spin oscillations can be observed with a Rabi frequency $\Omega_n \sim 25$ kHz [Fig. 4.3(b)]. This nuclear Rabi frequency is much greater than the Rabi frequency calculated using only

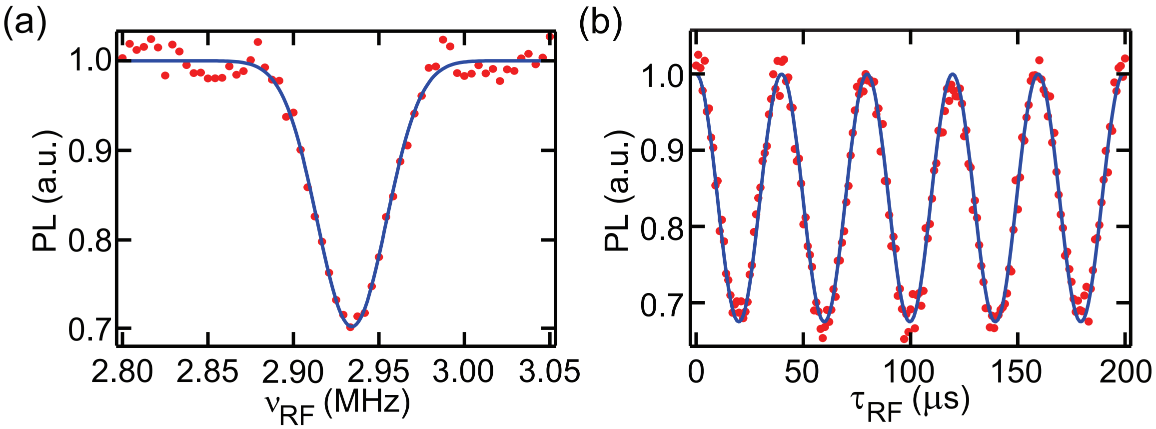

Figure 4.3: (a) PL measured as a function of RF frequency ν_{RF} showing a nuclear spin transition at $\nu_{\mathrm{RF}} = 2.934$ MHz, with a Gaussian fit to the data. (b) PL as a function of RF pulse length τ_{RF} showing nuclear spin Rabi oscillations.

the nuclear gyromagnetic ratio, due to the additional $\sim 10\times$ enhancement from the electron-nuclear flip-flop, $\Omega_n \approx g_N \mu_N B_{\mathrm{RF}} + A_\perp g_e \mu_B B_{\mathrm{RF}}/D$ [36]. This enhancement is explained in detail in Chapter 5.

To measure the electronic transition frequency, we perform electron-nuclear double resonance spectroscopy by preparing the system in $|-1,0\rangle$ or $|-1,+1\rangle$ using the calibrated MW1 and RF pulses. We start by optically initializing the spin into the $|0,+1\rangle$ state, then we either apply only a selective MW1 π-pulse or apply a selective MW1 π-pulse with a subsequent RF π-pulse to prepare the the $|-1,+1\rangle$ state or the $|-1,0\rangle$ state, respectively [see Fig. 4.4(a–b)]. After this preparation, we then apply a MW2 π-pulse with varying frequency. Then, we reverse the preparation process to perform readout of the remaining population in the original $|-1,+1\rangle$ or $|-1,0\rangle$ state.

When MW2 is off-resonant, the state is unaffected by MW2 and the readout sequence will successfully transfer the population to the bright state $|0,+1\rangle$. When MW2 is on-resonant, the population is driven out of the initially prepared state. Therefore during the readout the $m_I = +1$ state will then be flipped to the dark state $|-1,+1\rangle$ as we have effectively applied a total of 3π rotation on the electronic

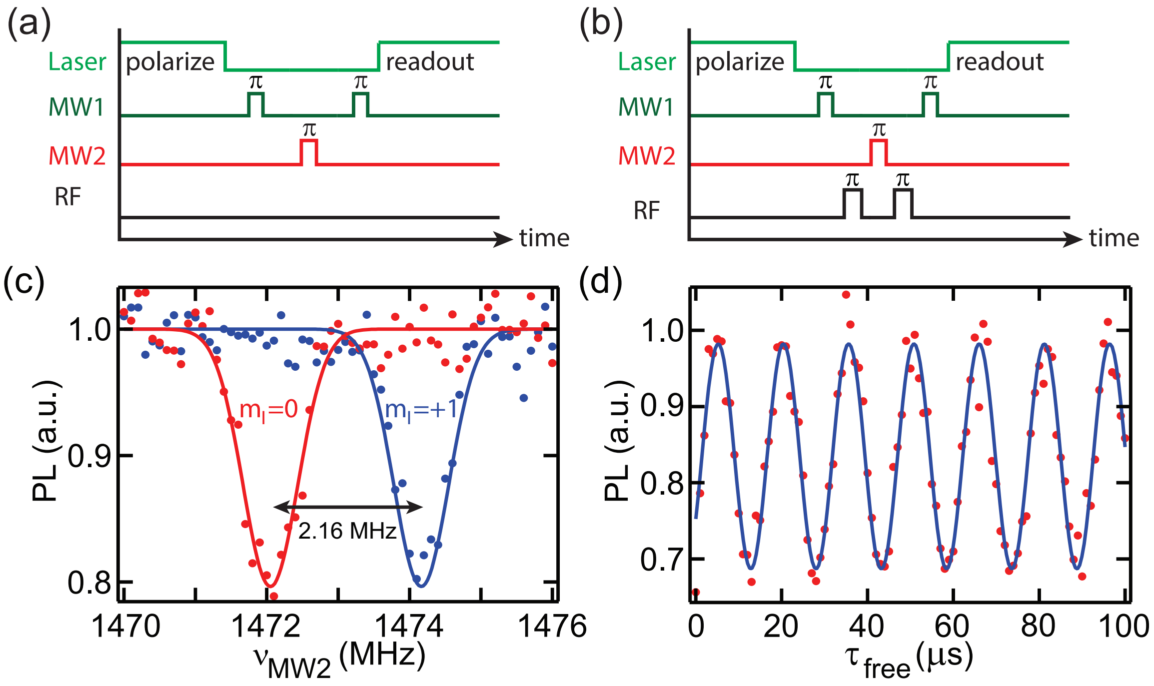

Figure 4.4: Pulse sequence of electron-nuclear double resonance for probing (a) $|-1,+1\rangle \leftrightarrow |0,+1\rangle$ and (b) $|-1,0\rangle \leftrightarrow |0,0\rangle$ transitions. (c) PL as a function of selective MW2 π-pulse frequency ν_{MW2} showing transition frequencies associated with the $m_I = +1$ and $m_I = 0$ nuclear spin projections, with Gaussian fits to the data. (d) Nuclear Ramsey measurements: PL measured as a function of free precession time τ_{free} showing no visible decay out to 100 μs.

spin. For $m_I = 0$ case, the state will remain in $|0,0\rangle$, which contributes to a dark optical readout at the ESLAC [see Appendix C], as the readout RF and MW1 pulse is now off-resonant.

A decrease in PL occurs when ν_{MW2} is on resonance with the electron spin transitions [Fig. 4.4(c)], allowing us to extract the hyperfine coupling $\sim$ 2.16 MHz, consistent with other experiments [12,30,75]. We also implement a Ramsey sequence on the ^{14}N nuclear spin [Fig. 4.4(d)]. Here the system is prepared in a superposition state $|\psi\rangle = \frac{1}{\sqrt{2}}(|-1,+1\rangle + |-1,0\rangle)$ with a nuclear spin $\frac{\pi}{2}$-pulse and allowed to freely precess for a duration τ_{free} before another $\frac{\pi}{2}$-pulse is applied to rotate the spin back to the original basis. The details of the Ramsey experiment sequence are given in Section 4.4. We do not observe any damping in the Ramsey fringes during this measurement interval, indicating a long nuclear spin phase coherence time $T^*_{2,n} > 100$ μs.

4.4 Nuclear Ramsey Experiment

To accurately measure the phase accumulation from the application of phase gates, we implement a Ramsey sequence on the ^{14}N nuclear spin. The experimental sequence is depicted in Fig. 4.5(a). A nuclear spin $\pi/2$-pulse prepares the system in the superposition state $|\psi\rangle = \frac{1}{\sqrt{2}}(|-1,+1\rangle + |-1,0\rangle)$. This state is allowed to evolve for a free precession interval τ_{free} before another $\pi/2$-pulse is applied to rotate the spin back to the measurement basis. Figure 4.5(b) shows Ramsey fringes as a function of τ_{free}. For direct comparison, we now apply a phase gate operation during the Ramsey sequence. As shown in Fig. 4.5(c), an abrupt $\Delta\phi = \pi$ phase shift is observed in the Ramsey data when a π-phase gate is applied 13 μs into the free precession interval. The solid curve is the theoretical prediction obtained by interrupting the sinusoidal Ramsey fringes with an abrupt π phase shift. We observe no damping of the Ramsey fringes during this measurement interval.

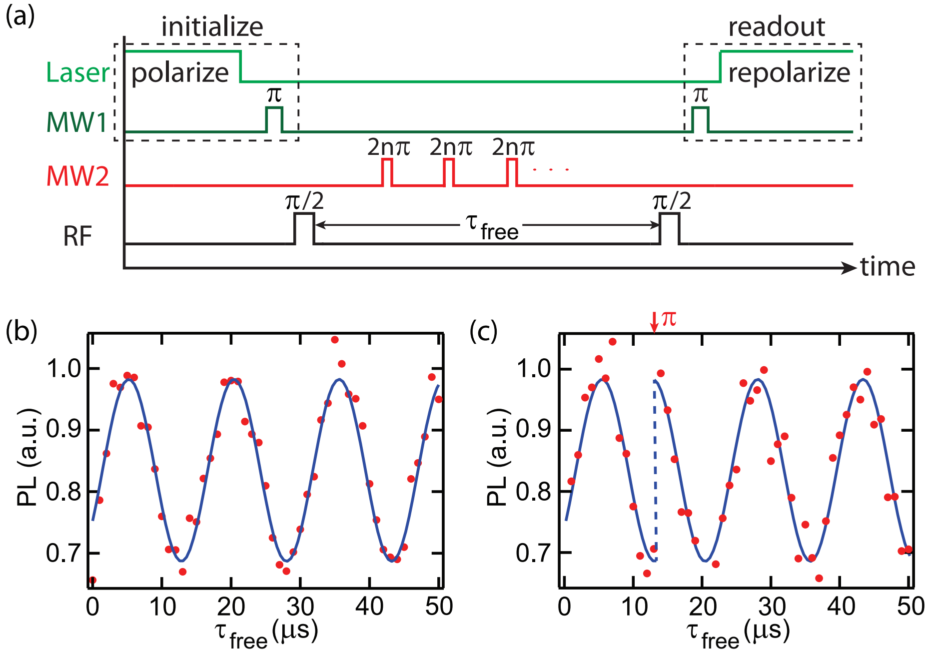

Figure 4.5: (a) Pulse sequence used to perform phase gates during a nuclear Ramsey experiment. (b) PL measured as a function of free precession time τ_{free} without a phase gate applied. (c) PL measured as a function of free precession time τ_{free} with a phase gate applied 13 μs into the free-precession interval, indicated by the red arrow.

4.5 Demonstration of Fast Phase Gates

Nuclear spin phase gates are calibrated by tuning the MW2 frequency ν_{MW2} to the midpoint between the $m_I = 0$ and $m_I = +1$ transitions. We apply one MW2 pulse of varying duration t during the Ramsey sequence [Fig. 4.6(a)] and extract the phase of the fringes afterwards. The inset of Fig. 4.6(a) shows that the nuclear spin phase accumulation $\Delta\phi$ is linearly proportional to the gate duration t. For this experiment the MW2 power is tuned such that six full cycles of electron Rabi oscillations correspond to a π-phase gate ($\Omega_e t/2\pi = 6$). We note that the π-phase gate duration $t = 2\pi/A_{||} = 462$ ns is fixed by the hyperfine coupling strength $A_{||} = 2.16$ MHz [Fig. 4.3(c)]. This corresponds to an electron Rabi frequency $\Omega_e = 12.96$ MHz.

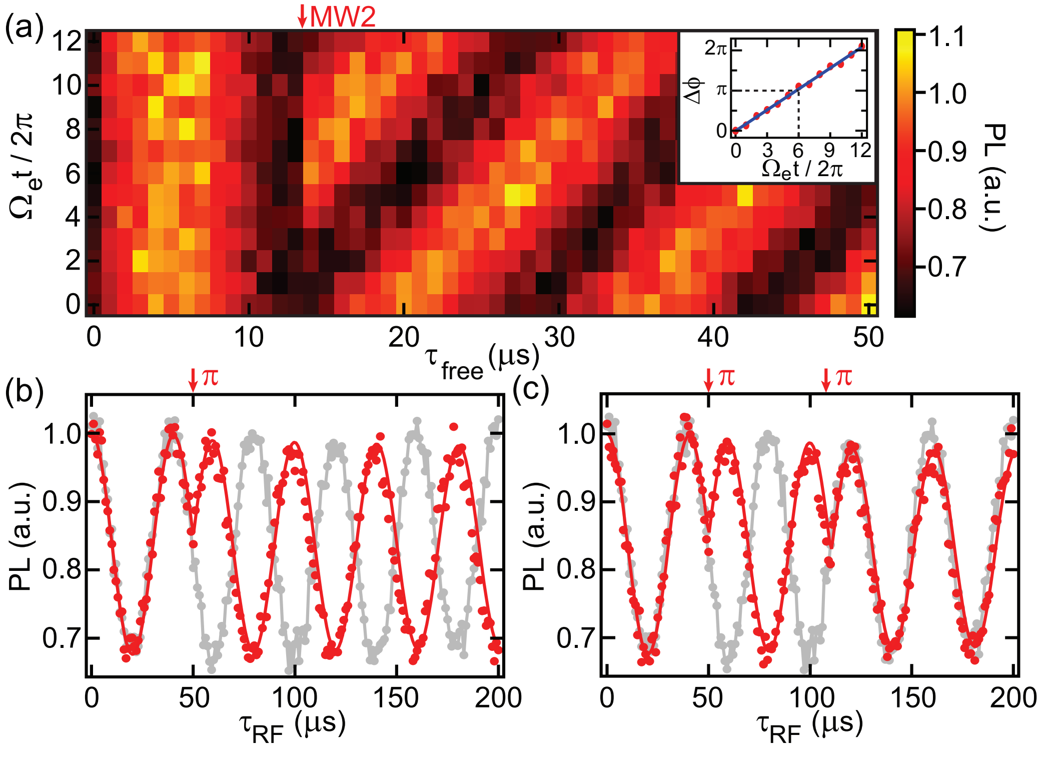

Figure 4.6: (a) Nuclear Ramsey fringes with one phase gate of varying time t applied 13 μs into the free-precession interval. Inset: Extracted phase shift of the fringes after the phase gate is applied. (b),(c) Comparison between bare nuclear Rabi oscillations (grey) and nuclear Rabi oscillations with fast π-phase gates applied (red): (b) One gate applied at 50 μs. (c) Gates applied at 50 μs and 110 μs. Red curves are simulation results.

We now show that the phase gate can be applied during nuclear Rabi oscillations. Results with one and two π-phase gates are shown in Fig. 4.6(b) and (c), respectively. The red data points show PL intensity as a function of τ_{RF} with phase gates applied and the red curves are simulation results. For direct comparison, the grey curves show nuclear Rabi oscillations that are not interrupted by phase gates. Phase gates are applied at the times indicated by the red arrows in the figures. The phase shifts $\Delta\phi = \pi$, evident in the two plots, indicate that we successfully applied π-phase gates on the nuclear spin qubit with each $t = 462$ ns gate operation time, far exceeding the speed of nuclear spin Rabi oscillations $\tau_n \sim 40$ μs shown in Fig. 4.3(b).

4.6 Bang-Bang Decoupling of the Nuclear Spin

The fast π-phase gate can be applied repeatedly to decouple the nuclear spin from the RF pulse, effectively locking the nuclear spin state. We demonstrate nuclear spin locking of the $m_I = 0$ state by applying multiple π-phase gates in rapid succession for up to several nuclear Rabi oscillation periods [Fig. 4.7(a–b)]. We also demonstrate locking of a superposition state of the nuclear spin in Fig. 4.7(c). While the state preservation is evident, there is $\gtrsim 30\%$ decrease in the amplitude of nuclear Rabi oscillations after several phase gates are applied. The amplitude decrease is asymmetric; it reduces the bright state PL level while leaving the dark state PL level unchanged. This suggests that it is not caused by dephasing of the nuclear spin, in which case the amplitude would be dampened symmetrically. To understand this effect, we first show from simulations that the decrease in contrast is due to the population being driven out of the $|m_S, m_I\rangle = |-1, 0\rangle, |-1, +1\rangle$ two-level subspace. Then, we argue that this missing population contributes to a "dark" readout, resulting in the asymmetric decrease in the oscillations.

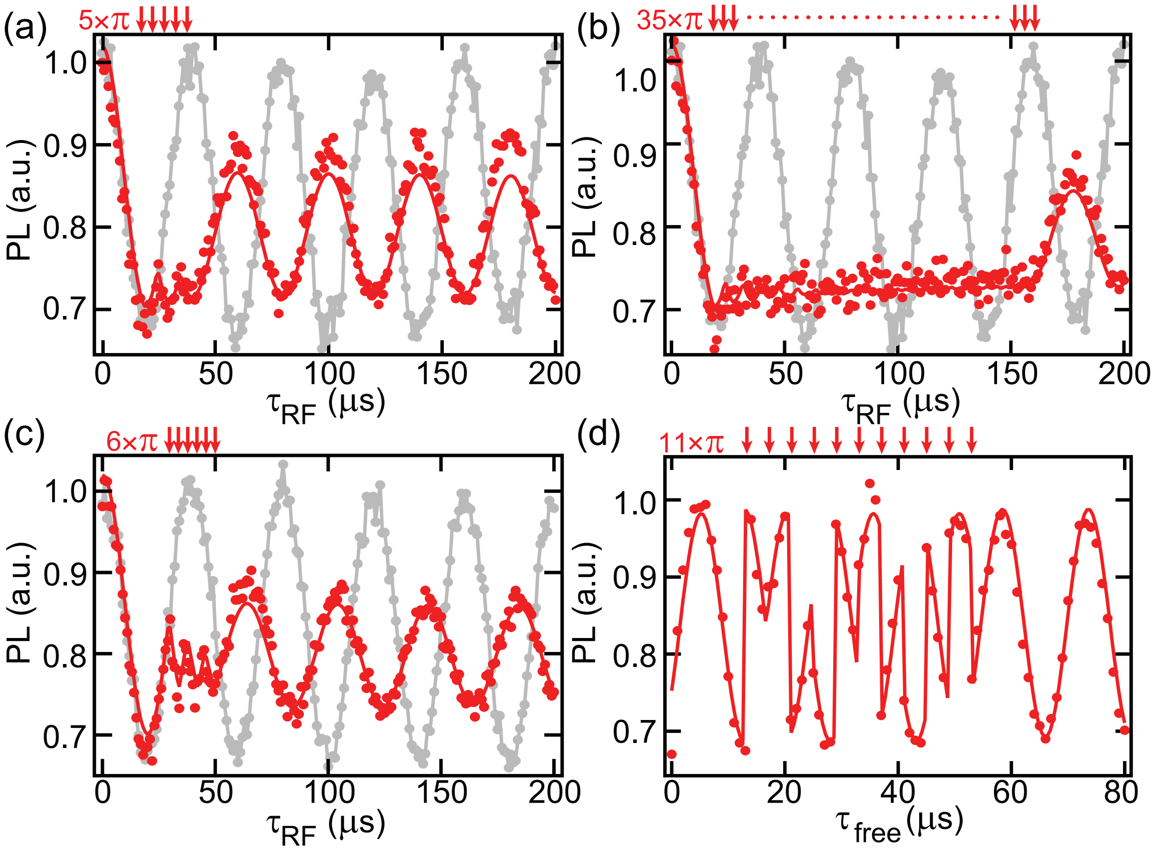

Figure 4.7: Comparison between bare nuclear Rabi oscillations (grey) and nuclear Rabi oscillations with multiple π-phase gates applied in quick succession, locking the nuclear spin (red). Red curves are simulation results. (a) 5 gates applied every 5 μs from 20 μs to 40 μs. (b) 35 gates applied every 4 μs from 20 μs to 156 μs. (c) 6 gates applied every 4 μs from 30 μs to 50 μs. (d) Nuclear Ramsey experiment with 11 π-phase gates applied at the times indicated by red arrows. In this case, there is no visible decrease in the amplitude of the Ramsey fringes. The theoretical prediction is given by the solid curve.

4.7 Simulations of the Nuclear Spin Phase Gates

To simulate the experiment we use the Hamiltonian given in Eq. 2.2 and add driving terms:

$$H_N^{\mathrm{ac}} = \Omega_n \sin(2\pi\nu_{\mathrm{RF}}t)I_x \tag{4.2}$$

$$H_e^{\mathrm{ac}} = \Omega_e \sin(2\pi\nu_{\mathrm{MW2}}t)S_x + r\Omega_n \sin(2\pi\nu_{\mathrm{RF}}t)S_z. \tag{4.3}$$

The experimentally determined Rabi frequencies $\Omega_e = 12.96$ MHz and $\Omega_n = 25$ kHz are used in the simulation, corresponding to $B_{\mathrm{MW2}} = 9.2$ G and $B_{\mathrm{RF}} = 8.4$ G, respectively. The dc magnetic field is fixed at $B_z = 500$ G. An off-axis drive field is accounted for using a phenomenological parameter r, which couples the RF drive field to the Zeeman splitting of the electron spin state. State evolution is calculated using the Lindblad master equation:

$$\dot{\rho} = -\frac{i}{\hbar}[H, \rho] + \left(L\rho L^\dagger - \frac{1}{2}(\rho L^\dagger L + L^\dagger L \rho) \right). \tag{4.4}$$

Dephasing of the electron spin is modeled using the Lindblad operator

$$L = \sqrt{1/T_2} \begin{pmatrix} 1 & 0 & 0 \\ 0 & 0 & 0 \\ 0 & 0 & -1 \end{pmatrix}, \tag{4.5}$$

with the electron spin coherence time $T_2 = 300$ μs extracted from spin echo experiments. Electron spin relaxation and nuclear spin dephasing are neglected as there is no observable decay on the timescale of our experiments. We start the simulation with the system in a pure state $|0, +1\rangle$ before the MW1 initialization pulse is applied.

Figure 4.8(a) shows the simulation result with $r = 0$, indicating a minimal decrease in the Rabi oscillation contrast after multiple phase gates are applied. In contrast, the simulation results shown in Fig. 4.8(b) indicate that there is a population buildup in the $|m_S, m_I\rangle = |0, 0\rangle$ state after the application of multiple phase gates. This population buildup results in a decrease in the maximum population of the $|-1, +1\rangle$ state Rabi oscillations after the phase gate, which agrees with the experimental result. This is due to the RF drive being applied simultaneously with the MW2 pulses, causing the electronic levels to oscillate with a frequency comparable to the electron Rabi frequency [76]. A non-ideal rotation on the $|-1, 0\rangle \leftrightarrow |0, 0\rangle$ transition during

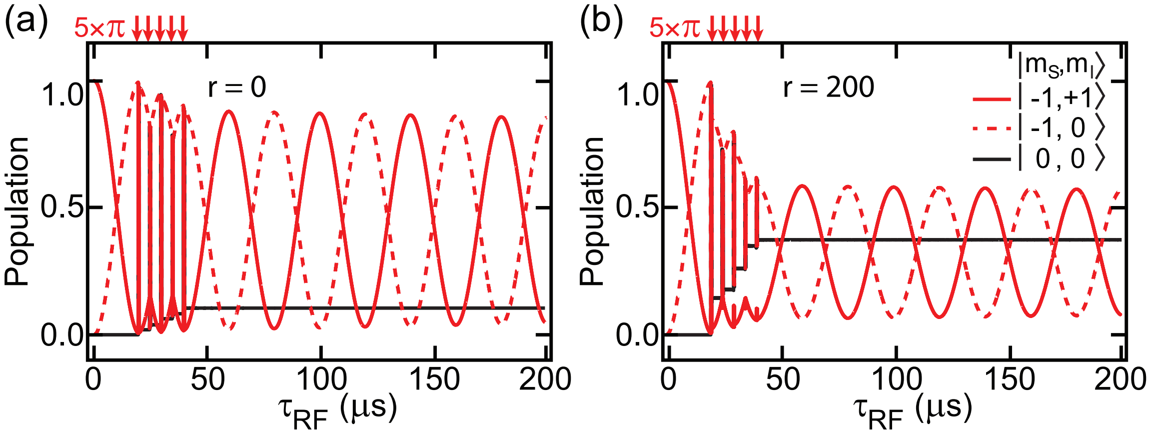

Figure 4.8: The effects of an off-axis RF field: Simulated time evolution of the nuclear Rabi oscillations with 5 π-phase gates applied every 5 μs from 20 μs to 40 μs. (a) Population as a function of τ_{RF} with no B_z component from the RF drive ($r = 0$), showing minimal population trapping in $|m_S, m_I\rangle = |0, 0\rangle$. (b) Population as a function of τ_{RF} with slow energy level shifting due to B_z from the RF drive ($r = 200$), showing a significant decrease in the Rabi oscillation amplitude due to population being trapped in $|0, 0\rangle$.

the fast phase gates leaves some residual population in $|0, 0\rangle$. We account for this effect using the second term in Eq. 4.3 with $r = 200$, a value of similar order to the ratio between the electron and nuclear magnetic moment, taking into account the electron-nuclear flip-flop enhancement discussed in the main text [36]. This is equivalent to the drive field being ~ 23° from the NV axis ($B_{\mathrm{RF},z} = 3.6$ G).

We argue that the additional population in $|0, 0\rangle$ does indeed contribute to a "dark" readout. Typically the $m_S = 0$ population would contribute to a "bright" readout, as the cycling transition associated with $m_S = 0$ does not involve the intersystem crossing through the singlet state ${}^1A_1$. However, near the ESLAC, $|0, 0\rangle$ is strongly coupled to $|-1, +1\rangle$ in the excited state manifold. In contrast to the experiment performed by Morton *et al.* [68, 69] where the nuclear spin is initialized using thermal polarization, it is precisely this coupling that makes the nuclear spin polarization possible for our experiment as it allows for Larmor precession between the two states near the ESLAC during optical excitation. Thus, $|0, 0\rangle$ can be converted to $|-1, +1\rangle$ and contribute to a dark state during optical readout due to the non-radiative decay of $|-1,+1\rangle$ through the singlet state. This sequence of events, which is part of the nuclear spin polarization process, occurs on the same ~ 300 ns timescale as the optical readout [75]. Details of the dark state population and readout are given in Appendix C.

Finally, we show that the population loss is indeed associated with the application of RF pulses. We perform a Ramsey experiment [see Fig. 4.7(d)] and interrupt the free evolution by applying multiple π-phase gates. Within our measurement error, there is no visible decay of the Ramsey fringe amplitude after the phase gates are applied. These measurements indicate that there is no population loss after many phase gates have been applied during the time when the RF field is turned off.

4.8 Summary

In conclusion, we have demonstrated fast phase gate operations on a nuclear spin qubit in diamond by driving electronic spin transitions of a NV center. π-phase gates are achieved in 462 ns, approximately 100 times faster than the bare nuclear Rabi frequency. These fast phase gates can be applied repeatedly to preserve the nuclear spin state, providing an alternative method for decoupling the nuclear spin from static environments.

Chapter 5

Hyperfine-Enhanced Gyromagnetic Ratio of a Nuclear Spin in Diamond

5.1 Introduction

Advancements in quantum computation have been accelerated by the development of qubits with high fidelity quantum control and long quantum coherence times [77, 78]. The nuclear spin degree of freedom has long been considered to be a good candidate for a qubit [79–81]. Since the nuclear spin has a relatively small gyromagnetic ratio $\gamma_N = g_N \mu_N$ compared to that of an electron (approximately 1000× smaller), it is well-protected from decoherence sources in the environment. Impressive coherence times up to six hours have been achieved in solid-state systems using the nuclear spin as a quantum memory [10, 12, 39, 66, 67, 82].

Despite the long coherence time, fast nuclear spin manipulation is difficult as the small gyromagnetic ratio of the nuclear spin also isolates the spin from the control fields. Several experiments on NV centers have shown that nuclear spins coupled to a

NV center can exhibit Rabi oscillations that are significantly faster than the expected oscillations of a bare nuclear spin that is driven by the same ac magnetic field [see Chapter 4]. This faster rotation rate can be interpreted as an enhancement of the effective nuclear gyromagnetic ratio ($\gamma_{N,\text{eff}}$) that results from hyperfine interactions with the NV electronic spin in the ground state. The enhancement factor of ~ 20 is typically achieved at the ESLAC, where the nuclear spin can be optically polarized [30,36,57].

In this chapter, we extend these earlier experiments and show that the enhancement of the nuclear spin gyromagnetic ratio in the NV system is widely tunable by varying the electronic spin transition frequency. The enhancement is observed by directly measuring the nuclear spin Rabi frequency as a function of ac magnetic field drive amplitude and comparing to the value expected from a bare nuclear spin driven under the same conditions. The result is in good agreement with the theoretical predictions [83]. We carefully study the behavior near the ground state level anti-crossing (GSLAC), where the enhancement is maximized. We demonstrate enhancements as large as 2000, a more than two orders of magnitude improvement over previous experiment.

Naturally, the increased control speed comes with the cost of faster spin decoherence. We therefore measure the dephasing rate of the nuclear spin as a function of the external magnetic field near the GSLAC. Our results show that the dephasing rate in our experimental setting is limited by fluctuations in the dc magnetic field, which is amplified due to the increased effective nuclear spin gyromagnetic ratio at the GSLAC.

5.2 Enhancement of the Nuclear Gyromagnetic Ratio in a NV Center

Coherent dynamics of the coupled electron and nuclear spins in the NV system have been demonstrated in reference [36], where Childress *et al.* observed an enhanced Larmor precession frequency of ^{13}C nuclear spins in close proximity to the NV center. The enhancement factor, $\alpha \equiv \gamma_{N,\mathrm{eff}}/\gamma_{N,\mathrm{bare}}$, explained by second-order perturbation theory, however, is sensitive to the external magnetic field and increases rapidly near the GSLAC. Recently, the exact expression of the enhancement has been presented in reference [83]. We briefly describe their derivation in this section.

The enhancement of the effective nuclear gyromagnetic ratio can be understood by considering the NV center Hamiltonian given by Eq. 2.2. We can separate the Hamiltonian H into secular terms (terms that commute with S_z) H_0, and non-secular terms V as:

$$H_0/h = DS_z^2 + g_e\mu_B B_z S_z - g_N\mu_N \vec{B}\cdot\vec{I} + \sum_{j=x,y,z} S_z A_{zj} I_j, \tag{5.1}$$

$$V/h = \frac{1}{2}\left(g_e\mu_B(B_-S_+ + B_+S_-) + \sum_{j=x,y,z}(S_+A_{-j}I_j + S_-A_{+j}I_j)\right). \tag{5.2}$$

Here the raising and lowering operators are defined as $B_\pm = B_x \pm iB_y$, $S_\pm = S_x \pm iS_y$, $A_{\pm j} = A_{xj} \pm iA_{yj}$. The perpendicular hyperfine terms $A_{xx} = A_{yy} = A_\perp = 3.65$ MHz mix the states with zero-quantum (ZQ) transitions, specifically $|m_S, m_I\rangle = |0,-\frac{1}{2}\rangle \leftrightarrow |-1,+\frac{1}{2}\rangle$ and $|+1,-\frac{1}{2}\rangle \leftrightarrow |0,+\frac{1}{2}\rangle$. Chen *et al.* [83] showed that the Hamiltonian can be diagonalized by rotating the two ZQ subspaces with a unitary transformation $U_{\mathrm{ZQ}} = e^{-i(\sigma_y^-\vartheta^- + \sigma_y^+\vartheta^+)}$, where $\sigma_y^+ = i(|+1,-\frac{1}{2}\rangle\langle 0,+\frac{1}{2}| - |0,+\frac{1}{2}\rangle\langle +1,-\frac{1}{2}|)$, $\sigma_y^- = i(|0,-\frac{1}{2}\rangle\langle -1,+\frac{1}{2}| - |-1,+\frac{1}{2}\rangle\langle 0,-\frac{1}{2}|)$ and the rotation angles are given by:

$$\tan(2\vartheta^{+}) = \frac{2A_{\perp}}{D + g_e\mu_B B_z - g_N\mu_N B_z - A_{zz}/2}, \tag{5.3}$$

$$\tan(2\vartheta^{-}) = \frac{-2A_{\perp}}{D - g_e\mu_B B_z + g_N\mu_N B_z - A_{zz}/2}. \tag{5.4}$$

By applying the transformation U_{ZQ} on the interaction Hamiltonian in the rotating frame, $H_{\mathrm{RF}} = B_{\mathrm{RF}}(g_e\mu_B S_x + g_N\mu_N I_x)$, and keeping only the terms that contribute to nuclear spin flips, one can obtain

$$\begin{aligned}\hat{H}_{\mathrm{RF}} &= U_{\mathrm{ZQ}} H_{\mathrm{RF}} U_{\mathrm{ZQ}}^{\dagger} \\ &= g_N\mu_N B_{\mathrm{RF}}\bigg(\alpha_{+1}|+\hat{1}\rangle\langle+\hat{1}| + \alpha_0|\hat{0}\rangle\langle\hat{0}| + \alpha_{-1}|-\hat{1}\rangle\langle-\hat{1}|\bigg)I_x.\end{aligned} \tag{5.5}$$

Here α_{m_S} represents the enhancement factors in each of the NV electronic spin manifold m_S and their exact expressions are given by:

$$\alpha_{+1} = \cos(\vartheta^{+}) + \frac{g_e\mu_B}{g_N\mu_N}\sin(\vartheta^{+}), \tag{5.6}$$

$$\alpha_0 = \cos(\vartheta^{+})\cos(\vartheta^{-}) - \frac{g_e\mu_B}{g_N\mu_N}\sin(\vartheta^{+} - \vartheta^{-}), \tag{5.7}$$

$$\alpha_{-1} = \cos(\vartheta^{-}) - \frac{g_e\mu_B}{g_N\mu_N}\sin(\vartheta^{-}). \tag{5.8}$$

In contrast to the second-order perturbation theory, where the enhancement α_{-1} is infinite near the GSLAC, these exact expressions predict a finite enhancement near the GSLAC with the maximum value of $\alpha_{-1} \approx \frac{g_e\mu_B}{\sqrt{2}g_N\mu_N}$. However, it is still unclear what ultimately limits the nuclear spin control speed near the GSLAC, where the enhancement is maximized. Therefore, we carefully measure the enhancements near the GSLAC, compare our measurements and theory, and investigate how this enhancement of the nuclear spin gyromagnetic ratio affects the nuclear spin coherence time.

5.3 Methods

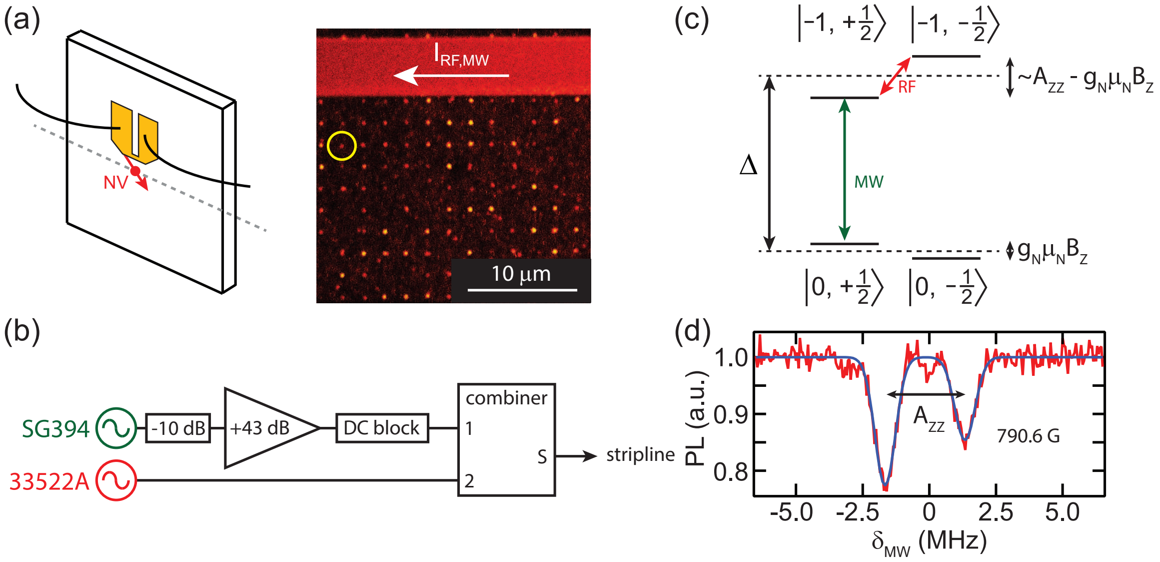

Figure 5.1: (a) Schematic of the setup and a confocal image of the sample implanted with ^{15}N. The circle indicates the NV used in this experiment. An on-chip Ti/Au stripline was fabricated on the sample to drive MW and RF control pulses on the NV center. A permanent magnet was aligned to produce a static magnetic field along the NV axis $\hat{z}$, indicated by the red arrow. (b) Circuit diagram: Two signal generators, SRS SG394 and Agilent 33522A, are used to generate MW and RF pulses, respectively. The signals are combined with a resistive splitter/combiner before being delivered to the sample. (c) NV center energy level diagram: The electronic spin levels $m_S = 0$ and $m_S = -1$ are separated by $\Delta = D - g_e \mu_B B_z$. A selective MW pulse is tuned to resonance with the $|m_S, m_I\rangle = |0, +\frac{1}{2}\rangle$ to $|-1, +\frac{1}{2}\rangle$ transition for initialization and readout of the nuclear spin qubit. A RF pulse is tuned to resonance with the $|-1, +\frac{1}{2}\rangle$ to $|-1, -\frac{1}{2}\rangle$ transition to drive nuclear spin Rabi oscillations. (d) PL as a function of $\delta_{\mathrm{MW}} = \nu_{\mathrm{MW}} - \Delta$ showing the electronic spin transitions associated with each nuclear spin projection.

Our quantum system consists of a NV electron spin and the intrinsic ^{15}N $I = 1/2$ nuclear spin. The sample is an electronic grade diamond (Element Six). The NV centers are created via 20 kV ion implantation of ^{15}N atoms into the 100-nm, isotopically enriched layer (^{12}C > 99.99 %) that is grown on top of the bulk sample [25]. The implantation depth is estimated to be ~ 25 nm from Stopping and Range of Ions in Matter (SRIM) simulations [52]. The schematic of the experimental setup is illustrated in Fig. 5.1(a). We select a suitable single NV center using a room-temperature confocal microscope with a 532 nm excitation laser. PL from the NV center is collected using a high numerical aperture (NA = 0.95) objective and directed towards single photon detectors using a combination of the fiber and free space optics [57]. The dc magnetic field along the NV axis is controlled by the combination of a permanent magnet mounted on a 3-axis translation stage and of electromagnets that are aligned perpendicular to the NV axis. Off-axis magnetic field components arising from misalignment of the permanent magnet are compensated using these electromagnets with an accuracy better than 0.1 G. The ac magnetic field is delivered to the sample via a Ti/Au stripline that is fabricated on the diamond surface. MW and RF pulses are applied through this stripline to drive electronic and nuclear spin rotations. The circuit diagram is shown in Fig. 5.1(b). A SRS SG394 (Aglient N5181A) signal generator is used to generate MW (RF) pulses. The MW signal is amplified with a broadband amplifier (Triad RF TA1003) to allow for fast manipulation of the electronic spin. MW and RF signals are combined with a resistive splitter-combiner before they are delivered to the sample. We calibrate the magnetic field amplitude of the RF pulse, B_{RF}, by performing ac magnetic field sensing with electron spin echo.

The energy level diagram of our system is depicted in Fig. 5.1(c). We select two well-isolated sublevels $|m_S, m_I\rangle = |-1, +\frac{1}{2}\rangle$, $|-1, -\frac{1}{2}\rangle$ to demonstrate nuclear spin rotations. The two states can be addressed with a RF pulse (frequency $\nu_{\mathrm{RF}} \sim 3$ MHz) driving a direct NMR transition. To read out the nuclear spin state, we map the nuclear spin state to the electronic spin state by applying a selective MW π-pulse (frequency ν_{MW}) tuned to resonance with the $|-1, +\frac{1}{2}\rangle \leftrightarrow |0, +\frac{1}{2}\rangle$ transition at the end of the nuclear spin control sequence. The electronic spin state is then read out by optical excitation [30, 39].

To probe the electronic spin transition frequencies, we performed ODMR spectroscopy by applying pulsed MW excitation with varying frequency ν_{MW} and monitoring the PL during a subsequent laser excitation. When ν_{MW} is on resonance with an electronic transition, we observe a dip in the PL intensity as a result of the population transfer from $m_S = 0$ to $m_S = -1$. Figure 5.1(d) shows an example of a PL spectrum measured as a function of the MW detuning $\delta_{\mathrm{MW}} = \nu_{\mathrm{MW}} - \Delta$ relative to the electronic spin splitting $\Delta = D - g_e\mu_B B_z = 654.8$ MHz ($B_z = 790.6$ G). The two resonances are separated by the hyperfine coupling to the ^{15}N nuclear spin, $A_{zz} = 3.03$ MHz [59].

To calibrate the amplitude of the field $\vec{B}_{\mathrm{RF}}$, we perform ac magnetic field sensing using an electron spin echo technique. The geometry of our sample is depicted in Fig. 5.2(a). The orientation of our stripline provides $\vec{B}_{\mathrm{RF}}$ along the xz-plane at the NV center used in this experiment. We perform spin echo measurement on the electronic spin while simultaneously applying a RF pulse during the free precession time of the electron. The experimental sequence of our spin echo sensing scheme is depicted in Fig. 5.2(b). The final pulse was set to either a $\pi/2$-pulse or a $3\pi/2$-pulse and the results were subtracted to obtain the spin echo contrast. This spin echo scheme provides an advantage over a Ramsey-type pulse sequence by canceling out all the quasi-static magnetic fields on the time scale of the free evolution time τ. We adjust τ to match the period of the RF pulse $\nu_{\mathrm{RF}}\tau = 1$, so that the phase accumulation $\Delta\phi$ from the RF pulse is maximized. With this choice of free evolution time, $\Delta\phi$ is given by [21]:

$$\Delta\phi = 2 \times \int_0^{\tau/2} g_e\mu_B B_{\mathrm{RF},z} \sin(2\pi\nu_{\mathrm{RF}}t)dt = 4\left(\frac{g_e\mu_B}{2\pi}\right) B_{\mathrm{RF},z}\tau. \tag{5.9}$$

We perform this ac magnetic field sensing at $B_z = 912.8$ G, a field intermediate between the ESLAC and the GSLAC, where nuclear spin is not polarized. We choose $\nu_{\mathrm{RF}} = 2.0$ MHz, far detuned from the NMR frequency $\nu_{\mathrm{NMR}} = 2.626$ MHz. This corresponds to $\tau = 0.5$ μs, much shorter than the coherence time of the electronic spin of the NV center in an isotopically purified substrate, as shown by the lack of any spin echo decay during this time when no RF is applied [see Fig. 5.2(c)]. Fixing

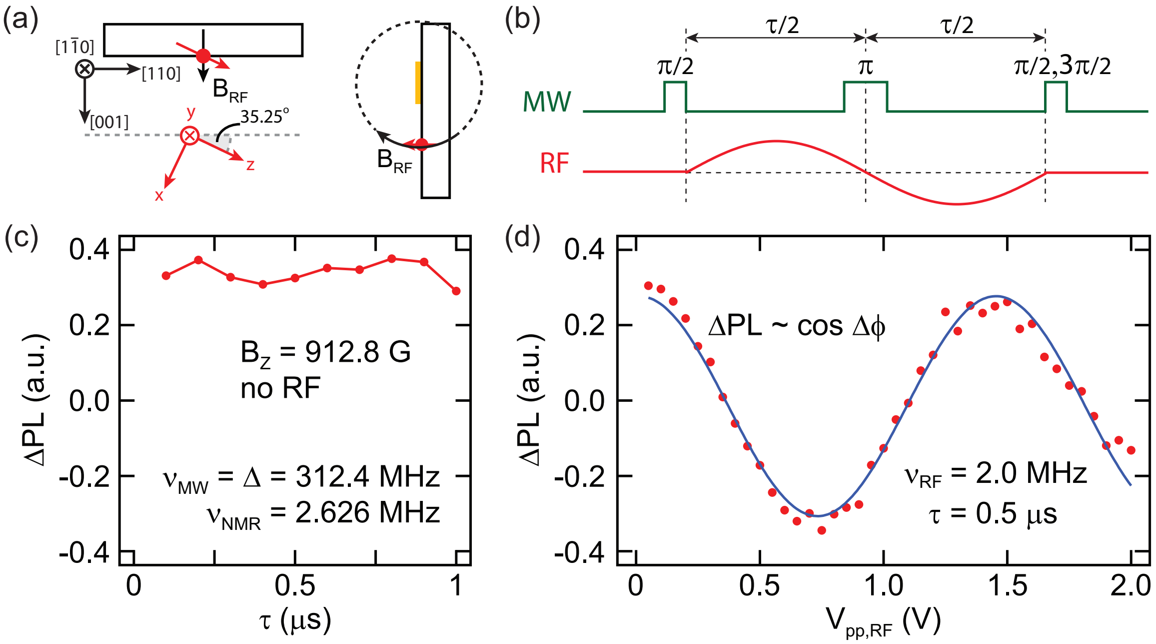

Figure 5.2: (a) Geometry of the sample: An on-chip stripline is fabricated such that the magnetic field $\vec{B}_{\mathrm{RF}}$ is directed perpendicular to the (100) surface of the diamond. (b) Spin echo sequence for sensing B_{RF}: An RF pulse is applied immediately after the preparation of the electronic spin superposition state and the free precession time τ is chosen to match the RF pulse period. (c) Standard spin echo signal showing no decay of the PL contrast ΔPL for $\tau < 1$ μs with no RF applied. (d) Spin echo contrast at $\tau = 0.5$ μs with 2 MHz RF applied. The phase accumulated results in modulation of the spin echo contrast.

$\tau = 0.5$ μs, we apply the RF pulse and monitor ΔPL as a function of RF amplitude $V_{\mathrm{pp,RF}}$. This results in the modulation in the spin echo contrast according to the phase accumulated, projected on to the z-axis of the Bloch sphere, $\Delta\mathrm{PL} \sim \cos\Delta\phi$.

Figure 5.2(d) shows the modulation from the ac magnetic field sensing scheme. From the cosine fit, we obtain $\Delta\phi = 4.36\ \mathrm{rad/V_{pp}}$, corresponding to $B_{\mathrm{RF},z} = 0.78\ \mathrm{G/V_{pp}}$. Considering the geometry from the sample orientation ({100}-face, ⟨110⟩ edge) [see Fig. 5.2(a)], we then obtain the magnitude of $B_{\mathrm{RF},x} = 1.10\ \mathrm{G/V_{pp}}$.

5.4 Nuclear Rabi Oscillations and the Effective Nuclear Gyromagnetic Ratio

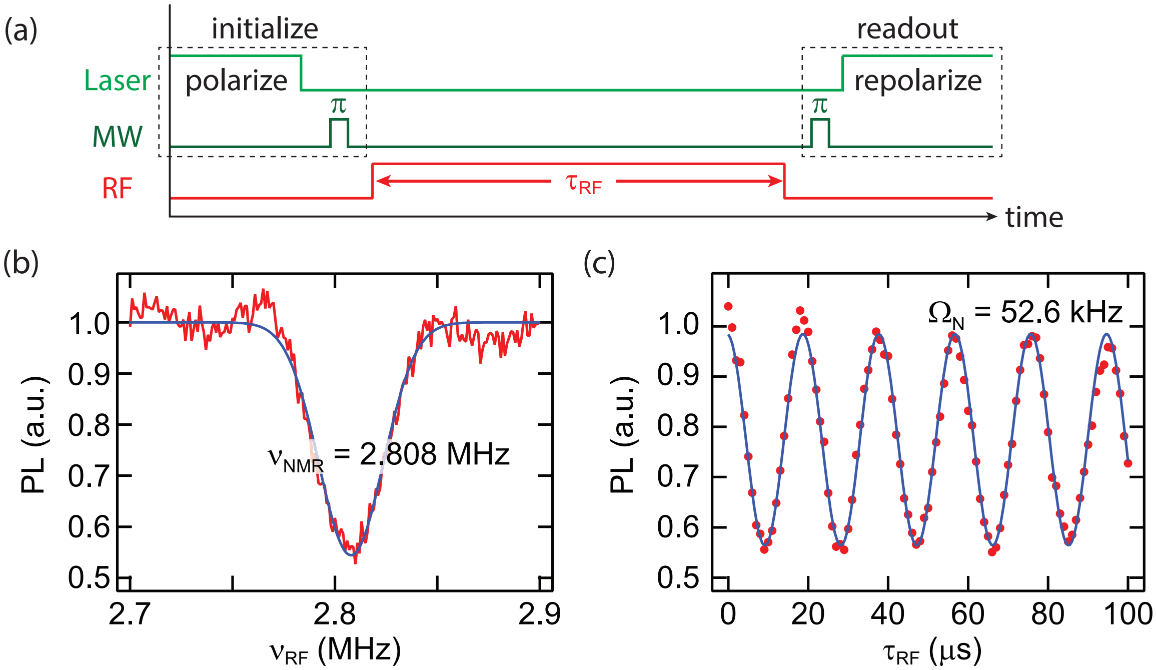

Figure 5.3: (a) Pulse sequence for NMR spectroscopy and nuclear Rabi oscillations. The nuclear spin is initialized with the application of a laser pulse, followed by a selective MW π-pulse. Nuclear Rabi oscillations are driven by a RF pulse (duration $\tau_{\rm RF}$). At the end, another selective MW π-pulse is applied to map the nuclear spin state to the electronic spin state before an optical readout. (b) A sample of NMR spectroscopy, taken at the ESLAC (512.3 G). The data shows PL plotted as a function of $\nu_{\rm RF}$. We observe a decrease in PL when $\nu_{\rm RF}$ is on resonance with an NMR transition. (c) A sample of nuclear Rabi oscillations, taken at the ESLAC (512.3 G). The data shows a sinusoidal modulation of PL as a function of $\tau_{\rm RF}$ corresponding to the Rabi oscillations.

We perform nuclear Rabi experiments with the pulse sequence illustrated in Fig. 5.3(a). We start by optically pumping the electron and nuclear spins with a 4-μs long 532 nm laser pulse [2]. After the system is polarized into the $|0, +\frac{1}{2}\rangle$ state, a selective MW π-pulse is applied to transfer the population to the $|-1, +\frac{1}{2}\rangle$ state, completing the initialization process. We then drive nuclear spin Rabi oscillations by applying a RF pulse with varying duration $\tau_{\rm RF}$ resonant with the $|-1, +\frac{1}{2}\rangle$ to $|-1, -\frac{1}{2}\rangle$ transition. We note that while the nuclear Rabi oscillation contrast is maximized at the ESLAC, as the optical polarization is most effective, we can still obtain nuclear Rabi oscillations with a reduced contrast away from ESLAC, where imperfect optical polarization occurs. Finally, optical readout is performed by applying another selective MW π-pulse that converts the population from $|-1,+\frac{1}{2}\rangle$ to the bright state $|0,+\frac{1}{2}\rangle$. This yields a PL signal that is proportional to the $|-1,+\frac{1}{2}\rangle$ population at the end of the pulse sequence.

We probe the nuclear spin transition frequency ν_{NMR} using this same pulse sequence. Using low RF power, the nuclear spin rotation is only effective when ν_{RF} is close to ν_{NMR}. Figure 5.3(b) shows PL as a function of ν_{RF} at $B_z = 512.3$ G, showing the decrease in PL at $\nu_{\mathrm{RF}} = \nu_{\mathrm{NMR}} = 2.808$ MHz. Then, we perform nuclear Rabi nutations by varying the RF duration τ_{RF}. Typical nuclear spin Rabi oscillations with $B_{\mathrm{RF},x} = 6.6$ G are shown in Fig. 5.3(c). The nuclear Rabi frequency $\Omega_N = 52.6$ kHz we extract from the data exceeds the expected value from a bare nuclear spin $\Omega_{N,\mathrm{bare}} = g_N \mu_N B_{\mathrm{RF},x} = 2.85$ kHz by a factor of ~ 18.5, indicating an enhancement of the effective nuclear gyromagnetic ratio.

Plotting the nuclear Rabi frequency Ω_N as a function of $B_{\mathrm{RF},x}$ for a series of dc magnetic fields B_z (see Fig. 5.4(a),(b)), we see that for each value of B_z, Ω_N scales linearly with $B_{\mathrm{RF},x}$. As the Rabi frequency increases beyond $\Omega_N \sim 1$ MHz, the scaling starts to deviate from the linear behavior and saturates at $\Omega_N \sim 1.5$ MHz before the dynamics become non-sinusoidal (see Section 5.5 for details.). We attribute this saturation to the breakdown of the rotating wave approximation when Ω_N is comparable to the hyperfine splitting A_{zz}. We extract the effective nuclear gyromagnetic ratio $\gamma_{N,\mathrm{eff}}$ by linear fitting the data and obtaining the slopes. Fitting of each data set is extended to the largest values of $B_{\mathrm{RF},x}$ where the fit maintains over 95% confidence ($R^2 > 0.9975$). The data also confirms the dc magnetic field is well aligned with the NV axis, as there is no visible offset at $B_{\mathrm{RF},x} = 0$ that would result from an off-axis magnetic field B_x, B_y.

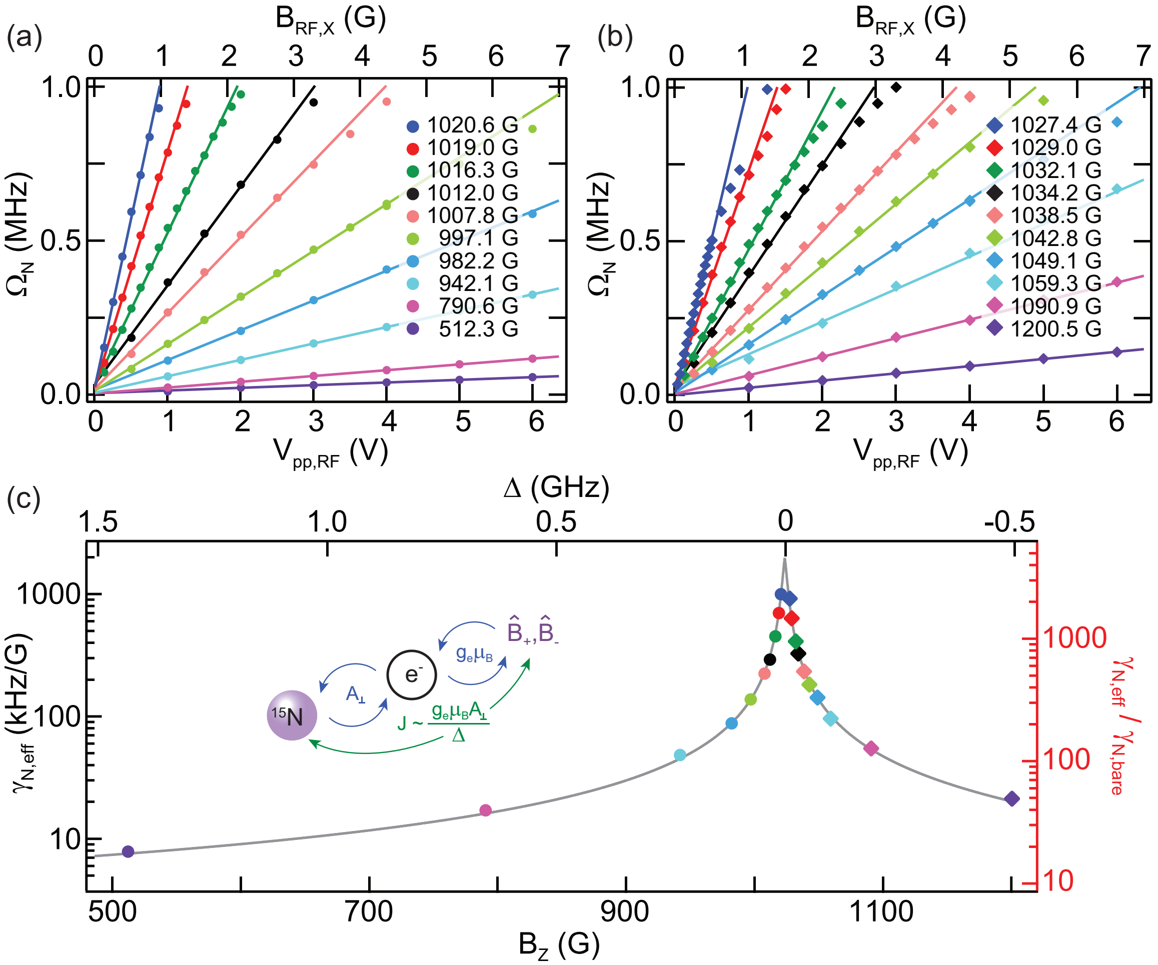

Figure 5.4: Nuclear spin Rabi frequency Ω_N as a function of RF amplitude $V_{\text{pp,RF}}$ (a) below the GSLAC and (b) above the GSLAC. (c) Extracted nuclear gyromagnetic ratio $\gamma_{N,\text{eff}}$ from (a) and (b). The grey curves show $\gamma_{N,\text{eff}}$ calculated from the theory described in Section 5.2. (Inset) The coupling mechanism in analogy to the cQED architecture. Here the electronic spin acts in place of a cavity, mediating the coupling between the nuclear spin and the ac magnetic field.

In Fig. 5.4(c) we plot $\gamma_{N,\text{eff}}$ extracted from the slopes in Fig. 5.4(a),(b) as a function of B_z. We achieved enhancements $\gamma_{N,\text{eff}}/\gamma_{N,\text{bare}}$ exceeding 2000 near the GSLAC ($\Delta \sim 10$ MHz), making it possible to perform a full nuclear spin 2π rotation within a microsecond with less than 1 mW of RF power applied to the stripline. This enhancement is more than two orders of magnitude greater than the results obtained on NVs at lower magnetic fields near the ESLAC [30] and is in excellent agreement with the expression given in equation 5.8, where the theoretical maximum enhancement is $\alpha_{-1} \approx \frac{g_e \mu_B}{\sqrt{2} g_N \mu_N} \approx 4600$.

The enhancement of the nuclear gyromagnetic ratio is analogous to the two-qubit interactions in the circuit quantum electrodynamics (cQED) architecture, where two qubits can be coupled via the exchange of virtual photons through a microwave cavity [84, 85]. The effective coupling rate $J \sim g_1 g_2 / \Delta_{\mathrm{cQED}}$, is a function of the individual coupling strength of each qubit to the cavity (described by g_1 and g_2) and the qubit-cavity detuning Δ_{cQED} [86]. Here our NV electronic spin acts in place of the cavity, mediating the coupling between the nuclear spin (qubit 1, coupling strength $g_1 \sim A_\perp$) and the ac magnetic field ("qubit 2", coupling strength $g_2 \sim g_e \mu_B$). The detuning is set by the energy difference Δ between the $m_S = 0$ and $m_S = -1$ states.

5.5 Strong Driving Limit of Nuclear Rabi Oscillations

As the amplitude of the RF field driving the NMR transition increases, we found that while the nuclear Rabi frequency can increase beyond $\Omega_N \sim 1$ MHz, the scaling of the Rabi frequency as a function of the drive amplitude starts to deviate from the expected linear behavior and saturates at $\Omega_N \sim 1.5$ MHz, as shown in Fig. 5.5(a),(b).

In addition to this saturation behavior, we also observe that the dynamics become non-sinusoidal at strong driving field. Figure 5.5(c) shows nuclear Rabi oscillations obtained near the GSLAC ($B_z = 1027.4$ G, $\Delta = 8.8$ MHz) where we obtain standard sinusoidal behavior with the drive amplitude $B_{\mathrm{RF},x} = 0.83$ G. As we increase the drive amplitude to $B_{\mathrm{RF},x} = 1.24$ G, the dynamics of the nuclear spin oscillations become non-sinusoidal, as shown in Fig. 5.5(d). We attribute this to the breakdown of the rotating wave approximation, and to the fact that our RF field contains both $B_{\mathrm{RF},x}$ and $B_{\mathrm{RF},z}$. Near the GSLAC, the z-component $B_{\mathrm{RF},z}$ can also contribute to

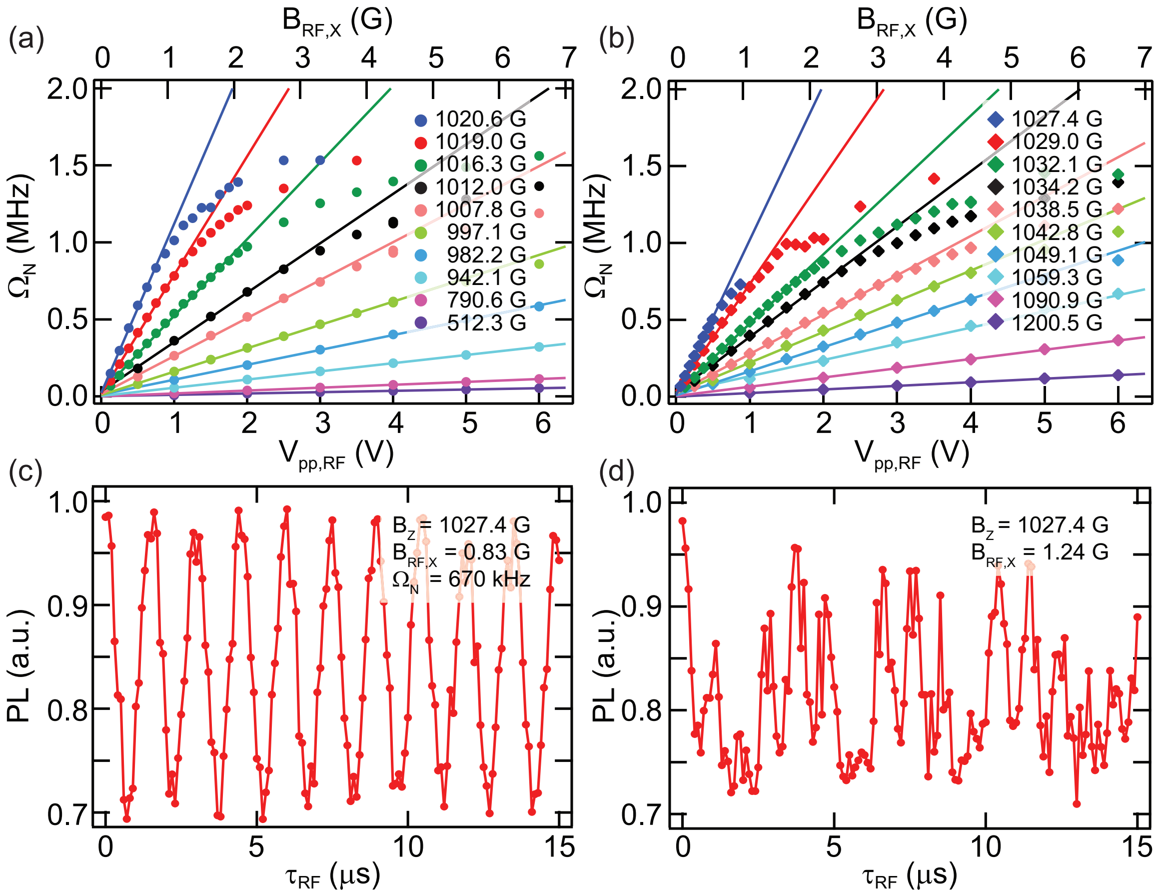

Figure 5.5: Nuclear spin Rabi frequency Ω_N as a function of RF amplitude $V_{\text{pp,RF}}$ (a) below the GSLAC and (b) above the GSLAC, showing the saturation behavior around $\Omega_N \sim 1.5$ MHz. (c) Nuclear Rabi oscillations obtained close to the GSLAC with a small drive amplitude are sinusoidal. (d) Non-sinusoidal behavior is observed at the same dc magnetic field as in (c), but with a larger drive amplitude.

the level shifts of both ESR and NMR transitions. This effect can result in a more complicated Landau-Zener-like dynamics. In principle, the complicated dynamics could be mitigated by engineering the sample geometry such that the RF field is perpendicular to the NV axis [12].

5.6 Nuclear Spin Dephasing

While the largest enhancement of the nuclear gyromagnetic ratio is obtained near the GSLAC, where the nuclear spin can also be polarized via optical pumping, the GSLAC spin mixing responsible for nuclear polarization also affects the coherence time of the nuclear spin. We therefore investigate the behavior at the GSLAC by examining the coherence of the nuclear spin via nuclear spin Ramsey experiments.

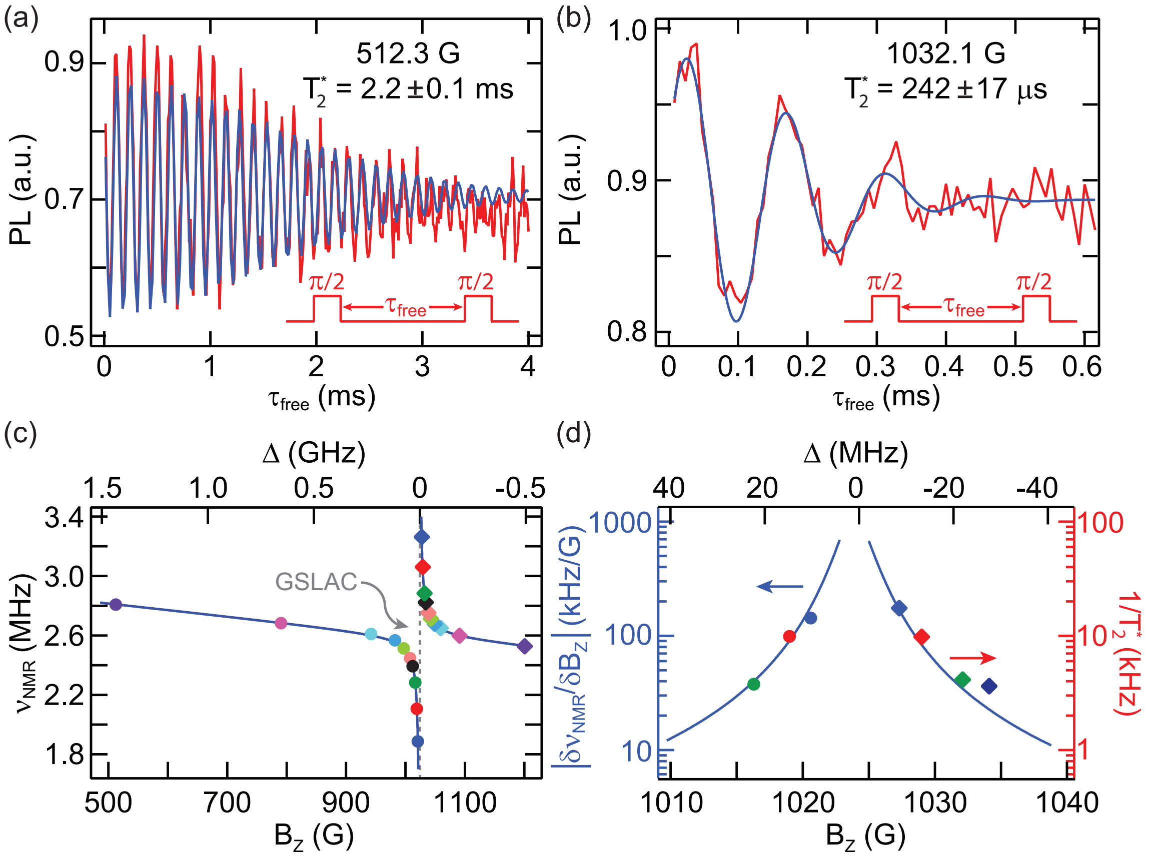

Figure 5.6: Nuclear Ramsey fringes acquired at (a) $B_z = 512.3$ G and (b) $B_z = 1032.1$ G show a reduction of T_2^* near the GSLAC. The data are fitted with a sinusoidal function with Gaussian decay $\mathrm{PL}(\tau_{\mathrm{free}}) \propto e^{-(\tau/T_2^*)^2} \cos(2\pi\nu\tau_{\mathrm{free}} + \phi)$. (c) NMR Frequency ν_{NMR} as a function of B_z showing a nonlinearity near the GSLAC. Each data point is labeled according to the data sets in Fig. 5.4. Blue curves show the theoretical values derived by diagonalizing the NV Hamiltonian. (d) Blue curves: The derivative of the NMR frequency shown in (c) with respect to the magnetic field $|\delta\nu_{\mathrm{NMR}}/\delta B_z|$ characterizes the sensitivity of the nuclear spin to the magnetic field along the NV z-axis. The data points show the dephasing rate $1/T_2^*$ extracted from Ramsey experiments. The increase in the nuclear spin dephasing rate is in good agreement with the increase in magnetic field sensitivity.

Here, after initialization of the nuclear spin, a RF $\pi/2$-pulse on resonance with ν_{NMR} is applied to create a superposition state $\frac{1}{\sqrt{2}}(|-1,+\frac{1}{2}\rangle+|-1,-\frac{1}{2}\rangle)$. The state is then allowed to freely precess for a duration τ_{free} before another RF $\pi/2$-pulse rotates the nuclear spin state back to the measurement basis. We manually shift the phase of the second RF $\pi/2$-pulse linearly as a function of τ_{free}, relative to the first pulse, to create visible Ramsey fringes.

Figures 5.6(a–b) show the nuclear spin Ramsey data at the ESLAC (512.3 G) and the GSLAC (1032.1 G), respectively. From each data set, we extracted the dephasing time T_2^* from the gaussian decay envelope. We found that while the change in the external magnetic field from the ESLAC to the GSLAC results in over a 50× improvement of the effective nuclear spin gyromagnetic ratio, it also results in a 10× increase in the nuclear spin dephasing rate $1/T_2^*$.

This increased nuclear spin dephasing rate can be explained by considering the inhomogeneous broadening of the nuclear spin transition (frequency ν_{NMR}). Near the GSLAC, hybridization of electronic and nuclear spins results in a NMR frequency shift that deviates from a simple linear nuclear Zeeman shift, as shown in Fig. 5.6(c). This hybridization causes a significant increase in the effective longitudinal gyromagnetic ratio $|\delta\nu_{\mathrm{NMR}}/\delta B_z|$ around the GSLAC. As a consequence, the nuclear spin suffers larger inhomogeneous broadening from the same dc magnetic field fluctuation and thus results in the shorter T_2^*. Figure 5.6(d) shows that the increase in the dephasing rate $1/T_2^*$ is in good agreement with the increase in $|\delta\nu_{\mathrm{NMR}}/\delta B_z|$, confirming that our T_2^* is limited due to dc magnetic field fluctuations $|\delta B_z| \sim 0.1$ G. This is attributed to the thermal drift from ~ 0.05 °C room temperature fluctuations.

5.7 Summary

We have shown that the effective nuclear spin gyromagnetic ratio can be greatly enhanced due to hyperfine coupling of the nuclear spin to the NV electronic spin. The enhancement is well described by diagonalizing the Hamiltonian and is analogous to cavity-mediated qubit couplings in cQED. Our approach is also applicable to other coupled electron-nuclear spin systems, such as phosphorous donors in silicon or rare-earth ion dopants in crystalline hosts [82,87], where it would allow for rapid quantum control of nuclear spins without requiring high RF power. We observe the strongest enhancement near the GSLAC, where we achieve over a factor of 2000 enhancement of the effective nuclear gyromagnetic ratio over the bare nuclear gyromagnetic ratio. Ultimately, as the enhancement increases rapidly near the GSLAC, the spin coherence suffers from the inhomogeneous broadening of the NMR frequency and more complicated dynamics occur as the Rabi frequency approaches the NMR frequency.

Chapter 6

Towards Coupling of Bismuth Nuclear Spins to NV Centers

6.1 Introduction

Bismuth, a brittle metal with a colorful iridescent oxide, is the deepest group V donor in silicon. When implanted in silicon, the bismuth donor energy level structure is extremely complicated. Its exotic nuclear spin $I = 9/2$ exhibits a large ground state zero-field splitting. From the strong hyperfine interactions, the energy level structure contains several nonlinear behaviors as a function of magnetic field compared to that of simple spin-$\frac{1}{2}$ linear Zeeman effects. Some of these nonlinear behaviors result in clock transitions, transitions that are first order insensitive to magnetic field fluctuations [88,89]. These transitions, at which the linewidth is narrowed, can be exploited to extend the coherence time of the bismuth nuclear spin memory [90]. NV centers in diamond have been known to serve as a perfect gateway for accessing nearby nuclear spins on a single-spin level. Therefore, in this chapter we explore the potential of coupling single bismuth nuclear spins to a single NV center.

6.2 Implantation Process

We introduce the bismuth atoms into the diamond lattice by means of ion implantation. Bismuth is a heavy element and thus the implantation process is highly destructive to the diamond lattice, posing a major challenge for positioning the bismuth ion close to the NV center. By simulating the implantation parameters with SRIM [52], we can determine the acceleration energy required for the implanted bismuth ions to be at the same depth as the implanted nitrogen ion. The close proximity will allow for the higher chance of observing strong coupling between the electronic spin of the NV center and the nuclear spin of the bismuth ion.

For localization of the implantations in the xy-direction, we use the masked apertures, previously discussed in Chapter 3, to define arrays of implantation sites, with each site being a small cylindrical aperture. We also utilize the shadowing effect that results from the finite implantation mask thickness to reduce the effective xy-aperture area. Most of the NV centers characterized are implanted through 50-nm apertures, defined by electron beam lithography. The shadowing from implantation at a 7° angle results in very small effective aperture area of ~ 200 nm^2. Implantations are performed at Kroko Inc. in a two-step process [see Fig. 6.1(a)]:

1. Implantation of ^{15}N at 5 kV. The choice of ^{15}N allows for a clear distinction of the implanted NV centers from the substrate NV centers.

2. Implantation of ^{209}Bi at 20 kV, which allows placement of the ^{209}Bi ion distribution at the same depth as the ^{15}N ion distribution.

Both implantations are performed at room-temperature with a 7° tilt to reduce ion channeling. The chosen acceleration energies result in an estimated depth of ~ 9 nm from the surface of the diamond [see Fig. 6.1(b)]. This depth is relatively shallow in order to reduce the range of ion straggling, while maintaining sufficient distance from the surface where surface spins can deteriorate the coherence of the NV centers [91].

Following the two-step implantations, the sample is annealed to form NV centers using the methods described in Chapter 3.

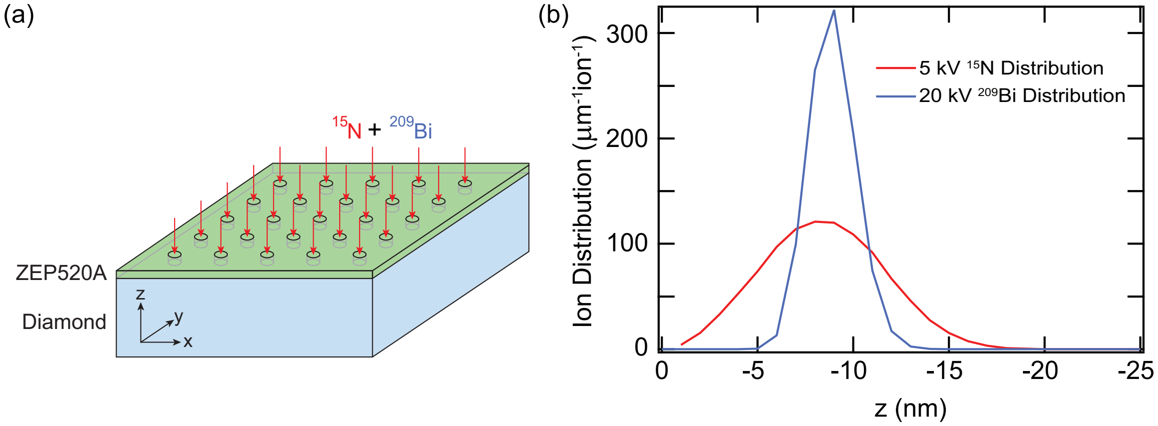

Figure 6.1: (a) Implantation process: Small apertures are patterned using ZEP520A electron beam resist. ^{15}N and ^{209}Bi ions are subsequently implanted through these apertures. The sample is then annealed at 850 °C to form NV centers. (b) Simulation from SRIM showing the z-distribution of the ions for the implantations of ^{15}N and ^{209}Bi. The xy-straggling range follows a similar distribution ($\sim$ 4 nm for ^{15}N and $\sim$ 2 nm for ^{209}Bi).

6.3 Reduction of NV Center Conversion Yields from Bismuth Co-Implantations

For calibration of the NV center yields, we start with an isotopically-enriched substrate (99.99% ^{12}C) [25]. We implant two different regions of the same substrate with the same ^{15}N fluence of 2×10^{12} ions/cm^2 at 5 kV. We then mask off one region and implant the other with ^{209}Bi fluence of 5×10^{13} ions/cm^2 at 20 kV.

In each region, we pattern arrays of 40, 50, 60, and 70 nm apertures using electron beam lithography. For 40-nm apertures, the shadowing effect from the 7° implantation angle and the thickness of the mask (t = 230 nm) results in an extremely small effective aperture area $A < 1$ nm^2 such that the average number of NV centers per site $\bar{n}_{\mathrm{NV}}$ is effectively zero. Therefore, the sites with 40-nm apertures are only used for basic verifications through the confocal microscope image. Any damage to the apertures that takes place due to the implantation of heavy ^{209}Bi ions would result in a large $\bar{n}_{\mathrm{NV}}$ among these sites. Throughout our experiments, we do not observe such behaviors.

From the remaining 50, 60, and 70 nm apertures, we select arrays of 24×24 sites from each aperture size. We carefully characterize the PL from these arrays with the methods described in Chapter 3 and obtain $\bar{n}_{\mathrm{NV}}$ for each array. The results are plotted in Fig. 6.2(a). We then calculate the NV conversion yield by linear fitting the data and dividing the slopes by the ^{15}N implantation fluence.

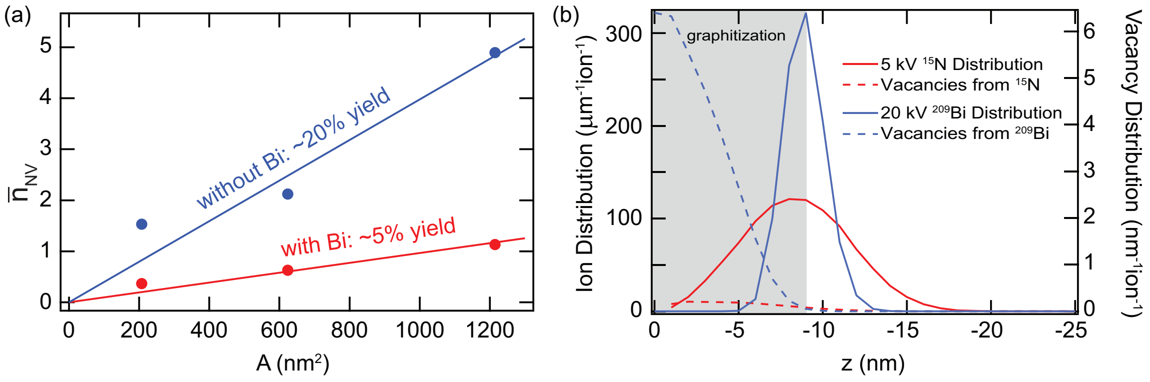

Figure 6.2: (a) The average number of NV centers $\bar{n}_{\mathrm{NV}}$ plotted as a function of the effective implantation aperture area A. The area A is calculated using Eq. 3.1. The regions with co-implantations of ^{209}Bi (fluence 5×10^{13} ions/cm^2) shows a drastic reduction of the NV conversion yield compared to that of the regions without Bi implantations. (b) Simulations from SRIM showing the distribution of ions and vacancies created via ^{15}N and ^{209}Bi implantations. The shaded region indicates the approximate area where graphitization of the diamond can occur. Note the difference in the units between the left axis (ion distribution) and the right axis (vacancy distribution).

From the data in Fig. 6.2(a), we find a significant reduction of the NV conversion yield from 20% to 5% when the ^{209}Bi ions are co-implanted after the ^{15}N ions. We attribute the cause of this reduction to the graphitization of the diamond in the shallow depth as a result of the ^{209}Bi ion damage. Since ^{209}Bi is a heavy element, the density of vacancies created can reach the graphitization threshold of ~ 10 nm^{-3} in diamond, even at relatively low ^{209}Bi fluence. Beyond this threshold, the carbon becomes amorphous and the damage is irreversible even after high-temperature annealing [55]. Figure 6.2(b) shows, in addition to the ion distribution, SRIM simulation results of the vacancy distribution from the implantations of ^{15}N and ^{209}Bi [52]. From the simulation, we find that the density of vacancies increases rapidly for the depths below 9 nm. Therefore, we can expect graphitization to occur in the first 9 nm layer of the diamond surface. This graphitization prevents the NV center formation in the shallow region of the diamond and results in the reduction of the NV conversion yield. However, we may utilize this mechanism to our advantage for obtaining strong coupling between ^{209}Bi nuclear spins and a NV center, as the wider distribution of ^{15}N along the z-axis can be screened out via graphitization. Specifically, it is possible to increase the depth of the ^{209}Bi implantation to overlap with smaller areas of the ^{15}N distribution. The graphitization will ensure that any NV centers created are not in the shallow region, where there is no overlap with the ^{209}Bi ions.

6.4 Characterization of NV Centers with Bi Co-Implantations

After PL characterization of the implanted arrays, we select the implantation sites containing single NV centers via the PL criteria using the methods described in Chapter 3. We then characterize each single NV center via continuous-wave ODMR experiments. The NV centers with ODMR response are then selected for further characterization through Ramsey measurements. For baseline measurements, we select single NV centers in the region without Bi implantation. We perform Ramsey and Hahn echo experiments to measure the dephasing time T_2^* and decoherence time T_2, respectively. From the data, we obtain the average dephasing time $T_2^* \sim 20$ μs and spin echo time $T_{2,\text{echo}} \sim 500$ μs, values typical for shallow NV centers in isotopically-enriched diamond samples [4, 25].

We then proceed to characterize the region with Bi co-implantations. Using Ramsey interferometry [see Section 2.6], we characterize 61 single NV sites in the region implanted with ^{209}Bi fluence of 1×10^{13} ions/cm^2 and 45 single NV sites in the region implanted with ^{209}Bi fluence of 5×10^{13} ions/cm^2. Of the 106 single NV centers in total, we do not observe any set of Ramsey fringes with 20 modulation frequencies, a signature that would be unique to strong coupling to a ^{209}Bi nuclear spin $I = 9/2$ in addition to the intrinsic ^{15}N $I = 1/2$. However, we find a drastic reduction of the dephasing time among these samples. To quantify this, we identify via Ramsey fringes the NV centers without any strong > 1 MHz coupling to additional nuclear spins and measure their dephasing time T_2^*. This choice allows us to measure an unbiased T_2^* in the absence of other strongly-coupled nuclear spins that can contribute to decoherence. Figure 6.3 shows the histograms of T_2^* obtained from the two regions with different ^{209}Bi fluences. We note that the ^{15}N fluence was increased for the higher ^{209}Bi fluence to compensate for the reduction of the NV conversion yield discussed in Section 6.3.

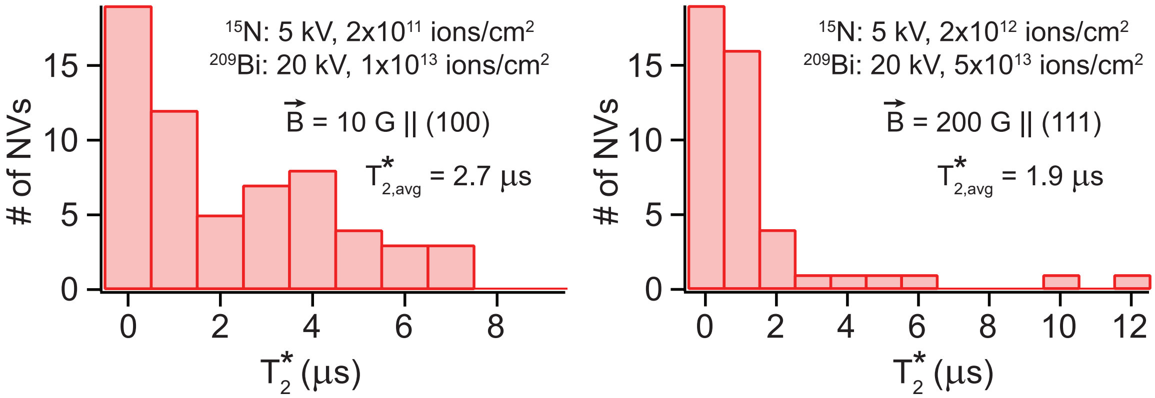

Figure 6.3: (a) Histogram of the dephasing times obtained from 61 NV centers co-implanted with a low Bi fluence of 1×10^{13} ions/cm^2, measured at a magnetic field $B = 10$ G applied along the (100)-direction of the diamond sample. From the data, we obtain an average dephasing time $T_{2,\text{avg}}^* = 2.7$ μs. (b) Histogram of the dephasing times obtained from 45 NV centers co-implanted with a high Bi fluence of 5×10^{13} ions/cm^2, measured at a magnetic field $B_z = 200$ G applied along the NV axis in the (111)-direction of the diamond. Despite the better magnetic field conditions, the average dephasing time $T_{2,\text{avg}}^* = 1.9$ μs obtained from this region is significantly lower that that from (a).

For the ^{209}Bi fluence of 1×10^{13} ions/cm^2, we measure the dephasing time T_2^* of 61 single NV centers with a small magnetic field $B = 10$ G applied along the (100)-direction of the sample [see Fig. 6.3(a)]. This choice of magnetic field allows for unbiased measurements of all four NV orientations. We obtain an average value of the dephasing time $T_{2,\mathrm{avg}}^* = 2.7$ μs. We also note that this is an overestimate of T_2^* as we have excluded the sites with no ODMR response.

For the ^{209}Bi fluence of 5×10^{13} ions/cm^2 under the same magnetic field condition, we find that the signal contrast of the Ramsey fringes is insufficient for obtaining reliable fits for T_2^*. To improve the signal contrast, we realigned the magnetic field along the (111)-direction of the sample and increased the magnetic field strength to $B_z = 200$ G. At this moderate magnetic field strength, the spin bath can exhibit an appreciable polarization via optical pumping [74]. The nuclear polarization, along with the absence of the off-axis magnetic field, typically results in a better signal contrast and longer T_2^*. Then, we measure the T_2^* of 45 single NV centers whose axes are aligned with the magnetic field [see Fig. 6.3(b)]. However, we obtain an average value $T_{2,\mathrm{avg}}^* = 1.9$ μs, a value lower than that of the region with ^{209}Bi fluence of 1×10^{13} ions/cm^2, indicating that the environment around the NV centers is disturbed by the Bi implantation.

6.5 Higher-Order Characterization: Dynamical Decoupling

To overcome the limitation of the short dephasing time T_2^* of the co-implanted sites and improve the sensitivity for detecting dynamics associated with bismuth nuclear spins, we utilize dynamical decoupling techniques for mitigating the quasi-static noise and extending the coherence time [14,19,92]. The extended coherence times obtained by dynamical decoupling also provides an enhancement in the ac sensitivity of the NV center [22].

In general, the dynamical decoupling pulse sequence is an extension of the Hahn echo sequence [13], where a π-pulse is applied during the free precession of the spin. This technique can mitigate the decoherence from sources whose correlation time is longer than that of the free precession interval τ. As an effort to extend the coherence time beyond the Hahn echo method, Carr and Purcell introduced a concatenation of multiple π-pulses, separated by regular intervals τ, also known as CP sequence [16]. However, as the number of pulses increases, the error from each pulse can accumulate and contribute additionally to the decoherence. To overcome this limitation, Meiboom and Gill proposed a method to reduce the effect from pulse errors by modifying the CP sequence such that the axes of π-pulses are perpendicular to the state preparation $\pi/2$-pulse, resulting in the CPMG sequence [17].

In the particular case of nuclear spin sensing, where most of the time the electronic spin is in an arbitrary state on the Bloch sphere, we utilize a variation of the CPMG sequence that is symmetric under time reversal. This pulse sequence, also known as the XY8k sequence, is especially robust against pulse errors and arbitrary state preparations [15,19]. The pulse sequence is depicted in Fig. 6.4. First, the NV center electronic spin is optically polarized with a 532-nm laser pulse. Then, a $(\pi/2)_{+x}$ pulse is applied to create a superposition between the $m_S = 0$ and the $m_S = -1$ states. During the free precession time that immediately follows, eight π-pulses are applied at regular intervals with their axes alternating in a time-reversal symmetric manner. Each π-pulse is separated from one another by the time duration τ, effectively performing eight spin echoes on the NV center electronic spin. This sequence is repeated k times to extend the total free precession time in the case of small τ. Finally, another phase-controlled $(\pi/2)_{-x}$ or $(\pi/2)_{+x}$ pulse is applied to to rotate the spin projection back to measurement basis z or $-z$, respectively. The results are then subtracted to obtain the contrast ΔPL, while canceling out PL drifts in the system. To achieve phase-controlled pulses in our experiments, we use a fast arbitrary waveform generator (Tektronix AWG7122B) operating in interleaved mode at 24 GS/s to generate the full MW signal. The duration of the π-pulses was kept around $20-40$ ns to drive both the $m_I = -\frac{1}{2}$ and $m_I = +\frac{1}{2}$ states of the ^{15}N nuclear spin that are separated by the hyperfine coupling $A_{\parallel} = 3.03$ MHz.

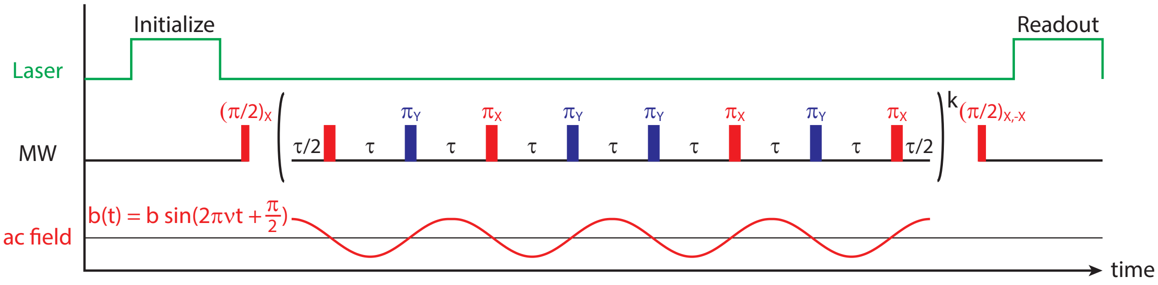

Figure 6.4: Schematic of the XY8k dynamical decoupling sequence for sensing ac magnetic fields. After optical initialization, the NV electronic spin is prepared in a superposition of the $m_S = 0$ and $m_S = -1$ states with a $(\pi/2)_{+x}$ pulse. Then, π-pulses are applied periodically for $8 \times k$ times to dynamically decouple the electronic spin from the environment. The phase of the π-pulses is alternated in a time-reversal symmetric manner to compensate for small pulse errors. Finally, a $(\pi/2)_{-x}$ or $(\pi/2)_{+x}$ pulse is applied to rotate the spin back to the measurement basis, z or $-z$, respectively. The results are then subtracted to obtain the contrast ΔPL. This pulse sequence is ineffective against the ac magnetic field $b(t)$ whose frequency is half of that of the π-pulses, as the π-pulse spin flips result in a constructive interference of the phase accumulated. We utilize this mechanism for the frequency-selective ac magnetic field sensing.

While dynamical decoupling is effective against decoherence sources with a long correlation time, it is ineffective against ac magnetic fields whose frequency matches the resonance condition of the π-pulse intervals. An example of a fundamental resonance condition for an XY8k dynamical decoupling sequence is shown in Fig. 6.4, where the frequency of the ac magnetic field noise (ν) is half that of the π-pulse train. In this case, each spin flip introduced by the π-pulse results in constructive interference of the phase accumulation. In general, the phase accumulation from an external ac magnetic field $b(t) = b\sin(2\pi\nu t + \varphi_0)$ is given by [20–22]:

$$\begin{aligned}\frac{\delta\phi}{2\pi} &= 8k \times g_e\mu_B \left[\int_0^{\tau/2} b(t)dt - \int_{\tau/2}^{\tau} b(t)dt\right] \\ &= g_e\mu_B \cdot b \cdot 8k\tau \cdot \frac{\sin^2(2\pi\nu\tau/4)\cos(2\pi\nu\tau/2 + \varphi_0)}{2\pi\nu\tau/4}. \end{aligned} \tag{6.1}$$

This phase accumulation is maximized when $\varphi_0 = \frac{\pi}{2}$ and $2\pi\nu\tau = \pi$, where we obtain $\delta\phi_{\max}/2\pi = 4g_e\mu_B \cdot b \cdot 8k\tau$. However, in general, the source of $b(t)$ will have a random phase with respect to the experimental sequence, resulting in the experimental value being the root mean square (rms) of the signal:

$$\frac{\delta\phi_{\mathrm{rms}}}{2\pi} = 2\sqrt{2}g_e\mu_B \cdot b \cdot 8k\tau. \tag{6.2}$$

As a consequence of the constructive interference when $2\nu\tau = 1$, the XY8k dynamical decoupling sequence is particularly sensitive to the ac magnetic field noise frequency $\nu = 1/2\tau$ [22]. Therefore, by varying the time interval τ between the π-pulses, we can probe the frequency information of the spin bath experienced by the NV center. In particular, when the ac signal frequency is off resonance ($\nu \neq \frac{1}{2\tau}$), we can perform an explicit integral to obtain the response in the frequency domain, given by the filter function [92]:

$$Y_{N=8k}(\nu,\tau) = \frac{1 - \sec(\pi\nu\tau)}{2\pi\nu\tau}\sin(2\pi N\nu\tau), \qquad Y_{\max} = \frac{2N}{\pi}. \tag{6.3}$$

The normalized filter function $Y_N/Y_{N,\max}$ [see Fig. 6.5] represents the contribution from each frequency of the ac magnetic field to the total phase accumulated for an XY8k dynamical decoupling sequence with pulse interval τ. This normalized contribution is given relative to the maximum value at the fundamental resonance, where $\nu = 1/2\tau$ [Eq. 6.2]. In addition to the diminishing contribution away from the fundamental resonance, the filter function also shows odd-number l-th harmonics,

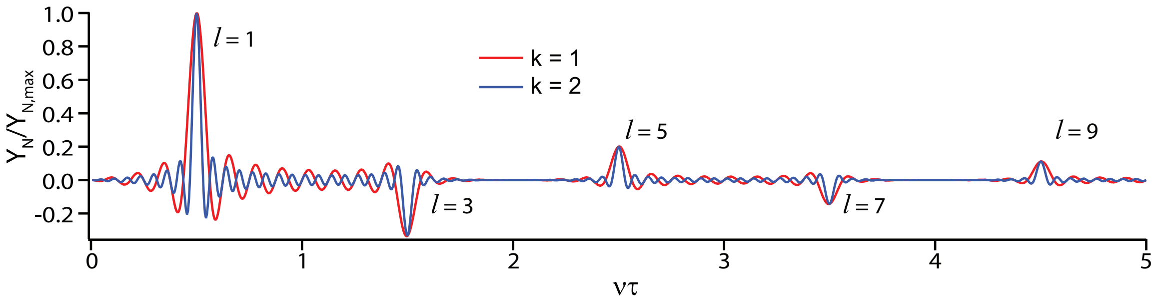

Figure 6.5: Normalized filter functions of an XY8k pulse sequence: The XY8k decoupling sequence with time interval τ between the π-pulses is most sensitive to the ac signal frequency $\nu = 1/2\tau$. In addition to this fundamental frequency, the filter function also shows odd-number l-th harmonics. These harmonics allow for frequencies $\nu = l/2\tau$ to contribute to the phase accumulation for a given time τ.

where the ac magnetic field frequencies $\nu = l/2\tau$ can also contribute to the phase accumulation at a given time τ. Conversely, a single ac magnetic field frequency ν can also produce signals at $\tau = l/2\tau$, imitating the fundamental resonance from multiple ac magnetic fields with frequencies $\nu_l = \nu/l$. The amplitude of these harmonics, however, are suppressed for higher-order harmonics.

6.6 Dynamical Decoupling Results

To characterize the nuclear spin bath of the NV centers, we sample the sites from the arrays with bismuth co-implantations and perform XY8k sensing scheme using the superposition state between $m_S = 0$ and $m_S = -1$. The pulse sequence is described in Section 6.5. From the PL contrast (ΔPL) obtained, we can identify the time τ during which the coherence of the NV is not preserved from the XY8k dynamical decoupling as a consequence of the nuclear spin bath being on resonance with the dynamical decoupling sequence. To reliably confirm a nuclear spin specie via the gyromagnetic ratio, we also considered the harmonics of the signal that can arise from the dynamical decoupling sequence. Normal harmonics from the XY8k filter function are described in Section 6.5. In addition to these normal harmonics, spurious harmonics may also occur as the finite duration of the π-pulses causes the rotation axis to precess during the pulse [93]. The effects of the finite-duration π-pulse, however, were not observed in our experiments for $\tau > 100$ ns.

We probe the frequencies of the nuclear spin bath surrounding the NV centers by performing XY8k dynamical decoupling sequence at multiple values of the magnetic field B_z along the NV center. At a particular value B_z, the nuclear spin (gyromagnetic ratio $g_N\mu_N$) undergoes a Larmor precession with frequency $\nu_L = g_N\mu_N B_z$. By varying B_z and observing the evolution of the signal, we can reliably map out each of the different ΔPL signals that correspond to a specific nuclear gyromagnetic ratio, up to a factor l of the harmonics.

Figure 6.6 shows a sample of the spectroscopy results from applying a XY8k, $k = 8$ sensing scheme on a NV co-implanted with ^{209}Bi fluence of 1×10^{13} ions/cm^2. From the data, we can identify the two species, ^{13}C and ^{15}N, from the spectra. Their Larmor precession frequencies are labeled with red dashed lines and the order l of the harmonics is indicated in parentheses by (ν/l). The precession frequency from the ^{13}C nuclear spins follows a simple form $f_L = 1/2\tau = g_N\mu_N B_z$, with $g_N\mu_N = 1.07$ kHz/G. However, the precession frequency of the ^{15}N spin ($g_N\mu_N = 0.432$ kHz/G) is also dependent on the hyperfine coupling $A_{zz} = 3.03$ MHz, and is given by $\nu_L = A_{zz} + g_N\mu_N B_z$. In addition to the two known species, we also observe two additional ΔPL signals corresponding to precession frequencies $\nu_1 = 385$ kHz and $\nu_2 = 510$ kHz in our spin noise, indicated by green dashed lines in Fig. 6.6. Unlike the ^{15}N and ^{13}C signals, these signals are not reproducible in other NV centers and do not change with B_z in this range of $B_z = 200 - 900$ G. While the origin of these two frequencies is still unclear, we have not observed any signal with the expected Larmor frequencies of the ^{209}Bi nuclear spin [blue dashed line in Fig. 6.6], even with the repetitions up to $k = 32$ (256 π-pulses total) and the total detection time up to $8k\tau = 512$ μs.

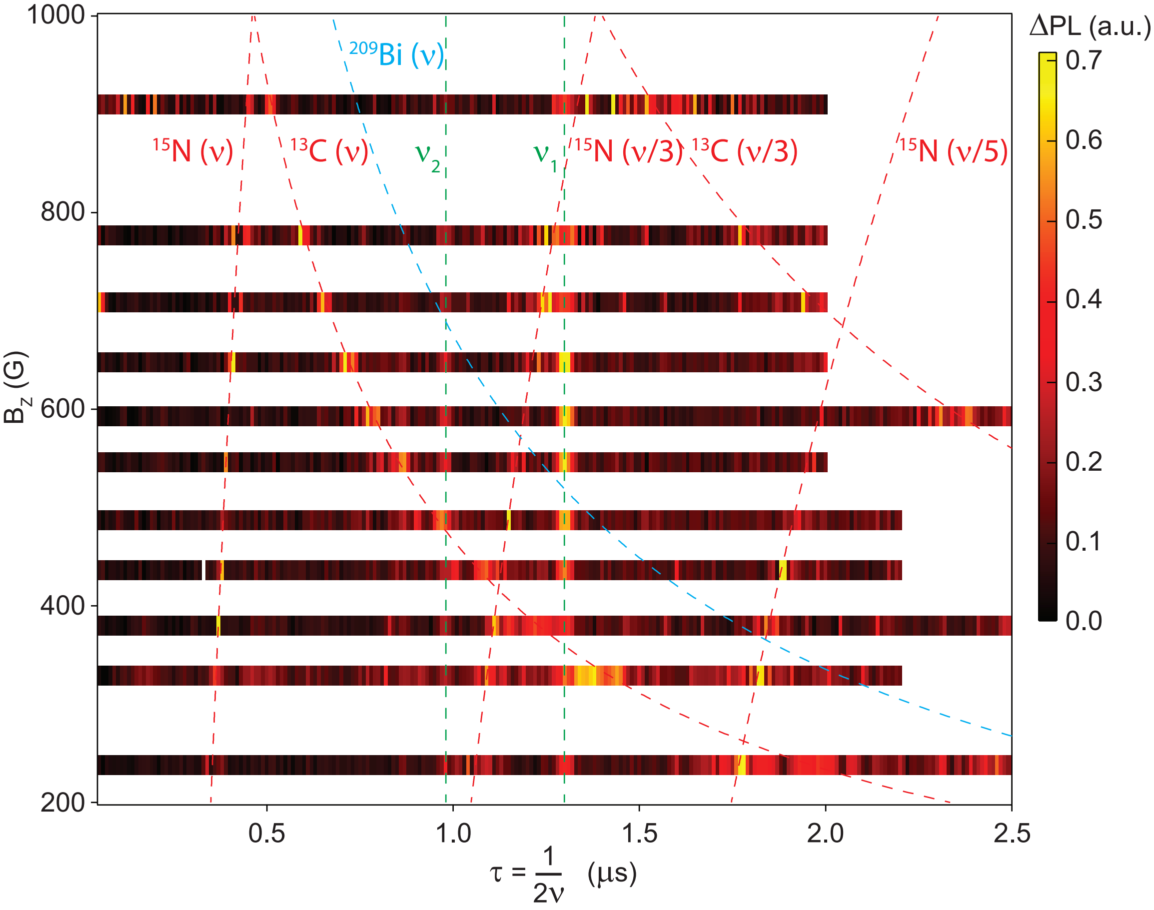

Figure 6.6: XY8k, $k = 8$ spectroscopy data. The data shows the PL contrast, ΔPL, obtained from dynamical decoupling as a function of π-pulse interval τ and external magnetic field B_z. Large values of ΔPL indicate areas where the coherence of the NV is not preserved by the XY8k dynamical decoupling scheme as τ satisfies the resonance condition $\tau = l/2\nu$, where l is the order of the harmonics. The red dashed lines indicate the expected signals from the known species of the nuclear spins, ^{13}C and ^{15}N. The l-th harmonics are indicated by (ν/l). The blue dashed line indicate the first harmonic signals we expect from ^{209}Bi Larmor precession. The green dashed lines indicate the two additional signals that do not change with the magnetic field in this regime.

6.7 Summary

We have studied co-implantations of ^{209}Bi and ^{15}N into a high-purity diamond surface for the purpose of coupling the nuclear spin $I = 9/2$ of the ^{209}Bi ions with the NV center electronic spin. We observe a significant reduction of NV center conversion yield and the NV coherence as a result of the bismuth co-implantations. However, we do not see any evidence of strong coupling between the NV electronic spin and bismuth nuclear spins via Ramsey experiments and pulsed-ODMR spectroscopy. A dynamical decoupling technique has been employed to improve the sensitivity of our measurements, where we can observe Larmor precession of the ^{13}C and ^{15}N nuclear spins. We also observe anomalous ac magnetic field signals whose frequencies are independent of the magnetic field strength between $200 - 900$ G. However, there is no direct evidence of the ^{209}Bi Larmor precession in the proximity of a NV center. In principle, the experiments could be extended to an ensemble scale, where more bismuth ions are implanted into the diamond and more NV centers are available for efficient detection. It is also possible to fine tune the ^{209}Bi implantation parameters such that the ^{209}Bi distribution overlaps with smaller region of the ^{15}N distribution after graphitization damage. The smaller overlap region will result in a higher probability of obtaining strong coupling between a NV center and ^{209}Bi nuclear spins.

Chapter 7

Conclusions and Outlook

In this dissertation, we have demonstrated room temperature experiments on the NV center in diamond. We started from the basic creation of NV centers in high-purity diamond via ion implantation. We showed methods for efficient characterization of NV centers using a confocal microscope. From the PL statistics, we can establish criteria for determining the number of NV centers within a confocal volume. This method is significantly more efficient than photon correlation measurements that require long integration times. We also showed tunability of the implanted NV center population by means of fine adjustments to the aperture mask dimensions.

Following the discussion of the creation of NV centers, we demonstrated quantum control of the NV center electronic and nuclear spins using MW and RF manipulations. By utilizing a single NV center and its hyperfine coupling to the intrinsic ^{14}N nuclear spin, we showed that by driving off-resonant electron Rabi oscillations, the nuclear spin can exhibit spin-dependent phase shifts. We used this mechanism to develop a fast phase gate on the intrinsic ^{14}N nuclear spin, where we achieved a sub-microsecond π-phase gate on the nuclear spin. This achievement is a major improvement of the control speed over conventional NMR pulses operating on the nuclear spin.

We also showed enhancements to the effective gyromagnetic ratio of the nuclear spin that is coupled to a NV center. This enhancement is a result of the ground state hyperfine coupling between the NV electronic and nuclear spins. We carefully studied the enhancement near the ground state anti-crossing, where the enhancement is maximized. We achieved more than a factor of 2000 enhancement of the effective nuclear gyromagnetic ratio over the bare nuclear gyromagnetic ratio. This result is also applicable to other coupled electron-nuclear spin systems, such as phosphorous donors in silicon and rare earth dopants in crystalline hosts, allowing for fast quantum control without requiring high RF power.

Finally, we discussed preliminary experiments aimed towards coupling a single NV center to higher nuclear spin systems. We showed results from co-implantation of nitrogen and bismuth into a high-purity diamond substrate. However, the co-implantation of a heavy atom such as bismuth resulted in a significant lattice damage and a reduction of the NV coherence time. We mitigated the latter effect by utilizing dynamical decoupling techniques and showed sensitivity capable of detecting ^{15}N and ^{13}C Larmor precessions. However, we did not observe any evidence of coupling to bismuth nuclear spins. Therefore, we concluded with the discussions on how to achieve stronger couplings by moving towards ensemble-scale couplings and fine tuning the implantation parameters.

All the experiments presented in this dissertation show the versatility of the NV center system. In addition to being good quantum information processing units, the NV centers can also serve as robust quantum sensors for magnetometry. However, at the current state of technology, these defects cannot be reproducibly created on an atomic scale. The ability to engineer these defects in an atomic scale would result in a tremendous improvement in terms of the scalability of the NV as a qubit and in terms of the sensitivity as a magnetometer.

Appendix A

Experimental Setup

The full schematic of the experimental setup is shown in Fig. A.1. We use a custom-built laser scanning confocal microscope with a 532-nm laser source (Coherent Sapphire SF532-100). The laser is directed through an acousto-optic modulator (AOM, Gooch & Housego 15210) for switching the laser on and off at high speed (rise time $\sim$ 10 ns) before coupling through a single-mode fiber (Thorlabs). The laser output is directed into the confocal microscope by means of a dichroic mirror, then directed towards scanning galvo mirrors (Thorlabs GVS002) for rastering over the sample. The diamond sample is mounted on a piezo stage (Thorlabs NF15AP25) in a room-temperature enclosure with a 50× objective (Olympus MPLAPON50X, NA=0.95) for high collection efficiency. We use the piezo stage for fine-focusing of the confocal image. Fluorescence is then collected via the same objective lens and is separated from the excitation lasers using a longpass dichroic filter (Thorlabs DMLP567) for 532-nm filering. The remaining excitation lasers are then filtered out with a 532-nm notch filter (Thorlabs NF533-17), a 600-nm longpass filter (Thorlabs FEL0600), and two 635-nm longpass filters (Semrock BLP-01-635R-25) before being focused onto a single-mode fiber (Thorlabs SM600) acting as a confocal pinhole. Single photon detection is achieved using avalanche photodiodes (PerkinElmer SPCM-AQRH-14-

FC, dark counts 100 counts/s). The signal from the photon detector is routed to a multi-function DAQ (NI PCIe-6363) for photon counting and to a time-correlated single photon counting module (Picoharp 300) for lifetime and photon correlation measurements.

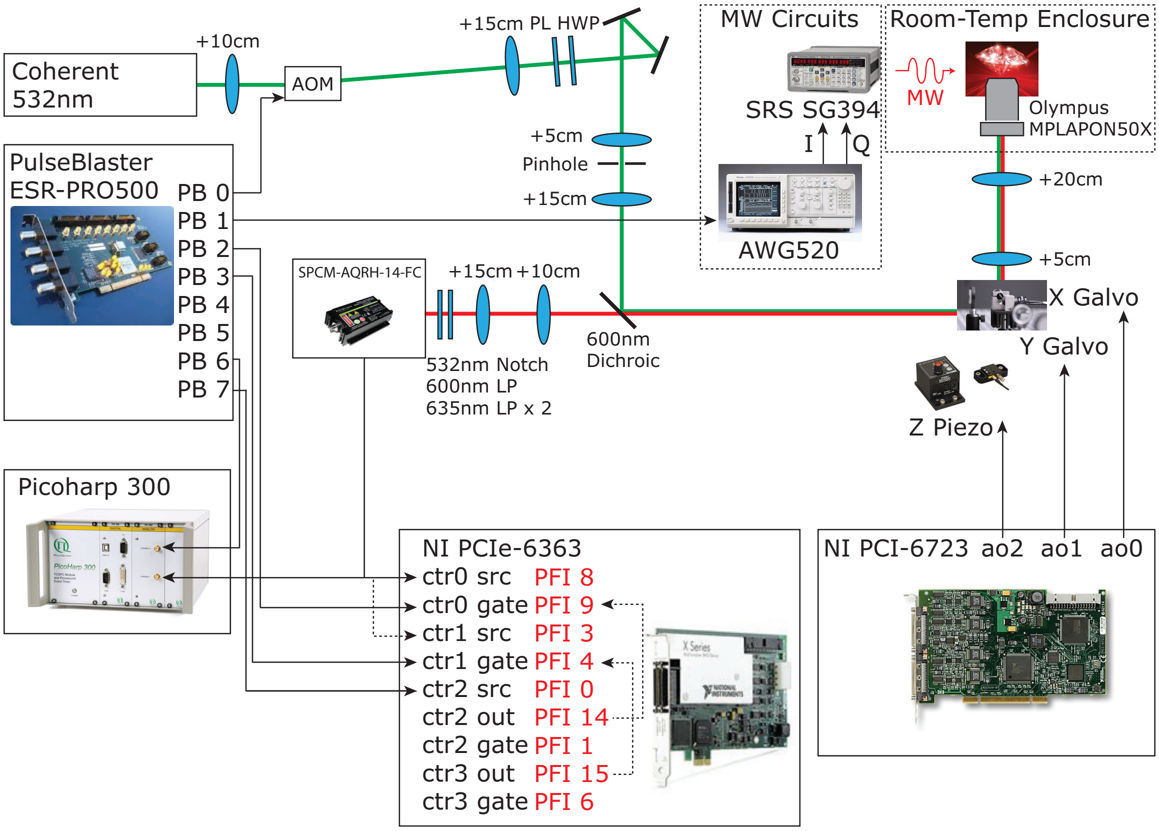

Figure A.1: Schematic of the experimental setup. The optical setup consists of a confocal microscope with a 532-nm laser excitation and a single photon detector. Confocal scanning of the sample is achieved by rastering the XY galvo mirrors and adjusting the Z piezo via the analog outputs of a NI PCI-6723. The sample and the objective lens are placed inside an enclosure to minimize the effects from room temperature fluctuations. Experimental sequencing is achieved with a digital delay generator (PulseBlaster) operating at a clock speed of 500 MHz. Photon counting is achieved with either a Picoharp 300 or the digital counters on a NI PCIe-6363. Gating of the digital counters is achieved either via the PulseBlaster signals, or via an internal clock of the PCIe-6363 that is internally routed through the software.

Confocal scanning is performed by synchronizing the analog output signals from an analog output generator (NI PCI-6723) to the galvo mirrors such that they raster over the sample area. The photoluminescence (PL) is measured by counting the photons within the scanning interval.

For pulsed experiment sequencing, a high-speed digital delay generator (PulseBlaster ESR-PRO500), operating at 500 MHz, is used to gate the acousto-optic modulators and the counters on the multi-function DAQ. The same pulse generator is also used for triggering the MW circuits.

Quantum control of NV center spins is achieved by sending MW and RF signals to the sample. The MW circuit setup varies from experiment to experiment and therefore is specified in each chapter of this dissertation. Figure A.1 shows an example of the MW circuit for vector control of the MW pulses. An arbitrary waveform generator (Tektronix AWG520), triggered by the PulseBlaster, is used to drive the external IQ modulation input of the MW generator (SRS SG394) for phase control of the MW pulses.

Appendix B

Nuclear Polarization at the ESLAC

In Chapter 4, we work with the ^{14}N nuclear spin that is intrinsic to the NV center. To initialize the spin, we utilize the ESLAC for dynamic nuclear polarization, a process that has been studied extensively on implanted ^{15}N [29, 74]. The excited state Hamiltonian of the ^{14}NV center is given by:

$$H = ES_z^2 + g_e\mu_B\vec{B}\cdot\vec{S} + \frac{1}{2}A_\perp(S_+I_- + S_-I_+) + A_\parallel S_zI_z + QI_z^2 - g_N\mu_N\vec{B}\cdot\vec{I}. \quad \text{(B.1)}$$

The form is similar to that of the ground state, with the exception of the zero-field splitting $E \sim 1.42$ GHz and a much stronger hyperfine coupling $A_\perp, A_\parallel \sim 40$ MHz [29, 30, 75].

The energy level diagram near the ESLAC ($B_{\text{ESLAC}} \approx 510$ G) is depicted in Fig. B.1, where couplings between two states of the same total spin projection are the result of the axial hyperfine coupling. It is precisely this coupling, along with the non-radiative intersystem crossing mechanism for electronic spin polarization, that allows for dynamic nuclear polarization via optical pumping. The result is a large nuclear spin polarization in the state with the maximum spin projection along the NV axis ($m_I = +1$) [see Fig. B.2(a)].

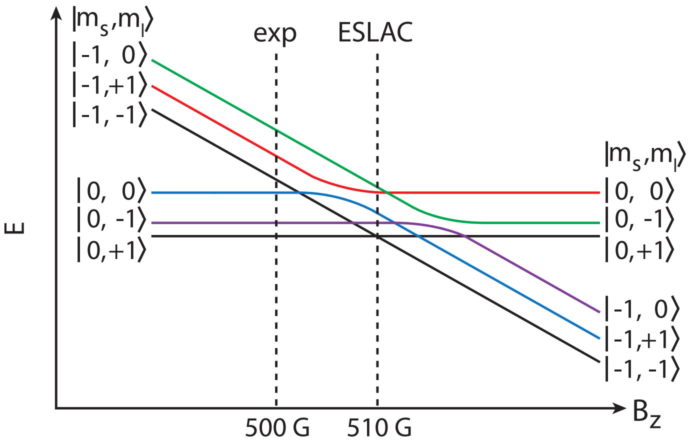

Figure B.1: Excited state energy levels of a NV center as a function of the magnetic field B_z along the NV axis near the ESLAC.

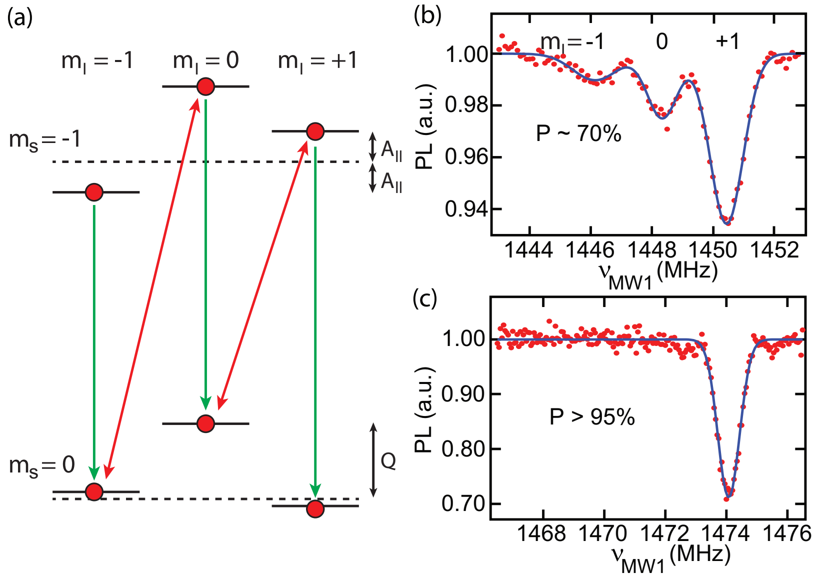

Figure B.2: (a) Energy level diagram with $B_z = 500$ G, showing the electronic and nuclear spin polarization process. Red arrows indicate couplings from the axial hyperfine interaction. Green arrows indicate optical pumping processes that are driven by the 532 nm laser. Under the appropriate conditions, the system is polarized to $|0, +1\rangle$. (b) PL as a function of selective MW1 π-pulse frequency showing electronic spin transitions near the ESLAC. Three ^{14}N hyperfine transitions are visible due to imperfect nuclear polarization. (c) Careful alignment of the magnetic field increases the ^{14}N nuclear spin polarization to $> 95\%$.

To measure the nuclear spin polarization, we perform ODMR spectroscopy by repeating the initialization pulse sequence and sweeping MW1 frequency ν_{MW1}. Initial data with the magnetic field aligned to within $\sim 1^\circ$ of the NV axis [Fig. B.2(b)] contains three Gaussian dips corresponding to the transitions associated with the three nuclear spin states of ^{14}N. The visibility of the three transitions indicates imperfect nuclear polarization due to spin mixing near the ESLAC. The peak separation was measured to be ~ 2.16 MHz, consistent with other experimental results [12, 30, 75].

The degree of nuclear spin polarization is determined by fitting the data to three Gaussian peaks. All peaks are constrained to have the same width (FWHM = 1.13 MHz) and their heights are fitted with one parameter, the effective temperature T. The peak amplitudes A_{m_I} are defined by $A_{m_I} = A\exp(-E_{m_I}/k_BT)$, where k_B is Boltzmann's constant. The energies E_{m_I} are defined as:

$$E_{+1}/h = 0, \tag{B.2}$$

$$E_0/h = |E_{|0,+1\rangle} - E_{|0,0\rangle}|/h = |Q - g_N\mu_N B_z| = 5.25 \text{ MHz}, \tag{B.3}$$

$$E_{-1}/h = |E_{|0,+1\rangle} - E_{|0,0\rangle}|/h + |E_{|0,0\rangle} - E_{|0,-1\rangle}|/h = 2|Q| = 9.92 \text{ MHz}. \tag{B.4}$$

The nuclear spin polarization is given by:

$$P = \frac{A_{+1}}{A_{-1} + A_0 + A_{+1}}. \tag{B.5}$$

From the initial coarse alignment of the magnetic field [Fig. B.2(b)], we obtained $P = 0.71$. After careful magnetic field alignment, the ODMR contrast drastically improves and we achieve $m_I = +1$ nuclear spin polarization $P = 0.96$ [Fig. B.2(c)].

Appendix C

Dark State Population and Readout at the ESLAC

To simulate the readout process in Chapter 4, we use the rate equation model and consider only the relevant states $|m_S, m_I\rangle = \{|0,0\rangle, |0,+1\rangle, |-1,0\rangle, |-1,+1\rangle\}$. The model [see Fig. C.1(a)] consists of the following transitions (GS: Ground State, ES: Excited State):

- γ: Excitation from GS to ES.
- Γ_{ES}: Decay from $m_S = 0$ ES directly to GS.
- Γ_{ES}: Decay from $m_S = -1$ ES with probability p to shelving state A_1, probability $1-p$ to GS.
- Γ_{A1}: Decay from A_1 to $m_S = 0$ GS.
- A_{ES}: Hyperfine mixing of $|0,0\rangle$ and $|-1,+1\rangle$ ES.

The values used are $\gamma = 0.3$ GHz, $\Gamma_{\mathrm{ES}} = 1/T_{\mathrm{ES}} = (13\ \mathrm{ns})^{-1}$, $\Gamma_{\mathrm{A1}} = 1/T_{\mathrm{A1}} = (300\ \mathrm{ns})^{-1}$, $A_{\mathrm{ES}} = 40$ MHz, $p = 0.3$. Photoluminescence is then given by the rate of the radiative decay from the ES to the GS.

$$\begin{aligned}\mathrm{PL} = &\Gamma_{\mathrm{ES}} P_{|0,0\rangle} + \Gamma_{\mathrm{ES}} P_{|0,+1\rangle} \\ &+ (1-p)\Gamma_{\mathrm{ES}} P_{|-1,0\rangle} + (1-p)\Gamma_{\mathrm{ES}} P_{|-1,+1\rangle}.\end{aligned} \tag{C.1}$$

Figure C.1(b) shows that the state $|0,0\rangle$ does indeed contribute to a "dark" readout, comparable even to that of the $|-1,0\rangle$ state. The decrease in the fluorescence is due to the population being trapped in the long-lived shelving state.

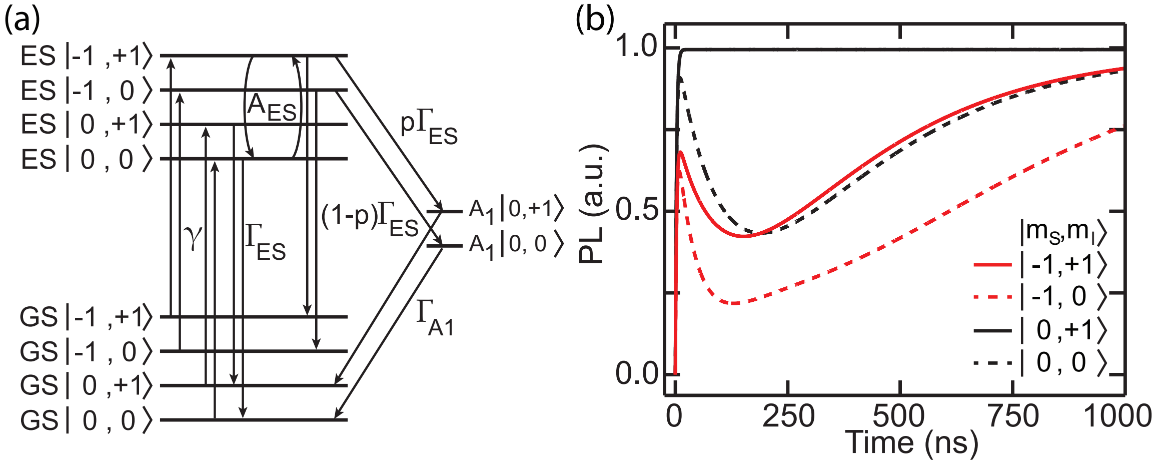

Figure C.1: (a) States and their coupling used to model the readout process. (b) Simulated PL time trace of a NV center prepared in different states.

Appendix D

Fabrication Recipes

D.1 Photolithography Recipe for Etching Alignment Marks

This is a recipe for making a Cr/Au metal mask on bulk diamond to protect the surface and create permanent markers via reactive ion etching through the openings of the mask. We start by making a mask for etching using photolithography with the following recipes:

Photolithography Mask:

1. Sonicate the diamond sample in acetone for 5 minutes and in isopropanol for 5 minutes, using glass beakers. Then, blow dry.
2. Prebake at 190 °C for 5 minutes.
3. Spin coat with lor5a photoresist in a two step process.
    - Step 1: 500 rpm, 500 rpm/s ramp, 5 s.
    - Step 2: 4,500 rpm, 4,500 rpm/s ramp, 60 s.
4. Bake at 190 °C for 5 minutes.

5. Spin coat with S1818 photoresist in a two step process.
   - Step 1: 500 rpm, 500 rpm/s ramp, 5 s.
   - Step 2: 4,500 rpm, 4,500 rpm/s ramp, 60 s.
6. Bake at 115 °C for 2 minutes.
7. Expose with the MJB4 for 3 s using soft contact, reflected light.
8. Develop with MF319 for 45 s, followed by a rinse in DI water. Agitate well during these processes.
9. Bake at 125 °C for 5 minutes.
10. Develop with MF319 for 60 s, followed by a rinse in DI water.
11. Optically inspect the pattern.

Metalization:

1. UV Ozone clean at 200 °C for 2 minutes.
2. Using the Sharon thermal evaporator, evaporate 10 nm of Cr at a rate of 0.35 Å/s. Then evaporate 150 nm of Au at a rate of 1.5 Å/s.
3. Liftoff using Nanoremover PG that is heated to 80 °C. Typical liftoffs are achieved in $\sim$ 30 minutes.
4. Transfer the sample into a petri dish containing acetone and spray the sample with more acetone from a squeeze bottle.
5. Transfer the sample into a petri dish containing isopropanol and optically inspect the sample. If there are remaining residues, sonicate for 5 s in acetone and isopropanol, using plastic beakers, to remove the residues.
6. Optically inspect the sample again before proceeding to etching.

Reactive Ion Eching:

1. Prepare the STS Reactive Ion Etcher chamber by etching a clean silicon wafer using `o2diamond` recipe (5 minutes, O_2 30 SCCM, 100 W Bias Power, 700 W ICP Power, 10 mTorr).

2. Mount the sample onto a fused-silica wafer with crystal bond.

3. Run Tepla `strip10min` (no Faraday cage, RF 500 W, O_2 150 sccm, 500 mTorr, Ignition level 1000 mV).

4. Load the fused-silica wafer with the sample into the chamber and perform a real etch using `o2diamond` recipe (5 minutes, O_2 30 SCCM, 100 W Bias Power, 700 W ICP Power, 10 mTorr).

D.2 Electron Beam Lithography for the Ion Implantation Mask

Implantations described in Chapter 3 of this dissertation were done using PMMA 950K A4 as a mask, as it provides the highest resolution. Later, we found that continuous exposure of the PMMA to the electron beam during aperture size measurements can cause the apertures to swell or collapse. Therefore, implantations in Chapter 6 were done using ZEP520A as an implantation mask. ZEP520A is more robust against etching and electron beam imaging. Aperture sizes down to 40 nm can still be achieved with the resolution provided by ZEP520A.

D.2.1 PMMA 950K A4 Implantation Mask

1. Sonicate the diamond sample in acetone for 5 minutes and in isopropanol for 5 minutes, using glass beakers. Then, blow dry.
2. Run Tepla `strip10min` (no Faraday cage, RF 500 W, O_2 150 sccm, 500 mTorr, Ignition level 1000 mV) to remove any remaining organic residues.
3. Spin on PMMA 950K A4 in a single step: 3,300 rpm, 10,000 rpm/s ramp, 45 s.
4. Bake at 170 °C for 15 minutes.
5. Evaporate 10 nm Al with the AJA electron beam evaporator at a rate of 1.5 Å/s.
6. Expose the pattern with the Elionix, 125 kV, 120 μm aperture, 500 pA, dose $\sim 1600 - 2000$ μC/cm^2. Focusing is done using the height sensor.
7. Develop with MF-319 for 60 s to remove all of the aluminum discharge layer. (Aluminum is typically removed in $\sim$ 10 s.)

8. Develop with MIBK:IPA 1:3 for 60 s, followed by a rinse in isopropanol for 20 s. Then, blow dry.

D.2.2 ZEP520A Implantation Mask

1. Sonicate the diamond sample in acetone for 5 minutes and in isopropanol for 5 minutes, using glass beakers. Then, blow dry.
2. Run Tepla `strip10min` (no Faraday cage, RF 500 W, O_2 150 sccm, 500 mTorr, Ignition level 1000 mV) to remove any remaining organic residues.
3. Spin on ZEP520A in a single step: 6,000 rpm, 10,000 rpm/s ramp, 60 s. (ZEP520A dissolves in 1165 remover, PG remover, i.e. n-methyl-2-pyrrolidone (NMP), after exposed to UV light.)
4. Bake at 180 °C for 3 minutes.
5. Evaporate 10 nm Al with the AJA electron beam evaporator at a rate of 1.5 Å/s.
6. Expose the pattern with the Elionix, 125 kV, 120 μm aperture, 100 pA, dose $\sim 240 - 320$ μC/cm^2. Focusing is done using the height sensor.
7. Develop with MF-319 for 60 s to remove all of the aluminum discharge layer. (Aluminum is typically removed in $\sim$ 10 s.)
8. Develop with ZED-N50 (n-amyl acetate) for 60 s, followed by a rinse in isopropanol for 20 s. Then, blow dry.
9. Post-bake at 95 °C for 2 minutes.

D.3 Microwave Stripline Fabrication

Microwave striplines were fabricated using a bilayer PMMA/MMA resist. The stripline consists of 0.6 nm of titanium for adhesion, followed by 200 nm of gold to achieve low resistance.

1. From a clean sample (no metal), sonicate the diamond sample in acetone for 5 minutes and in isopropanol for 5 minutes, using glass beakers. Then, blow dry.
2. Run Tepla `strip10min` (no Faraday cage, RF 500 W, O_2 150 sccm, 500 mTorr, Ignition level 1000 mV) to remove any remaining organic residues.
3. Spin on PMMA/MMA EL11 in a single step: 4,000 rpm, 4,000 rpm/s ramp, 60 s.
4. Bake at 120 °C for 5 minutes.
5. Spin on PMMA 950K A4 in a single step: 4,000 rpm, 4,000 rpm/s ramp, 60 s.
6. Bake at 170 °C for 15 minutes.
7. Evaporate 25 nm Al with the AJA electron beam evaporator at a rate of 5 Å/s. (With the delay in shutter closing, stopping at 25 nm gives $\sim$ 29 nm when the shutter is fully closed.)
8. Expose the pattern with the Elionix, 125 kV, 120 μm aperture, 500 pA, dose $\sim 1600 - 2000$ μC/cm^2. Focusing is done using the height sensor.
9. Develop with MF-319 for 5 minutes to remove all of the aluminum discharge layer. (Aluminum is typically removed in $\sim$ 2 minutes.)
10. Develop with MIBK:IPA 1:3 for 60 s, followed by a rinse in isopropanol for 20 s. Then, blow dry.

11. Run Tepla `descum10min` (with Faraday cage, RF 200 W, O_2 150 sccm, 500 mTorr, Ignition level 1000 mV).
12. Using the Sharon thermal evaporator, evaporate 0.6 nm of Ti at a rate of 0.15 Å/s. Then, evaporate 200 nm of Au at a rate of 1.5 Å/s.
13. Lift off in acetone for at least 3-4 hours. Rinse in isopropanol.
14. UV Ozone clean at 200 °C for 5 minutes.

Bibliography

[1] F. Jelezko, I. Popa, A. Gruber, C. Tietz, J. Wrachtrup, A. Nizovtsev, and S. Kilin, *Appl. Phys. Lett.* **81**, 2160 (2002).

[2] F. Jelezko, T. Gaebel, I. Popa, A. Gruber, and J. Wrachtrup, *Phys. Rev. Lett.* **92**, 076401 (2004).

[3] F. Jelezko, T. Gaebel, I. Popa, M. Domhan, A. Gruber, and J. Wrachtrup, *Phys. Rev. Lett.* **93**, 130501 (2004).

[4] G. Balasubramanian *et al.*, *Nature Materials* **8**, 383 (2009).

[5] E. Togan *et al.*, *Nature* **466**, 730 (2010).

[6] H. Bernien *et al.*, *Nature* **497**, 86 (2013).

[7] B. Hensen *et al.*, *Nature* **526**, 682 (2015).

[8] F. Dolde, I. Jakobi, B. Naydenov, N. Zhao, S. Pezzagna, C. Trautmann, J. Meijer, P. Neumann, F. Jelezko, and J. Wrachtrup, *Nature Phys.* **9**, 139 (2013).

[9] P. Neumann, J. Beck, M. Steiner, F. Rempp, H. Fedder, P. R. Hemmer, J. Wrachtrup, and F. Jelezko, *Science* **329**, 542 (2010).

[10] A. Dréau, P. Spinicelli, J. R. Maze, J.-F. Roch, and V. Jacques, *Phys. Rev. Lett.* **110**, 060502 (2013).

[11] G. Waldherr *et al.*, *Nature* **506**, 204 (2014).

[12] G. D. Fuchs, G. Burkard, P. V. Klimov, and D. D. Awschalom, *Nature Phys.* **7**, 789 (2011).

[13] E. L. Hahn, *Phys. Rev.* **80**, 580 (1950).

[14] Z.-H. Wang, G. de Lange, D. Ristè, R. Hanson, and V. V. Dobrovitski, *Phys. Rev. B* **85**, 155204 (2012).

[15] A. M. Souza, G. A. Álvarez, and D. Suter, *Phys. Rev. Lett.* **106**, 240501 (2011).

[16] H. Y. Carr and E. M. Purcell, *Phys. Rev.* **94**, 630 (1954).

[17] S. Meiboom and D. Gill, *Review of Scientific Instruments* **29**, 688 (1958).

[18] N. Bar-Gill, L. M. Pham, A. Jarmola, D. Budker, and R. L. Walsworth, *Nature Communications* **4**, 1743 (2013).

[19] C. A. Ryan, J. S. Hodges, and D. G. Cory, *Phys. Rev. Lett.* **105**, 200402 (2010).

[20] J. M. Taylor, P. Cappellaro, L. Childress, L. Jiang, D. Budker, P. R. Hemmer, A. Yacoby, R. Walsworth, and M. D. Lukin, *Nature Phys.* **4**, 810 (2008).

[21] J. R. Maze *et al.*, *Nature* **455**, 644 (2008).

[22] L. M. Pham, N. Bar-Gill, C. Belthangady, D. Le Sage, P. Cappellaro, M. D. Lukin, A. Yacoby, and R. L. Walsworth, *Phys. Rev. B* **86**, 045214 (2012).

[23] Y. Chu *et al.*, *Nano Letters* **14**, 1982 (2014).

[24] T. Yamamoto *et al.*, *Phys. Rev. B* **88**, 075206 (2013).

[25] K. Ohno, F. Joseph Heremans, L. C. Bassett, B. A. Myers, D. M. Toyli, A. C. Bleszynski Jayich, C. J. Palmstrøm, and D. D. Awschalom, *Appl. Phys. Lett.* **101**, 082413 (2012).

[26] J. R. Maze, A. Gali, E. Togan, Y. Chu, A. Trifonov, E. Kaxiras, and M. D. Lukin, *New Journal of Physics* **13**, 025025 (2011).

[27] L. Robledo, L. Childress, B. Bernien, H. Hensen, P. F. A. Alkemade, and R. Hanson, *Nature* **477**, 574 (2011).

[28] N. B. Manson, J. P. Harrison, and M. J. Sellars, *Phys. Rev. B* **74**, 104303 (2006).

[29] G. D. Fuchs, V. V. Dobrovitski, R. Hanson, A. Batra, C. D. Weis, T. Schenkel, and D. D. Awschalom, *Phys. Rev. Lett.* **101**, 117601 (2008).

[30] B. Smeltzer, J. McIntyre, and L. Childress, *Phys. Rev. A* **80**, 050302 (2009).

[31] S. Felton, A. M. Edmonds, M. E. Newton, P. M. Martineau, D. Fisher, and D. J. Twitchen, *Phys. Rev. B* **77**, 081201 (2008).

[32] S. Felton, A. M. Edmonds, M. E. Newton, P. M. Martineau, D. Fisher, D. J. Twitchen, and J. M. Baker, *Phys. Rev. B* **79**, 075203 (2009).

[33] M. O. Scully and M. S. Zubairy, *Quantum Optics* (Cambridge University Press, 1997).

[34] I. I. Rabi, *Phys. Rev.* **51**, 652 (1937).

[35] I. I. Rabi, S. Millman, P. Kusch, and J. R. Zacharias, *Phys. Rev.* **55**, 526 (1939).

[36] L. Childress, M. V. G. Dutt, J. M. Taylor, A. S. Zibrov, F. Jelezko, J. Wrachtrup, P. R. Hemmer, and M. D. Lukin, *Science* **314**, 281 (2006).

[37] N. F. Ramsey, *Phys. Rev.* **78**, 695 (1950).

[38] J. R. Maze, J. M. Taylor, and M. D. Lukin, *Phys. Rev. B* **78**, 094303 (2008).

[39] M. V. G. Dutt, L. Childress, L. Jiang, E. Togan, J. Maze, F. Jelezko, A. S. Zibrov, P. R. Hemmer, and M. D. Lukin, *Science* **316**, 1312 (2007).

[40] T. H. Taminiau, J. Cramer, T. van der Sar, V. V. Dobrovitski, and R. Hanson, *Nature Nanotechnology* **9**, 171 (2014).

[41] J. Meijer, B. Burchard, M. Domhan, C. Wittmann, T. Gaebel, I. Popa, F. Jelezko, and J. Wrachtrup, *Appl. Phys. Lett.* **87**, 261909 (2005).

[42] P. Spinicelli *et al.*, *New Journal of Physics* **13**, 025014 (2011).

[43] C. Osterkamp, J. Scharpf, S. Pezzagna, J. Meijer, T. Diemant, R. Jürgen Behm, B. Naydenov, and F. Jelezko, *Appl. Phys. Lett.* **103**, 193118 (2013).

[44] T. Yamamoto, C. Müller, L. P. McGuinness, T. Teraji, B. Naydenov, S. Onoda, T. Ohshima, J. Wrachtrup, F. Jelezko, and J. Isoya, *Phys. Rev. B* **88**, 201201 (2013).

[45] S. Pezzagna, D. Rogalla, H.-W. Becker, I. Jakobi, F. Dolde, B. Naydenov, J. Wrachtrup, F. Jelezko, C. Trautmann, and J. Meijer, *Phys. Status Solidi A* **208**, 2017 (2011).

[46] M. Lesik *et al.*, *Phys. Status Solidi A* **210**, 2055 (2013).

[47] C. D. Weis *et al.*, *Journal of Vacuum Science and Technology B* **26**, 2596 (2008).

[48] D. M. Toyli, C. D. Weis, G. D. Fuchs, T. Schenkel, and D. D. Awschalom, *Nano Letters* **10**, 3168 (2010).

[49] S. Pezzagna, B. Naydenov, F. Jelezko, J. Wrachtrup, and J. Meijer, *New Journal of Physics* **12**, 065017 (2010).

[50] T. van der Sar, Z. H. Wang, M. S. Blok, H. Bernien, T. H. Taminiau, D. M. Toyli, D. A. Lidar, D. D. Awschalom, R. Hanson, and V. V. Dobrovitski, *Nature* **484**, 82 (2012).

[51] B. Naydenov, F. Reinhard, A. Lämmle, V. Richter, R. Kalish, U. F. S. D'Haenens-Johansson, M. Newton, F. Jelezko, and J. Wrachtrup, *Appl. Phys. Lett.* **97**, 242511 (2010).

[52] J. F. Ziegler, M. Ziegler, and J. Biersack, *Nucl. Instrum. Methods Phys. Res., Sect. B* **268**, 1818 (2010).

[53] A. Mainwood, *Phys. Rev. B* **49**, 7934 (1994).

[54] D. J. Twitchen, M. E. Newton, J. M. Baker, T. R. Anthony, and W. F. Banholzer, *Phys. Rev. B* **59**, 12900 (1999).

[55] C. UzanSaguy, C. Cytermann, R. Brener, V. Richter, M. Shaanan, and R. Kalish, *Appl. Phys. Lett.* **67**, 1194 (1995).

[56] D. Antonov *et al.*, *Appl. Phys. Lett.* **104**, 012105 (2014).

[57] S. Sangtawesin, T. O. Brundage, and J. R. Petta, *Phys. Rev. Lett.* **113**, 020506 (2014).

[58] R. Epstein, F. Mendoza, Y. Kato, and D. Awschalom, *Nature Phys.* **1**, 94 (2005).

[59] A. Dréau, M. Lesik, L. Rondin, P. Spinicelli, O. Arcizet, J.-F. Roch, and V. Jacques, *Phys. Rev. B* **84**, 195204 (2011).

[60] B. J. M. Hausmann, T. M. Babinec, J. T. Choy, J. S. Hodges, S. Hong, I. Bulu, A. Yacoby, M. D. Lukin, and M. Loncar, *New Journal of Physics* **13**, 045004 (2011).

[61] B. J. M. Hausmann *et al.*, *Nano Letters* **12**, 1578 (2012).

[62] R. Hanson, O. Gywat, and D. D. Awschalom, *Phys. Rev. B* **74**, 161203 (2006).

[63] P. Neumann, N. Mizuochi, F. Rempp, P. Hemmer, H. Watanabe, S. Yamasaki, V. Jacques, T. Gaebel, F. Jelezko, and J. Wrachtrup, *Science* **320**, 1326 (2008).

[64] L. Jiang *et al.*, *Science* **326**, 267 (2009).

[65] T. H. Taminiau, J. J. T. Wagenaar, T. van der Sar, F. Jelezko, V. V. Dobrovitski, and R. Hanson, *Phys. Rev. Lett.* **109**, 137602 (2012).

[66] P. C. Maurer *et al.*, *Science* **336**, 1283 (2012).

[67] K. Saeedi, S. Simmons, J. Z. Salvail, P. Dluhy, H. Riemann, N. V. Abrosimov, P. Becker, H.-J. Pohl, J. J. L. Morton, and M. L. W. Thewalt, *Science* **342**, 830 (2013).

[68] J. J. L. Morton, A. M. Tyryshkin, A. Ardavan, S. C. Benjamin, K. Porfyrakis, S. A. Lyon, and G. A. D. Briggs, *Nature Phys.* **2**, 40 (2006).

[69] J. J. L. Morton, A. M. Tyryshkin, A. Ardavan, S. C. Benjamin, K. Porfyrakis, S. A. Lyon, and G. A. D. Briggs, *Phys. Status Solidi B* **243**, 3028 (2006).

[70] L. Viola and S. Lloyd, *Phys. Rev. A* **58**, 2733 (1998).

[71] L. C. Bassett, F. J. Heremans, C. G. Yale, B. B. Buckley, and D. D. Awschalom, *Phys. Rev. Lett.* **107**, 266403 (2011).

[72] P. Tamarat *et al.*, *Phys. Rev. Lett.* **97**, 083002 (2006).

[73] V. Filidou, S. Simmons, S. D. Karlen, F. Giustino, H. L. Anderson, and J. J. L. Morton, *Nature Phys.* **8**, 596 (2012).

[74] V. Jacques, P. Neumann, J. Beck, M. Markham, D. Twitchen, J. Meijer, F. Kaiser, G. Balasubramanian, F. Jelezko, and J. Wrachtrup, *Phys. Rev. Lett.* **102**, 057403 (2009).

[75] M. Steiner, P. Neumann, J. Beck, F. Jelezko, and J. Wrachtrup, *Phys. Rev. B* **81**, 035205 (2010).

[76] L. Childress and J. McIntyre, *Phys. Rev. A* **82**, 033839 (2010).

[77] R. Barends *et al.*, *Nature* **508**, 500 (2014).

[78] L. DiCarlo, M. D. Reed, L. Sun, B. R. Johnson, J. M. Chow, J. M. Gambetta, L. Frunzio, S. M. Girvin, M. H. Devoret, and R. J. Schoelkopf, *Nature* **467**, 574 (2010).

[79] B. E. Kane, *Nature* **393**, 133 (1998).

[80] J. J. Pla, F. A. Mohiyaddin, K. Y. Tan, J. P. Dehollain, R. Rahman, G. Klimeck, D. N. Jamieson, A. S. Dzurak, and A. Morello, *Phys. Rev. Lett.* **113**, 246801 (2014).

[81] J. T. Muhonen *et al.*, *Nature Nanotechnology* **9**, 986 (2014).

[82] M. Zhong, M. P. Hedges, R. L. Ahlefeldt, J. G. Bartholomew, S. E. Beavan, S. M. Wittig, J. J. Longdell, and M. J. Sellars, *Nature* **517**, 177 (2015).

[83] M. Chen, M. Hirose, and P. Cappellaro, *Phys. Rev. B* **92**, 020101 (2015).

[84] A. Blais, J. Gambetta, A. Wallraff, D. I. Schuster, S. M. Girvin, M. H. Devoret, and R. J. Schoelkopf, *Phys. Rev. A* **75**, 032329 (2007).

[85] A. Wallraff, D. I. Schuster, A. Blais, L. Frunzio, R. S. Huang, J. Majer, S. Kumar, S. M. Girvin, and R. J. Schoelkopf, *Nature* **431**, 162 (2004).

[86] J. Majer *et al.*, *Nature* **449**, 443 (2007).

[87] J. J. Pla, K. Y. Tan, J. P. Dehollain, W. H. Lim, J. J. L. Morton, F. A. Zwanenburg, D. N. Jamieson, A. S. Dzurak, and A. Morello, *Nature* **496**, 334 (2013).

[88] G. Wolfowicz, A. M. Tyryshkin, R. E. George, H. Riemann, N. V. Abrosimov, P. Becker, H.-J. Pohl, M. L. W. Thewalt, S. A. Lyon, and J. J. L. Morton, *Nature Nanotechnology* **8**, 561 (2013).

[89] K. Saeedi *et al.*, *Scientific Reports* **5**, 10493 (2015).

[90] P. A. Mortemousque, S. Berger, T. Sekiguchi, C. Culan, R. G. Elliman, and K. M. Itoh, *Phys. Rev. B* **89**, 155202 (2014).

[91] B. A. Myers, A. Das, M. C. Dartiailh, K. Ohno, D. D. Awschalom, and A. C. Bleszynski Jayich, *Phys. Rev. Lett.* **113**, 027602 (2014).

[92] G. de Lange, D. Ristè, V. V. Dobrovitski, and R. Hanson, *Phys. Rev. Lett.* **106**, 080802 (2011).

[93] M. Loretz, J. M. Boss, T. Rosskopf, H. J. Mamin, D. Rugar, and C. L. Degen, *Phys. Rev. X* **5**, 021009 (2015).